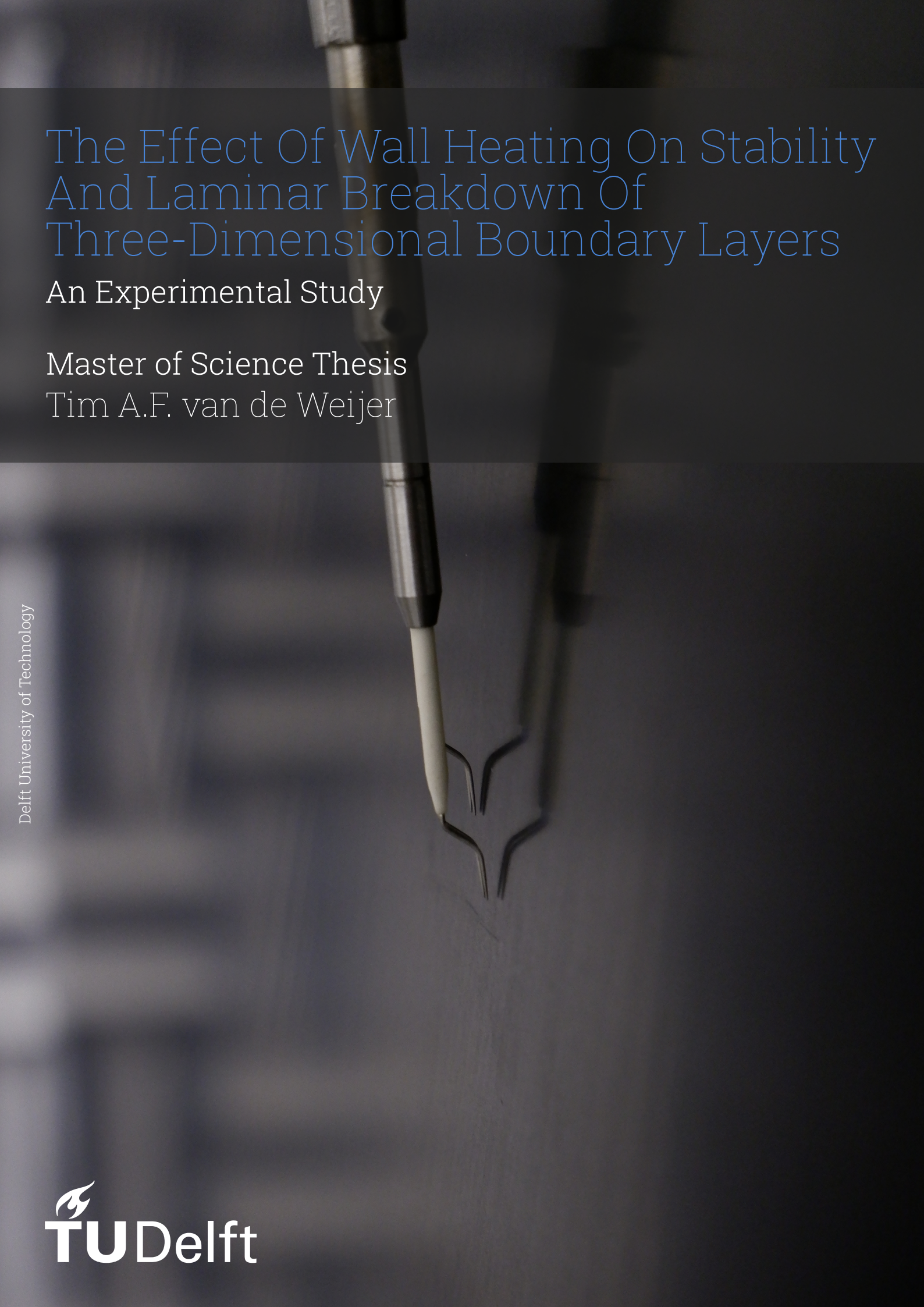

The Effect Of Wall Heating On Stability And Laminar Breakdown Of Three-Dimensional Boundary Layers

An Experimental Study

Master of Science Thesis

Tim A.F. van de Weijer

Delft University of Technology

TU Delft

The Effect Of Wall Heating On Stability And Laminar Breakdown Of Three-Dimensional Boundary Layers

An Experimental Study

by

Tim A.F. van de Weijer

For obtaining the degree of Master of Science in Aerospace Engineering at Delft University of Technology.

Student number:	4551133	
Project duration:	7 November, 2022 – 19 January, 2024	
Thesis committee:	Prof. Dr. Ir. M. Kotsonis,	TU Delft
	Ir. M. Barahona,	TU Delft
	Dr. Ir. A.F. Rius-Vidales,	TU Delft
	Dr. B.W. van Oudheusden,	TU Delft
Faculty:	Aerospace Engineering	
Department:	Flow Physics and Technology	
Section:	Aerodynamics	

TU Delft

Abstract

An important challenge in the electrification of aircraft propulsion systems is the design of thermal management systems because of an increased heat load that needs to be dissipated. As an alternative to high-drag external heat exchangers, one can consider surface heat exchangers to dissipate the extra thermal energy. This reduces the size of the external heat exchangers and consequently reduces drag. However, a non-adiabatic wall can affect skin friction through a movement of boundary layer transition. Limited studies are available on the effect of non-adiabatic surfaces on laminar-to-turbulent transition in swept wing boundary layers dominated by crossflow instability (CFI). Therefore, the current work experimentally investigates the effect of surface heating on the stability and breakdown of the stationary crossflow instability. The experimental work is supported by Compressible Linear Stability Theory (CLST) computations.

Hot-Wire Anemometry (HWA) and Cold-Wire Anemometry (CWA) measurements of the boundary layer are performed on the STEP model, which features a 45°swept flat plate, for both adiabatic and heated surface conditions. Both the experimental and CLST results show a destabilisation of the primary instability linked to the increase in the growth rate of the stationary crossflow (CF) mode. The experimental results show that the type-I secondary CF instability exhibits a larger magnitude in the presence of wall heating and the mode emerges upstream compared to the adiabatic wall condition. The type-III mode displays a significant increase in magnitude in the presence of wall heating, thereby indicating a considerable destabilisation. The effect on laminar breakdown is identified by analysing velocity fluctuations in the $12-17\ kHz$ frequency band in planes parallel to the surface for two different wall distances. A temperature ratio of $T_w/T_f = 1.035$ is found to advance breakdown by 5.7%.

Preface

This thesis marks the end of my journey to my master's degree. It has been an interesting journey to say the least. Unlike my thesis topic, it has been turbulent at times, but overall, it has been filled with new experiences and I have learned an incredible amount. There are a few people I would like to thank for their support along my journey.

First of all, I wish to express my gratitude to Marina for her supervision and help whenever necessary. You were always available to help me out and I learned a great amount from you. Together we spent many weeks inside the A-tunnel, I will look back upon this with good memories. I also want to thank Beto for his supervision, mental support and help in the wind tunnel. I have always enjoyed our conversations and I am grateful that I have been able to pick your brain. This certainly helped me develop myself in this journey. The last person I'd like to thank for the supervision is Prof. Marios Kostonis. I enjoyed the meetings we had because of your endless optimism. I have found this to be very helpful. I am also thankful for the technical support of Stefan, Emiel and Martijn in the wind tunnel.

I want to thank my friends Sander, Ronald, Thomas, Jesse and John. We have known each other for a long time, and I have thoroughly enjoyed every second we spent together. You always allow me to reset mentally and you give me different perspectives on life, which I always find very enriching. This certainly helps me a great deal.

Lastly, I would like to thank my family. Ivo, Kirsten and Job, it has always been good to discuss the struggles of life and education with you and I am grateful for your support. I also want to thank my late Father. Although you are unfortunately not with us anymore, you'll always be an inspiration to me.

In special, I would like to thank my mother. For years, you have selflessly cared for me and my siblings at your own expense. During my graduation period, you have always provided me with support whenever needed and you have always believed in me. I will always be grateful for everything you have done for me.

Tim A.F. van de Weijer
Delft, January 2024

Contents

List of Figures

List of Tables

Nomenclature

Abbreviations

CF	Crossflow
CFI	Crossflow Instability
CLST	Compressible Linear Stability Theory
CTA	Constant Temperature Anemometry
CW	Cold Wire
CWA	Cold Wire Anemometry
DRE	Discrete Roughness Element
HW	Hot Wire
HWA	Hot Wire Anemometry
IR	Infrared
LE	Leading Edge
LST	Linear Stability Theory
PDF	Probability Density Function
PET	Polyethylene Terephthalate
PSE	Parabolised Stability Equations
PSD	Power Spectral Density
RMS	Root Mean Square
SFP	Swept Flat Plate
TE	Trailing Edge
LSL	Low Speed Laboratory
TS	Tollmien–Schlichting

Symbols

A_I	Amplitude of steady disturbance	[m/s]
A_{II}	Amplitude of unsteady disturbance	[-]
C_p	pressure coefficient	[-]
b	span of model	[m]
c	chord of model	[m]
d_w	Wire sensor diameter	[µm]
E	HWA or CWA output voltage	[V]
f_{res}	Frequency resolution	[Hz]
f_s	Sampling rate	[Hz]
H	Shape Factor	[-]
h	Heat transfer coefficient	[W/m^2/K]
I_w	Electrical amperage	[A]
l_w	Wire sensor length	[mm]
Nu	Number of samples	[-]
Nu	Nusselt number	[-]
N_{eff}	Effective number of samples	[-]
Pr	Prandtl number	[-]
Q	Velocity perceived by HWA	[m/s]
q	Disturbance	[m/s]
R	Electrical resistance	[Ω]
Re_d	Reynolds number $Re_d = Ud/\nu$	[-]
Ri	Richardson number $Ri = \frac{g\beta(T_\mathrm{w}-T_\mathrm{ref})d}{U^2}$	[-]

T	Temperature	[°C]
T_I	Integral timescale	[s]
Tu	Turbulence intensity	[-]
U, V, W	Global velocity components	[m/s]
u, v, w	Local velocity components	[m/s]
X, Y, Z	Global coordinate system	[m]
x, y, z	Local coordinate system	[m]
α	Streamwise wavenumber	[-]
β	Spanwise wavenumber	[-]
δ_T	Thermal boundary layer thickness	[m]
δ_{99}	Velocity boundary layer thickness	[m]
δ^*	Displacement thickness	[m]
ε_a	Uncertainty of quantity a	[m/s]
Θ	Non-dimensional temperature.	[-]
θ	Momentum thickness	[m]
Λ	Sweep angle	[°]
λ_z	Spanwise wavelength of the crossflow vortices	[mm]
$\lambda_{z,D}$	Spanwise wavelength of the DRE's	[mm]
μ	Dynamic viscosity	[kg m/s]
ρ	Density or auto-correlation function	[kg/m^3,-]
σ	Standard deviation	[m/s]
Φ	Probability density function	[(m/s)^2/Hz]
ω	Angular frequency	[1/s]

Subscripts and Accents

$\bar{a}$	Temporally-averaged quantity
a'	Perturbation or fluctuating quantity
$\langle a' \rangle_z$	Spanwise root mean square of quantity
a_e	External flow quantity
a_f	Bandpass filtered quantity
a_i	Imaginary component of quantity
a_r	Real component of quantity
a_w	Quantity at the model's surface or related to the wire sensor
a_z	Spanwise averaged quantity
a_0	Initial or reference value of quantity
a_∞	Quantity at freestream conditions
$\langle a \rangle_z$	Spanwise root mean square of quantity

1 Introduction

This chapter is written to introduce the research topic to the reader by providing context, relevance, background theory, a literature review and, eventually, the research objectives.

1.1 Motivation

The ongoing climate crisis requires the reduction of greenhouse gas emissions. This necessity is driving a global redesign of the current transportation methods. Different technologies and approaches are being investigated within the aviation industry to lower its contribution to climate change. These include increasing the efficiency of existing propulsion technologies, introducing sustainable aviation fuels, reducing direct carbon emissions (hydrogen combustion) and true zero-emissions through electrification (battery-electric and hydrogen-electric technology). Some of these true zero-emission technologies are currently being developed and tested by large stakeholders in the industry. For instance, Rolls-Royce is developing hydrogen combustion technology (Rolls-Royce, 2022) and Airbus is ground testing its ZEROe Fuel Cell engine (Airbus, 2023). A challenge of these true zero-emission technologies is the thermal management of these systems as they produce a large amount of heat that needs to be dissipated (Coutinho et al., 2023). The conventional approach uses external heat exchangers, such as ram-air cooling solutions, that re-direct the airflow for cooling purposes. The main disadvantage of this solution is its pressure drag penalty (Schlabe & Lienig, 2014).

An alternative to the conventional heat exchanger is the use of the aircraft's skin as a heat exchanger. The advantage of this technology is that it reduces the size of the required external heat exchangers, thereby decreasing pressure drag. However, one has to consider that this technique could also increase the aircraft's skin friction drag. Small perturbations are introduced in the boundary layer that grow in space and time, eventually triggering laminar-to-turbulent transition of the boundary layer. The process between the introduction of the disturbance and transition is also referred to as boundary layer stability.

Turbulent boundary layers exhibit higher wall shear stress than laminar boundary layers. Thus, delaying boundary layer transition is advantageous to reduce skin friction drag, which constitutes up to 50% (Marec, 200) of the total aircraft drag. Hence, it is important to understand how surface heat transfer affects the boundary layer stability and, consequently, transition.

The effect of non-adiabatic surfaces on boundary layer stability is not a new topic and has been widely investigated considering Tollmien-Schlichting waves, see for example Costantini et al. (2016), Frick and McCullough (1942), Liepmann and Fila (1947), and Özgen (2004). This instability type is typically dominant in the presence of an adverse pressure gradient in two-dimensional boundary layers such as unswept wings (Joslin, 1998). However, most commercial aircraft are designed with swept wings to delay drag divergence, so larger cruise speeds can be achieved. Such swept wings develop a three-dimensional boundary layer which is typically susceptible to crossflow instabilities (CFI) (Saric et al., 2003).

The effect of non-adiabatic surfaces on the stability of the crossflow instability is yet not well understood and lacks experimental research. Thus, combined with the technological advances in the

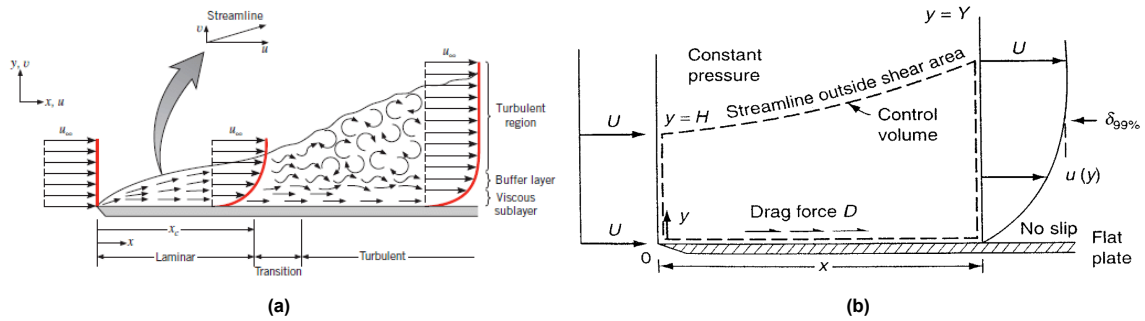

Figure 1.1: Schematic of a boundary layer in the streamwise direction. (a) Visualisation of a boundary layer over a semi-infinite flat plate, reproduced from Bergman et al. (2011). (b) Control volume for integral analysis of the boundary layer, reproduced from White (2006).

electrification of propulsion systems such as aircraft hydrogen fuel cell technology that generates a considerable heat load, the objective of the research in this MSc thesis is to investigate the effect of surface heating on the stability and transition of the three-dimensional laminar boundary layer dominated by crossflow instabilities.

1.2 Fundamentals of Boundary Layers

1.2.1 Velocity Boundary Layer Theory

As a fluid flows over a surface, a velocity boundary layer (also denoted boundary layer (BL) in the remainder of the document) develops if the Reynolds number ($\text{Re}_d = \frac{\rho U d}{\mu}$ where μ represents the viscosity of the fluid, ρ the fluid's density, d the characteristic length of the object and U the fluid's velocity) is sufficiently high. In the present study, a fluid dynamics problem is investigated considering air flows with a low viscosity, hence the Reynolds number is sufficiently large for the boundary layer concept to apply. In the boundary layer concept, viscous forces are considered to be isolated to the thin region near the wall (the boundary layer). In contrast, the external flow (outside of the BL) is considered to be inviscid. The boundary layer is conditioned through the interaction with the wall at which a no-slip condition is imposed through viscous forces. Considering a stationary surface, the velocity has to become zero at the surface, thereby creating a large shear between the wall and the external conditions bridged by the boundary layer. The development of a boundary layer over a swept flat plate is visualised in Figure 1.1a.

A set of parameters can be defined to gain insights into the development of the boundary layer. Firstly, the boundary layer thickness δ_{99} quantifies the wall-normal distance where the velocity inside the boundary layer reaches 99% of the local external velocity ($\delta_{99} = y(U = 0.99U_e)$ with U being the local velocity and U_e the external velocity). Secondly, the displacement thickness δ^* is defined which specifies the displacement of a streamline outside of the boundary in the wall-normal direction. δ^* is obtained through an integral analysis between the undisturbed flow (i.e. before the leading edge (LE)) and the local boundary layer condition. One can define a control volume limited in the streamwise direction by these boundaries while defining the domain in the wall-normal direction by the wall location and the streamline yielding Figure 1.1b. Evaluation of the continuity equation of this control volume can be shown to reduce to Equation 1.1 (White, 2006) for a compressible boundary layer. The usage of the compressible form as the to-be-discussed non-adiabatic wall modifies the density across the boundary layer. In Equation 1.1 ρ represents the local density while ρ_e is the density of the external flow, u represents the local velocity and U_e the velocity in the external flow.

$$\delta^* = \int_0^{\delta_{99}} \left(1 - \frac{\rho}{\rho_e}\frac{u}{U_e}\right) dy \tag{1.1}$$

To express the decrement of momentum in the boundary layer compared to undisturbed conditions, the momentum thickness (θ) is defined. This parameter specifies the movement of the wall in the undisturbed condition required to achieve a decrease in momentum equal to that of the boundary layer. It is computed with Equation 1.2 (compressible form) and is derived through an evaluation of the momentum equation on the control volume depicted in Figure 1.1b (see White, 2006).

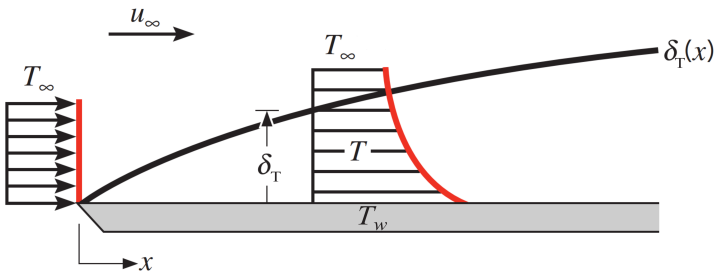

Figure 1.2: Visualisation of a thermal boundary layer over a semi-infinite flat plate, figure adapted from Bergman et al. (2011).

$$\theta = \int_0^{\delta_{99}} \frac{\rho}{\rho_e}\frac{u}{U_e}\left(1 - \frac{u}{U_e}\right) dy \tag{1.2}$$

A combination of the momentum and displacement thickness yields the shape factor H that provides an indication of the shape of the boundary layer profile. The fuller a profile is, the lower the value of H typically is. This is an important variable as the fullness of the profile provides a first indication of the stability of the boundary layer as a decrease in the fullness is associated with a reduction in the stability of the instability type in question (Ren & Kloker, 2022).

$$H = \frac{\delta^*}{\theta} \tag{1.3}$$

1.2.2 Thermal Boundary Layer Theory

The effect of a thermal boundary condition on the dynamics of a flow problem can be typically categorised into three convection modes: forced convection, mixed convection and natural convection. Natural convection is conditioned by buoyancy effects within the fluid, whereas heat is transported by the movement of a fluid in forced convection conditions. If both phenomena are relevant, the term *mixed convection* is used. The Richardson Number (see Equation 1.4) can be used to determine the convection regime of the flow problem where forced convection typically is present for $Ri < 0.1$ and natural convection for $Ri > 10$ (Zafar & Alam, 2020). In this work, forced convection is the dominant mode, hence, $Ri < 0.1$.

$$Ri = \frac{g\beta\,(T_\mathsf{w} - T_\mathsf{ref})\,d}{U^2} \tag{1.4}$$

As fluid flows over a surface with a wall temperature different from the fluid temperature, thermal gradients will exist in the wall-normal direction. Applying a similar boundary layer concept to the region where these thermal gradients exist yields the concept of a thermal boundary layer. A schematic of the thermal boundary layer is shown in Figure 1.2. As for the velocity boundary layer, a thermal boundary layer thickness (δ_T) can be defined. For this definition, the temperature is generally normalised using Equation 1.5 where T is the local temperature, T_w represents the wall temperature and T_e is the external temperature (White, 2006). The thermal boundary layer thickness is then defined such that $\delta_T = y(\Theta = 0.99)$ analogues to δ_{99}.

$$\Theta = \frac{T - T_e}{T_w - T_e} \tag{1.5}$$

The relative thickness of the thermal and velocity boundary layer in laminar flow is a function of the fluid properties and can be formulated as a function of the Prandtl Number $Pr = \mu c_p/k$. c_p is the specific heat capacity, μ the dynamic viscosity and k the thermal conductivity of the fluid. The Pr number specifies the relation between the momentum diffusivity and the thermal diffusivity of a fluid, thereby relating the thickness of the velocity and thermal boundary layer. For laminar boundary layers, the relation between δ_T and δ_{99} generally follows a form of Equation 1.6 with n being a positive constant (Bergman et al., 2011). For example, $n = 0.4$ is found to satisfy Equation 1.6 well for a Blasius boundary layer with a constant wall temperature (White, 2006). When $Pr = 1$, the thermal and velocity boundary layers behave similarly (White, 2006), hence, the thermal and velocity BL thickness and profiles are similar.

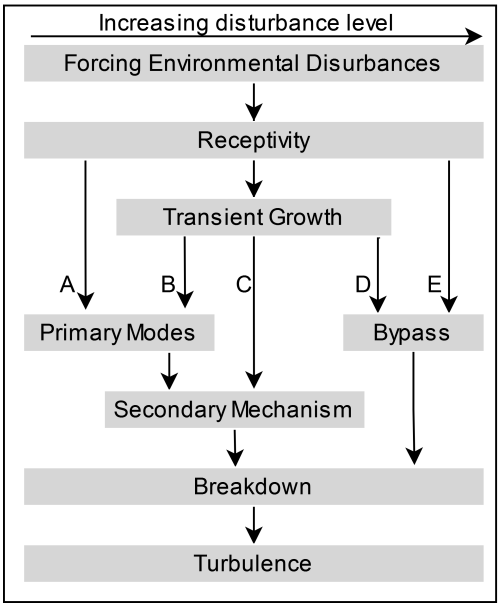

Figure 1.3: Adapted representation of roadmap to turbulence as presented by Morkovin (1994).

For air flows the Prandtl number is found to be $Pr \approx 0.71$ considering atmospheric pressures and the temperature in the range of $T = 223 - 373\ K$. Therefore, the thermal boundary layer is thicker than the velocity boundary layer for air flows.

$$\frac{\delta_T}{\delta_{99}} \approx Pr^{-n} \tag{1.6}$$

The presence of a thermal boundary layer affects the properties of the fluid. To be specific, for air flows, the density ρ and viscosity μ are proportional to the temperature and thus they vary across the temperature profile. For example, the viscosity and density of air are proportional to the air temperature. As the temperature increases, the viscosity increases and the density decreases. The importance of the variation of these fluid properties will be highlighted at a later stage.

1.2.3 Roadmap to Turbulence

The transition process from a laminar to a turbulent boundary layer can occur along a set of different processes well described in the 'roadmap' provided in Figure 1.3 as introduced by Morkovin (1994). The shared first step is the introduction of disturbances in the boundary layer by external disturbances, this process is also referred to as receptivity. The magnitude of the external disturbances determines the initial conditions of the disturbance introduced in the boundary layer and it affects the route to turbulence. For weak disturbances path *A* is followed in Figure 1.3, initially unstable disturbances grow linearly after which secondary mechanisms take over and cause breakdown of the laminar boundary layer and turbulent flow. As the initial disturbance grows in amplitude, path *B* to *D* may occur where the disturbances first exhibit transient growth. If the freestream disturbances are sufficiently large, linear growth is bypassed (Saric et al., 2002) and turbulence can come quickly through turbulent spots or subcritical instabilities. In this work, the disturbances are considered to be small and thus path *A* is considered in Figure 1.3. Consequently, path *B* to *E* is not further discussed and the reader is referred to literature of, for example, Morkovin (1994) and Saric et al. (2002) for more information.

1.3 Three Dimensional Boundary Layer Instabilities

Following path *A* in the roadmap, the laminar boundary layer is susceptible to the growth of small disturbances which eventually become large enough to trigger the laminar to turbulent transition. The majority of commercial aircraft have swept wings to increase the drag divergence Mach number, thereby increasing (cruise) speed. Over such swept wings, the path of the inviscid streamline (see Figure 1.4a) is determined by a combination of the pressure gradient and the centrifugal forces which balance the

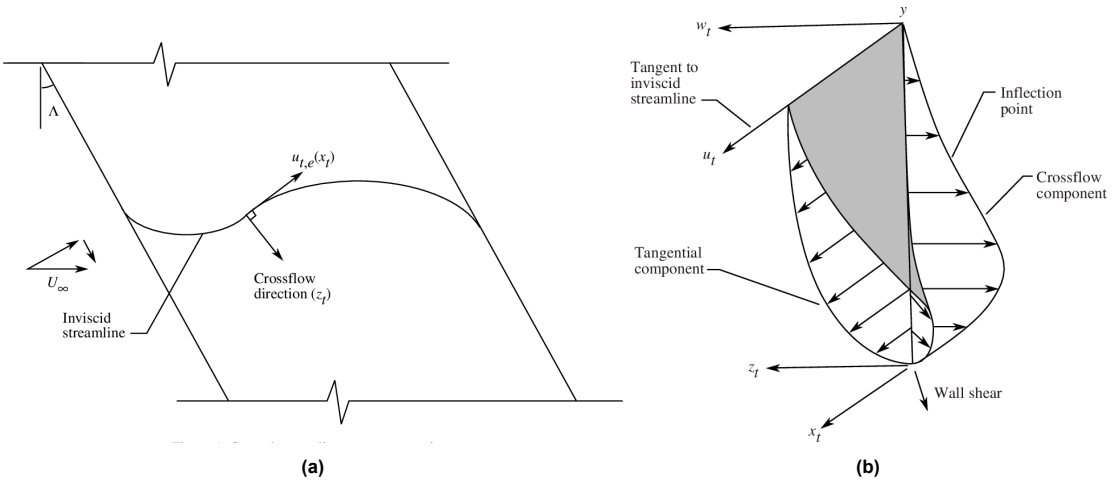

Figure 1.4: Schematics showing the development of the crossflow instability: (a) Infinite swept wing indicating the inviscid streamline curvature, reproduced from Dagenhart and Saric (1999). (b) Velocity profile of a three-dimensional boundary layer, reproduced from Dagenhart and Saric (1999).

pressure force outside the boundary layer. As the momentum decreases in the boundary layer, the centrifugal forces decrease, leading to an imbalance which results in a secondary flow component orthogonal to the inviscid streamline called *crossflow* (CF) (Bippes, 1999; Saric et al., 2003), see Figure 1.4b. Depending on the conditions, such a three-dimensional boundary layer is susceptible to attachment-line contamination, Görtler vortices, Tollmien Schlichting Waves and/or Crossflow instabilities (Reed & Saric, 1989).

Attachment-line contamination occurs along the attachment-line of the airfoil as disturbances propagate from the root towards the tip in backwards-swept configurations. Contamination of the attachment-line can happen when turbulent flow from the fuselage boundary layer or other structures impinges on the attachment-line of the swept wing. As the disturbances propagate along the attachment-line, the boundary layer can be tripped, causing early laminar-to-turbulent transition. Previous studies have shown that the damping of this disturbance has a large dependency on the LE radius. Moreover, Reed and Saric (2014) concluded that the consensus, within available literature, is that the disturbance is damped when Equation 1.7 is satisfied. Re_u represents the Reynolds number based on the freestream conditions with a unit characteristic length, e is the thickness ratio of the elliptical LE and r is the LE geometrical radius.

$$\bar{R} = \sqrt{\frac{Re_u\, r\, \tan(\Lambda)\, \sin(\Lambda)}{1+e}} \leq 247 \tag{1.7}$$

In the absence of a turbulent disturbance, the flow propagating along the attachment-line is laminar. However, the consensus is that an instability can grow when Equation 1.8 is satisfied (Reed & Saric, 2014). When the disturbances become large enough, the attachment-line becomes turbulent, tripping the boundary layer.

$$\bar{R} = \sqrt{\frac{Re_u\, r\, \tan(\Lambda)\, \sin(\Lambda)}{1+e}} \geq 583 \tag{1.8}$$

Görtler vortices develop in shear flows over concave surfaces. These counter-rotating vortices are streamwise vortices are linked to the previously described imbalance of the centrifugal and pressure forces in the boundary layer (Boiko et al., 2002). However, the formation of Görtler vortices can be easily prevented by avoiding concave surfaces. Laminar flow control design wings typically do not feature such concave surfaces (Saric et al., 2011).

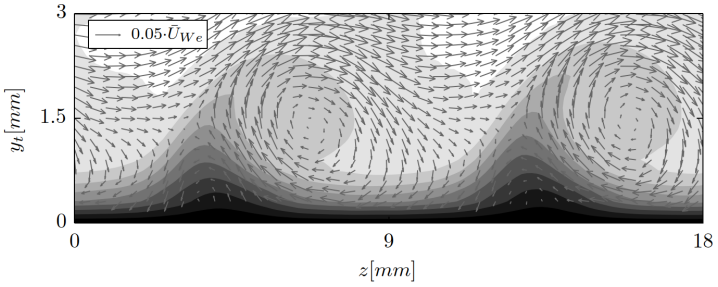

Figure 1.5: Time-averaged velocity field in the presence of stationary crossflow instabilities. Vectors represent the velocity direction and the magnitude of the in-plane components, the contours represent the out-of-plane component. Reproduced from Serpieri (2018).

1.3.1 Tollmien Schlichting Waves

Typically a (viscous) streamwise instability grows in the adverse pressure gradient region of a swept wing if the crossflow component of the three-dimensional (or two-dimensional) boundary layer is relatively weak. This type of instability is two-dimensional, unsteady and grows in the streamwise direction.

Tollmien Schlichting (TS) waves are susceptible to a range of disturbances: acoustic disturbances (Leehey & Shapiro, 1980), 2D vortical disturbance (Kachanov et al., 1978) and surface roughness (Saric et al., 1991) can all successfully excite TS waves. At low freestream turbulence levels, the growth of the TS waves agrees well with linear stability theory and the obtained stability diagram (Schmid & Henningson, 2000) while nonlinear growth and saturation downstream of the first neutral point occur at higher turbulence levels (Boiko et al., 2002). The travelling waves are modulated in the spanwise direction and secondary instabilities emerge as the disturbance grows linearly and large amplitudes are achieved. These secondary instabilities are amplified rapidly and eventually trigger laminar-to-turbulent transition through K-type or H-type boundary layer breakdown (Boiko et al., 2002; Schmid & Henningson, 2000). Strong shear layers are created by the spanwise modulation of the TS waves which leads to a set of Λ vortices. A staggered pattern of these Λ vortices as breakdown happens due to the H-type while the Λ vortices are aligned in K-type breakdown. Again different techniques have been developed over the years which include but are not limited to suction (e.g. Bodonyi and Duck, 1992), tailoring of surface geometry by increasing the favourable pressure gradient region (see Joslin, 1998), wave cancellation through active flow control (e.g. Li and Gaster (2006), Liepmann and Nosenchuck (1982)), surface irregularities such as steps and wall heat transfer.

1.3.2 Crossflow Instabilities

Attachment-line instabilities can be prevented by avoiding a large LE radius while the Görtler instability is prevented by avoiding concave surfaces in the wing design. TS waves can be avoided by preventing large adverse pressure gradients, and additionally, Crossflow Instabilities dominate over TS waves for sweep angles over 25° (see Joslin, 1998). Consequently, the control of CFI is of interest and is widely studied.

An inflection point exists in the crossflow component of the three-dimensional boundary layer due to the no-slip condition at the surface and the absence of crossflow outside the boundary layer. This makes the boundary layer susceptible to inviscid instabilities (Bippes, 1999; Saric et al., 2003). The instability is manifested as a set of travelling or stationary co-rotating vortices aligned with the inviscid streamline within a few degrees (Bippes, 1999; Saric et al., 2003). This and the distortion of the boundary layer flow is visualised in Figure 1.5. Travelling and stationary CF vortices can co-exist, but the dominant mode depends on certain conditions. Deyhle and Bippes (1996) found that stationary CF modes dominate in low freestream turbulence environments while travelling CF modes dominate in high turbulence ones. Deyhle and Bippes (1996) set $Tu = 0.15\%$ as a criterion at which travelling CF modes start to dominate. However, White et al. (2001) found that the receptivity of the two types is affected by the interaction between surface roughness and freestream turbulence implicating that no simple criterion can be used. Contrary to TS waves, the crossflow instability is found to be insensitive to acoustic perturbations (Deyhle & Bippes, 1996).

The development of the stationary crossflow vortices is divided into a primary and a secondary instabil-

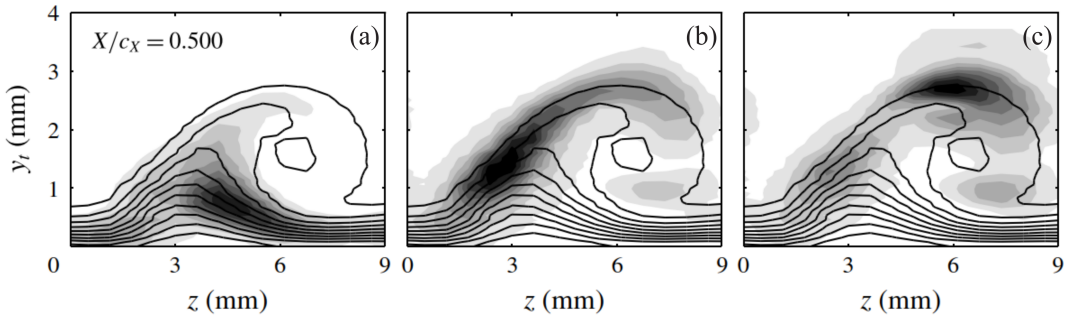

Figure 1.6: Contours of filtered velocity fluctuations (grey scale) and time-averaged velocity field (solid black lines, 10 levels from 0 to U_∞) on a swept wing model (45°). (a) Type-III mode, velocity fluctuations in the $350 \leq f \leq 550\ Hz$ range (10 levels from 0 to $0.24U_\infty$). (b) Type-I mode, velocity fluctuations in the $5 \leq f \leq 6\ kHz$ range (type-I mode, 10 levels from 0 to $0.6U_\infty$). (c) Type-II mode, velocity fluctuations in the $7 \leq f \leq 8\ kHz$ range (10 levels from 0 to $0.6U_\infty$). Adapted from Figure 20 in Serpieri and Kotsonis (2016).

ity. Initially, the primary CF instability amplifies linearly in agreement with linear theory. However, due to the co-rotating nature of the vortices inside the boundary layer, low-momentum fluid is transferred away from the wall (upwelling) and high-momentum fluid is transferred towards the wall (downwelling) as is also evident in Figure 1.5. This transfer in momentum eventually leads to nonlinear distortion of the boundary layer and amplitude saturation of the primary CF instability (Bippes, 1999; Saric et al., 2003). The presence of these nonlinear distortions leads to discrepancies between experimental results and linear stability methodologies (Haynes & Reed, 2000).

The strong spanwise modulation of the boundary layer flow by the stationary CF vortices introduces wall-normal and spanwise velocity gradients (Saric et al., 2003) that produce high-frequency secondary instabilities (Bippes, 1999; White & Saric, 2005). The work of Koch et al. (2000), Malik et al. (1996), and Wasserman and Kloker (2002, 2003) shows that these high-frequency instabilities grow rapidly. This eventually leads to the breakdown of the CF vortices and turbulent flow (Saric et al., 2003; Serpieri & Kotsonis, 2016; Wasserman & Kloker, 2002).

Two different modes have been found to be of the Kelvin-Helmholtz type (Bonfigli & Kloker, 2007), the type-I (or *z*) mode and the type-II (or *y*) mode. The spanwise velocity gradient $\partial U/\partial z$ imposed by the nonlinear distortion of the boundary layer, produces the type-I modes (White & Saric, 2005). The type-I modes are typically located in the outer region of the upwelling region (Serpieri, 2018) where the spanwise gradient is minimum, see Figure 1.6(b). The type-II modes, on the other hand, are produced by the wall-normal velocity gradient $\partial U/\partial y$ (White & Saric, 2005) and are typically located on top of the primary vortices (Serpieri & Kotsonis, 2016), see Figure 1.6(c). The type-II modes typically occur at higher frequencies than the type-I modes but have a smaller growth rate (White & Saric, 2005).

A third mode is visualised in Figure 1.6(a) near the wall at the inner side of the upwelling region which is denoted as the type-III mode. A fundamental difference with the type-I and II modes is that these type-III modes are not of the Kelvin-Helmholtz instability type. Instead, the type-III mode is associated to an interaction between the stationary CF vortices and travelling CF vortices (Bonfigli & Kloker, 2007; Serpieri & Kotsonis, 2016; Wasserman & Kloker, 2002, 2003; White & Saric, 2005). Therefore, the type-III mode provides information about the presence of the travelling CF vortices.

Many techniques are being investigated to control this type of instability. Some of these techniques make use of wall suction/blowing (including but not limited to Friederich and Kloker (2012a), Friederich and Kloker (2012b), and Mack (1980)), plasma actuators (see for example Dörr and Kloker (2015), Peng et al. (2022), and Yadala et al. (2018, 2021)), forcing of sub-critical modes using Distributed Roughness Elements (DRE) (see for example Hosseini et al. (2013), Saric et al. (2019), and Wasserman and Kloker (2002)) and surface irregularities in the form of forward-facing steps (see Casacuberta et al. (2023), Ivanov and Mischenko (2019), and Rius Vidales (2022)).

1.4 Influence of Non-Adiabatic Walls on Transition: CFI

The consensus behind the effectivity of non-adiabatic walls on Tollmien-Schlichting waves relates to the instability type. TS waves are considered to have a viscous nature, and therefore, the modification of the near-wall viscosity through non-adiabatic walls has a large effect on their growth. The destabilisation by wall heating for low subsonic flow was confirmed experimentally in the 40s by Frick and McCullough (1942) and Liepmann and Fila (1947) but also numerically later by, for example, Özgen (2004). Recently, the destabilisation/stabilisation by wall heating/cooling was experimentally studied and confirmed for Mach numbers $0.35 \leq M \leq 0.77$ by Costantini et al. (2015, 2016, 2020) in a cryogenic facility.Theisen et al. (1979) and Reshotko (1979) applied the concept of wall cooling to a hypothetical cryogenic hydrogen aircraft numerically and found a total drag reduction of 27 and 20%, respectively, for a temperature ratio of $T_w/T_f = 0.8 - 0.87$. This displays the effectiveness and potential of wall cooling as a flow control strategy in the presence of TS waves on an aircraft design level.

In contrast, crossflow instabilities are considered to have an inviscid nature as they originate from an inflectional instability. The effect of non-adiabatic walls on CF vortices can illustrated using a mathematical derivation. Following the derivation provided in Ren and Kloker (2022), the momentum equation is evaluated at the wall for the x and z component yielding Equation 1.9. CFI is unstable in the presence of a favourable pressure gradient, thus, let's assume that $\frac{dp}{dx} < 0$, this means that no separation can occur as $\frac{\partial^2 u}{\partial^2 y}|_w < 0$. $\partial u/\partial y$ and $\partial w/\partial y$ are known to be positive at the wall because of the no-slip condition. In case of wall heating in gas flows, $\frac{\partial \mu}{\partial y}|_w < 0$ meaning that $\frac{\partial^2 u}{\partial^2 y}|_w$ increases (i.e. becoming less negative). As a result, the momentum deficit in the boundary layer increases (i.e. the boundary layer becomes less full). Consequently, the wall distance of the inflection point in the crossflow profile is increased, increasing the inviscid instability (Ren & Kloker, 2022). For wall cooling in gas flows, $\frac{\partial \mu}{\partial y}|_w > 0$, hence, a decrease in the height of the inflection point is expected, stabilising the CFI.

$$\left.\frac{\partial^2 u}{\partial y^2}\right|_w = \frac{Re}{\mu_w}\frac{dp}{dx} - \left.\left(\frac{1}{\mu}\frac{\partial \mu}{\partial y}\frac{\partial u}{\partial y}\right)\right|_w \tag{1.9a}$$

$$\left.\frac{\partial^2 w}{\partial y^2}\right|_w = -\left.\left(\frac{1}{\mu}\frac{\partial \mu}{\partial y}\frac{\partial w}{\partial y}\right)\right|_w \tag{1.9b}$$

Apart from the movement of the inflection point, it can also be shown that the crossflow component is affected by non-adiabatic walls. By neglecting the viscous forces in the momentum equation along the local spanwise axes, the bulk cross-pressure equation can be obtained to be Equation 1.10 where R is the local radius of the streamline. Under the assumption of an infinite swept wing ($\frac{dp}{dz_s}$ remains constant), the streamwise velocity component (u_s, the subscript s denotes the local inviscid streamline coordinate system) and density increases for an increasing wall distance for wall heating conditions. To satisfy the constant condition of the left-hand side in Equation 1.10, R has to increase when moving away from the wall. This means that R is smaller near the wall in the presence of wall heating and the curvature of the streamline is higher. This increased curvature leads to an increased crossflow component (w_s, the subscript s denotes the local inviscid streamline coordinate system) and thus a destabilisation. In the case of wall cooling, the opposite effect is found.

$$\frac{dp}{dz_s} = -\frac{\rho}{R}u_s^2 \tag{1.10}$$

Even though the above method showcases the mechanism of non-adiabatic walls on CF vortices, the effectiveness is commonly challenged in comparison with TS waves (e.g. Reshotko, 1979). As a result, the effect of non-adiabatic walls on the CFI is not widely investigated. To the best of the author's knowledge, publications are limited to that of Eppink and Wlezien (2011), Fey et al. (2003), Lekoudis (1980), Mack (1980), Manuilovich and Ustinov (2014), Ren and Kloker (2022), and Tempelmann, Hanifi, and Henningson (2012).

1.4.1 Numerical Investigations With Uniform Non-Adiabatic Walls

The studies of Lekoudis (1980), Mack (1980), Manuilovich and Ustinov (2014), and Ren and Kloker (2022) use Compressible Linear Stability Theory (CLST) to assess the effect of non-adiabatic walls

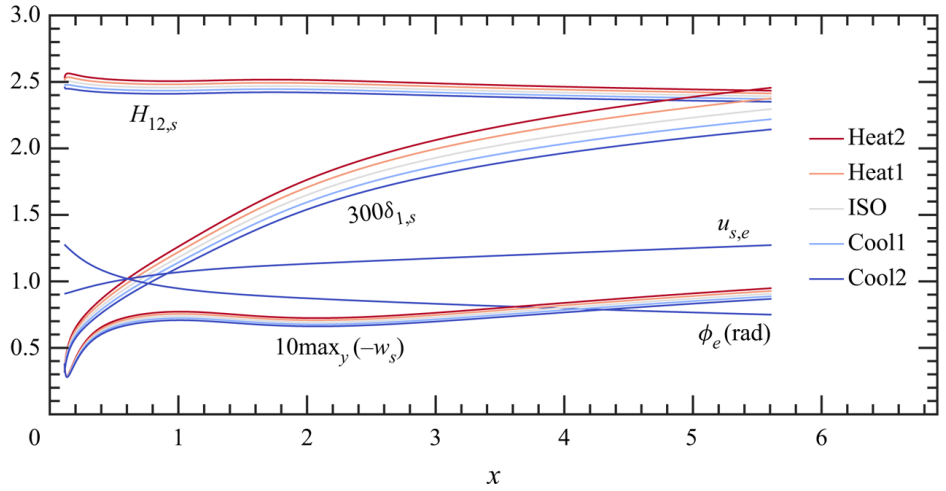

Figure 1.7: The effect of non-adiabatic walls on the baseflow in ideal gas conditions of CO_2 flow at 80 bar pressure. Boundary layer parameters as a function of x. Subscript s refers to the local streamline direction and e refers to the boundary layer edge. Reproduced from Ren and Kloker (2022)

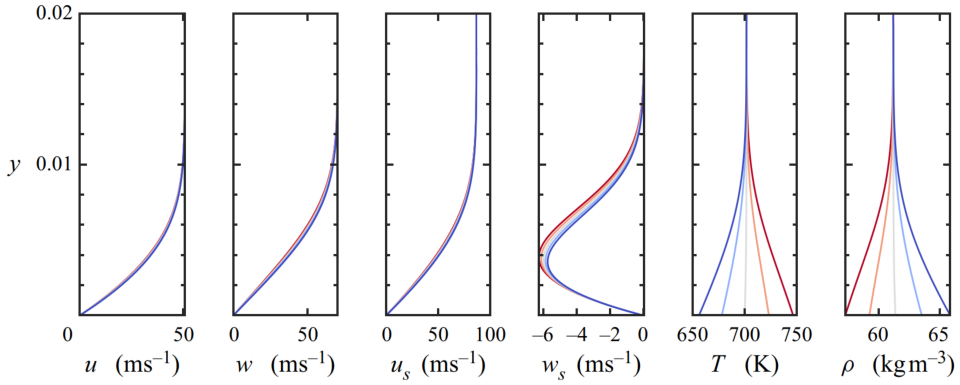

Figure 1.8: The effect of non-adiabatic walls on the baseflow in ideal gas conditions of CO_2 flow at 80 bar pressure. Boundary layer parameters as a function of y at $x = 1$. Subscript s refers to the local streamline direction and e to the boundary layer edge. Reproduced from Ren and Kloker (2022)

on the stability of the CF vortices. It assumes a linear perturbation and the stability computations are performed based on the undisturbed boundary layer. This approach is best suited to local stability computations, as has been highlighted in the work of Haynes and Reed (2000). They show that linear stability theory underpredicts the growth of the CF vortices and that it does not predict amplitude saturation of the stationary CF mode.

Tempelmann, Hanifi, and Henningson (2012), on the other hand, uses the Linear Parabolic Stability Equations (LPSE) to assess the effect of non-adiabatic walls on the stability of the CF vortices. This approach uses the same linear perturbation assumption, hence, it cannot predict amplitude saturation of the stationary CF mode. However, it takes into account the growth of the boundary layer providing a good prediction of the growth of the CF vortices (Haynes & Reed, 2000).

The Effect Of Non-Adiabatic Walls On The Baseflow

Before literature is discussed that studies the effect of wall heating on the development of the CFI, first the effect on the baseflow is further discussed. This is done utilising the computations of Ren and Kloker (2022) displayed in Figure 1.7 and 1.8.

The first observation that can be made from Figure 1.7 is that the streamwise boundary layer edge velocity $u_{s,e}$ (parallel to the local streamline) and the angle (ϕ_e) of the local streamline with respect to the chord coordinates are unaffected by non-adiabatic walls. This is expected as these variables depend on the inviscid conditions and not the conditions inside the boundary layer.

In agreement with the mathematical derivation provided at the beginning of this section, it is found

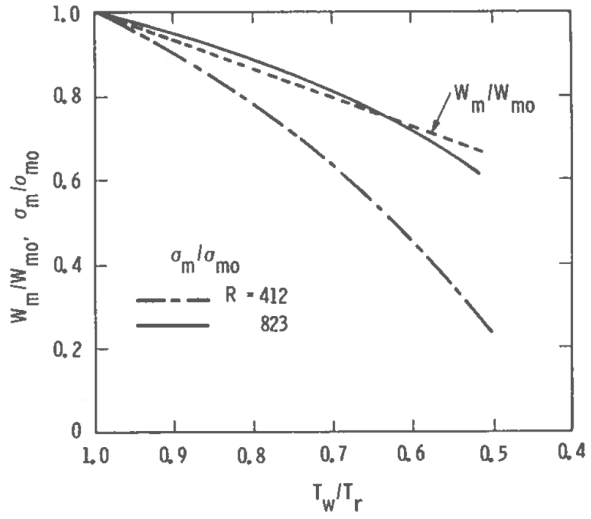

Figure 1.9: Reduction of the maximum crossflow component and maximum amplification rate of stationary CF modes at $R = 412, 823$ as a function of the temperature ratio. Reproduced from Mack (1980).

that wall heating increases the momentum deficit of the streamwise velocity profile. This is also shown in Figure 1.7 as the displacement thickness ($\delta_{1,s}$) is increased by wall heating. Additionally, an increase in the shape factor H is observed.

The results of the mathematical derivation are also confirmed for the effect on the crossflow component (w_s). As the surface is heated, an increase in the magnitude of w_s is observed in Figure 1.8. This is also evident from Figure 1.7 in the $10\text{max}_y(-w_s)$ term.

The numerical results of Ren and Kloker (2022) confirm effects expected based on the mathematical derivation. Therefore, it is now understood that the momentum deficit in the streamwise velocity profile, the magnitude of the crossflow component and the location of the inflection point are affected by non-adiabatic walls and that the modification of these form the basis of the (de)stabilisation mechanism. It can be insightful to understand how the impact of non-adiabatic walls on such parameters is affected by different conditions. The influence of the pressure gradient is especially interesting as this is variable over the airfoil. Mack (1980) reports how the wall temperature ratio affects the maximum growth rate and the crossflow component at two chordwise locations utilising CLST ($s/c = 0.012$ and 0.049, s being the distance along the surface of the airfoil). The corresponding figure is reproduced in Figure 1.9 where σ_m/σ_{mo} is the ratio of the growth rate of the CF vortices between adiabatic and non-adiabatic wall conditions. W_m/W_{mo} is the ratio for the crossflow component. The pressure gradients at these stations ($s/c = 0.012$ and 0.049) are expressed in terms of the Hartree parameter of the FSC boundary layer, these are $\beta_h = 0.67, 0.3$ and have Reynolds Number $R = 412$ and 823 respectively. The effect on the growth rate will be discussed later. However, one can see that only a single line is observed for the reduction in the crossflow component. This suggests that the reduction in the crossflow component by the temperature ratio is independent of the pressure gradient.

The Effect Of Non-Adiabatic Walls As A Function Of The Wavenumber

Lekoudis (1980) investigated the effect of wall cooling on the spatial amplification rates for three chordwise stations close to the LE ($x/c = 0.00189, 0.00580, 0.01222$) considering travelling CF vortices with a frequency of $F = 1000Hz$. These are all within the favourable pressure gradient region of the 35°swept wing computed with a freestream Mach number of 0.891. The effect of the temperature ratio as a function of the wavenumber (k) is shown in Figure 1.10(a). These calculations have also been provided for the other two chord stations, however, they are similar and thus not provided. One can see that wall cooling reduces the amplification rate and that the effect is relatively uniform for the considered wavenumbers. This suggests that the stabilising effect of wall cooling is independent of the wavenumber given a certain frequency. No information is provided by Lekoudis (1980) regarding this relation on stationary CF modes.

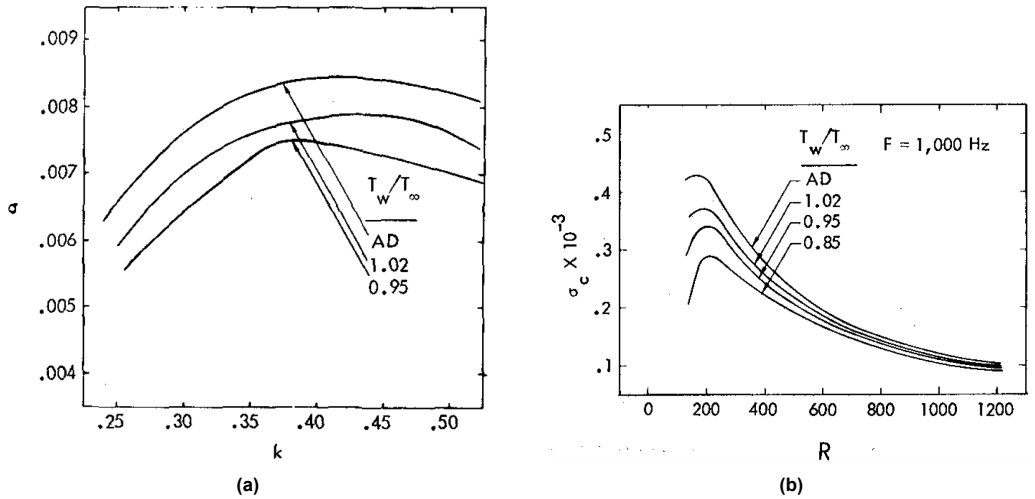

Figure 1.10: Variation of the growth rate (σ) for travelling CF modes with frequency $F = 1000Hz$. Figures are reproduced from Lekoudis (1980). (a) Variation of the growth rate as a function of the wavenumber (k) at $x/c = 0.01222$. (b) Variation of the growth rate normalised by the chord as a function of the adiabatic wall Reynolds number R.

Tempelmann, Hanifi, and Henningson (2012), on the other hand, found that the most amplified spanwise wavenumber (β) decreases with decreasing wall temperature for travelling CF modes. However, Tempelmann, Hanifi, and Henningson (2012) does not specify the streamwise wavenumber (α) to generate k, hence, one cannot directly compare the results. Additionally, Tempelmann, Hanifi, and Henningson (2012) found the optimal condition by also varying the angular frequency. The optimal frequency (least stable in terms of neutral point location) decreases rapidly for decreasing wall temperature. Hence, the frequency changes in the work of Tempelmann, Hanifi, and Henningson (2012) while Lekoudis (1980) evaluates a set frequency, making direct comparison problematic. However, the work of Tempelmann, Hanifi, and Henningson (2012) suggests that, under natural conditions, the dominant wavenumber (based on the movement of the neutral point) is prone to changes in the presence of wall cooling, most likely as a function of a change in the dominant frequency.

Manuilovich and Ustinov (2014) make an interesting conclusion on the interaction between non-adiabatic walls and the spanwise wavenumber (β). They concluded that the (de)stabilising effect of stationary and travelling CF modes (at a constant frequency) is not the same for different spanwise wavenumbers. The results even suggest a destabilisation when a stabilising effect is expected or vice versa. This contradicts the results of Lekoudis (1980). Figure 1.11(a) and (b) display the spatial amplification rate for stationary and travelling CF vortices with surface heating and cooling, respectively. One can see that, in general, surface heating increases the amplification rate for both the travelling and stationary CF modes, thereby destabilising the flow, while a stabilising effect is found for wall cooling. However, as the wavenumber increases ($\lambda \gtrsim 0.45$), one can see that the growth rate (α_i) in the presence of wall cooling becomes larger as the adiabatic growth rate suggesting a destabilising effect. A similar trend reversal is found for wall heating in Figure 1.11(b), but it is less pronounced and occurs at larger wavenumbers. This is an interesting discovery as the (de)stabilisation due to heat transfer has been attributed to the change in the crossflow component, which is identical for all wavenumbers. Manuilovich and Ustinov (2014) attribute this phenomenon to the balance between the stabilising effect of the effective Reynolds number and the destabilising effect of the increased crossflow component. They state that "*with a decrease in the transverse scale of the vortices the zone of their localisation is pressed against the wall occupying the hotter layers of the main flow*" (Manuilovich & Ustinov, 2014, pp. 605). For wall heating this means that as the wavenumber increases (wavelength decreases), the size of the vortices is smaller, and thus, the vortices are located in a (spanwise averaged) hotter region in case of wall heating. As they are located in a hotter region, the kinematic viscosity is increased, reducing the effective Reynolds number which has a stabilising effect. The stabilising effect of this phenomenon may become larger as the destabilisation induced by the increased crossflow component, providing an overall stabilising effect. It is interesting that this trend is similar between the travelling and stationary CF modes.

The study of Manuilovich and Ustinov (2014) is the only one to have noticed this phenomenon. It

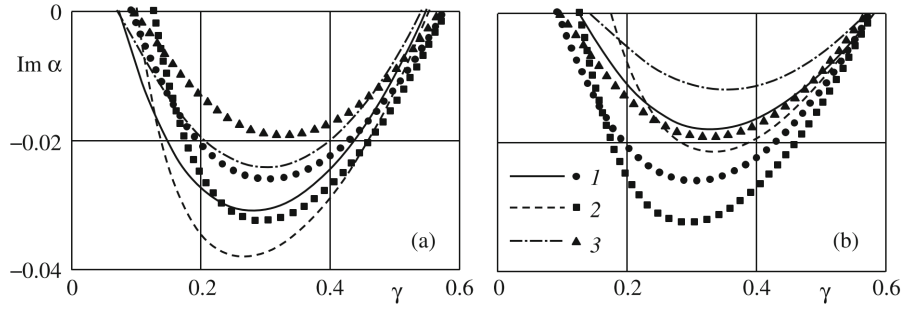

Figure 1.11: Effect of surface cooling (a) and heating (b) on the spatial amplification rate as a function of γ (spanwise wavenumber referred to as β in the rest of the report). 1 is the steady mode ($\omega = 0$) and 2 and 3 are unsteady modes ($\omega = 0.01$ and -0.01 respectively). Markers indicate adiabatic case and continuous lines are the non-adiabatic conditions. Reproduced from Manuilovich and Ustinov (2014).

is interesting to investigate this phenomenon further as it can provide insights into the effect of wall heat transfer on the development of the CF vortices. It is not clear if the trend reversal is relevant to flight conditions as the phenomenon is a function of the thermal boundary layer and the wave number for which the author is not aware of typical numbers, further analysis is required to make a statement regarding this.

The Effect Of Non-Adiabatic Walls On The Local Growth Rate at Different Chordwise Stations

Apart from the changes in the growth rate as a function of the wavenumber Lekoudis (1980) provided results as a function of the chordwise station (see Figure 1.10(b)). For travelling CF modes at $F = 1000Hz$ and a temperature ratio of $T_w/T_\infty = 0.95$ (approximately a 20% decrease in wall temperature compared to the adiabatic case), the local growth rate reduction is found to be 27, 17 and 11% at $x/c = 0.00186, 0.00580, 0.01222$ respectively. This suggests that the stabilisation due to wall cooling (and thus the wall heat transfer effect) is most effective close to the LE while it decreases in effectiveness at downstream positions. A similar plot to Figure 1.10(b) is provided for a stationary CF mode by Lekoudis (1980) showing the same trend. This phenomenon was also observed by Mack (1980) for stationary CF modes when evaluating the amplification rate at two chordwise stations (indicated by a variation of the Reynolds number R in Figure 1.9) as a function of the temperature ratio. One can see that the reduction in growth rate is much smaller at the downstream station compared to the upstream station even though the reduction in the crossflow component is identical.

Lekoudis (1980) nor Mack (1980) explain this phenomenon, however, the studies use the same conditions (sweep angle, pressure distribution, $M = 0.891$) for stations close to the LE. Additionally, the results are generated in the same x/c, hence, the pressure gradient is varied similarly to each other. This has shown to be a sensitive factor on stability in the presence of suction by, for example, Mack (1980), which makes it reasonable that the effectiveness of non-adiabatic walls varies with the pressure gradient. However, this has not been confirmed. Although the work of Ren and Kloker (2022) confirms the stabilising effect of wall cooling on the local growth rate for both travelling and stationary CF modes (see Figure 1.12(a) and (b)). Ren and Kloker (2022) do not present a direct comparison at different streamwise locations, and the visualisation of the results does not lend the opportunity to do so. Consequently, further investigation is required to understand how the chordwise station affects the effectiveness of wall cooling.

Effect of Non-Adiabatic Walls on the Neutral Point

In contrast to the other publications, Tempelmann, Hanifi, and Henningson (2012) focuses on the localisation of the neutral point as a response to non-adiabatic walls using parabolised stability equations (PSE). Tempelmann, Hanifi, and Henningson (2012) identify the neutral point using local computations (growth rate) under the assumption that non-modal growth occurs upstream of the neutral point and modal growth downstream of the neutral point. Tempelmann, Hanifi, and Henningson (2012) locates the neutral point at $x = 101$ for $T_w/T_f = 1.00$, $x = 456$ for $T_w/T_f = 0.5$ and is unable to identify the neutral point at $T_w/T_f = 0.25$ as the boundary layer is fully stabilised. This clearly demonstrates the stabilisation of the modal instabilities by wall cooling albeit that they investigate extreme heating ratios. Interestingly, Tempelmann, Hanifi, and Henningson (2012) find that the cooling effect is reversed between modal and non-modal growth. In Figure 1.13 the N factor is shown as a function of x, one can

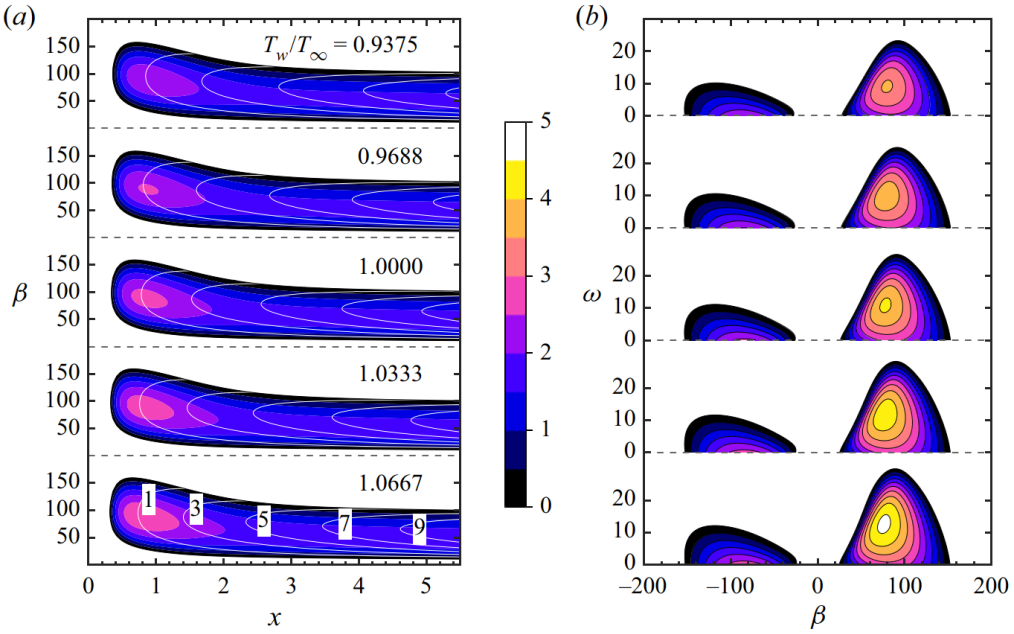

Figure 1.12: Stability diagram under ideal conditions for varying wall temperature ratios. (a) Stationary CF modes with local growth rate as contours and N factor as isocontours. (b) Stationary and travelling CF modes at $x = 1$ with local growth rate as contours. Reproduced from Ren and Kloker (2022).

clearly see a destabilisation upstream of $x = 200$ (non-modal region) by increased wall cooling while a destabilisation is found for the modal growth downstream.

The Effect Of Non-Adiabatic Walls On The Integrated Amplification Rate

In the previous sections, the effect of wall heat transfer on the local amplification rate is discussed as a function of the temperature, wavenumber and chordwise station. Even though the amplification rate is a good local stability metric, it cannot be solely relied upon for the discussion on transition. Due to the lack of a reliable transition predictor for crossflow dominant instability modes, it is common to judge the effect in a relative manner using the e^N method (as is used with TS waves). A comparison of the N factor between the adiabatic and non-adiabatic provides a good indication if the flow is stabilised or destabilised. Consequently, Lekoudis (1980) and Ren and Kloker (2022) provide such calculations to assess its effect on the stability of the boundary layer. The reader is reminded that the CLST methodology (as used by Lekoudis (1980) and Ren and Kloker (2022)) is not considered to be fully accurate for the generation of the N factor. A deviation from the growth in the linear stages of development is expected because of the parallel flow assumption embedded in the CLST methodology. Saturation of the primary CF vortices, however, is not predicted at all as linear disturbances are assumed (Haynes & Reed, 2000).

The N factor obtained by Lekoudis (1980) for stationary CF vortices in the region close to the LE are shown in Figure 1.14. One can see that the N factor is reduced by approximately 16% at $T_w/T_{\text{inf}} = 0.95$ within the investigated domain. This is rather large considering a maximum amplification of 27% which reduced quickly (11% after $0.01x/C$). This has been attributed by Lekoudis (1980) to the effect of integration of the growth rate. This trend is confirmed by Ren and Kloker (2022) who reported the location of several N factors for different wavenumbers and wall heating ratios for the stationary CF mode as visible in Figure 1.12(a). The first location where $N = 9$ is reached at adiabatic conditions is $x \approx 4.9$ while it is reached at $x \approx 4.6$ and $x \approx 5.3$ in case of temperature ratio of 1.0667 and $1/1.0667$ respectively. Evidently, uniform wall heat transfer destabilises/stabilises the BL in the case of wall heating/wall cooling. The former is especially interesting as the location at which $N = 9$ occurs is delayed by approximately 8% for a temperature ratio of $T_w/T_f = 1/1.0667$. Considering that much lower wall cooling ratios may be achieved (Mack, 1980; Reshotko, 1979), there is potential for considerate transition delay. The same stabilising trend of wall cooling with respect to the N factor is seen by Lekoudis (1980) for travelling CF modes, this will be discussed in more detail in the next section.

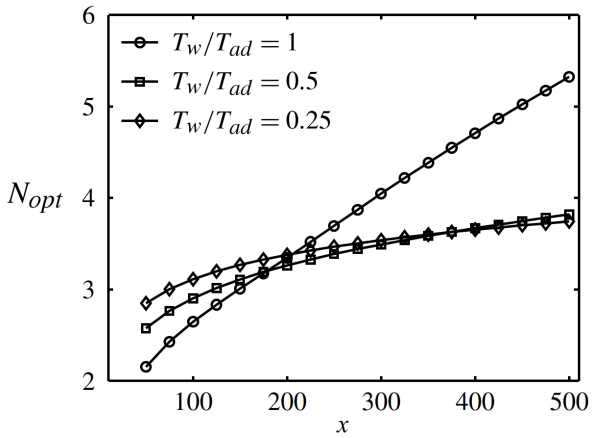

Figure 1.13: Growth in disturbance energy ($N = 0.5log\,(E(x)/E(x_0))$) of the mode that becomes first unstable, x_0 is the initialisation location. Reproduced from Tempelmann, Hanifi, and Henningson (2012)

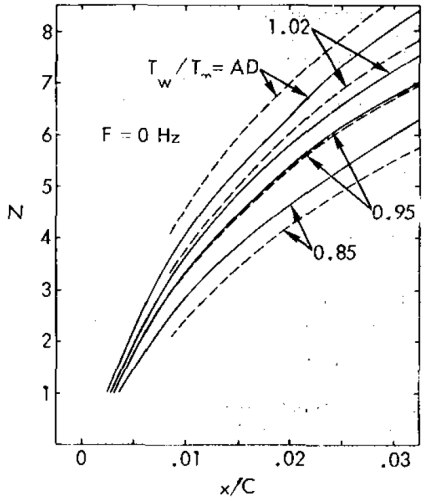

Figure 1.14: N factor at $F = 0Hz$ as a function of the chordwise location for different cooling ratios. The dashed line is obtained with incompressible theory and the solid line with compressible theory. Reproduced from Lekoudis (1980).

A Comparison On The Effect Of Non-Adiabatic Wall Between Stationary And Travelling CF Modes

A similar graph to Figure 1.14 is provided by Lekoudis (1980) for travelling primary CF modes at $F = 1000Hz$. It isn't provided in this document as the overall trends are very similar. Instead, the ratio of the non-adiabatic and adiabatic N factors at $x/C \approx 0.034$ is provided in Table 1.1 for both the stationary and the travelling CF mode. Note that these values are obtained by manually finding the values in the graph and dividing the non-adiabatic cases with the adiabatic cases which means it is prone to read-off errors.

The ratio of the N factor between the non-adiabatic cases and the adiabatic case is very similar between the stationary ($F = 0Hz$) and the travelling ($F = 1000Hz$) CF mode as evident from Table 1.1. This suggests that the expected stabilisation induced by wall cooling impacts travelling and stationary CF modes alike in terms of trend and magnitude. A similar trend between travelling and stationary CF modes was also observed for the local growth rate by Manuilovich and Ustinov (2014) and Ren and Kloker (2022), who found a stabilisation of stationary and travelling CF modes for wall cooling and a destabilisation under wall heating (see Figure 1.12(b)). However, the results of Ren and Kloker (2022) show that the impact (i.e. the magnitude of the effect) of non-adiabatic walls is different between travelling and stationary CF modes. In Figure 1.12(b) one can clearly see that the local growth rate for the travelling CF mode $\omega \approx 10$ is much more affected by the change in wall conditions than the stationary CF mode. Even though this is the local growth rate and not the N factor, one does not expect

the N factor to show a similar impact if the impact on the local growth rate is so different. Additionally, Tempelmann, Hanifi, and Henningson (2012) found that the most unstable frequency for travelling CF modes is drastically decreased by wall cooling. Although this does not indicate that the impact is different for stationary and travelling CF modes, it does show that the stabilisation of the different frequencies by wall-cooling is non-uniform.

T_w/T_∞	1.02	0.95	0.85
$F = 0Hz$	0.90	0.83	0.75
$F = 1000Hz$	0.90	0.85	0.73

Table 1.1: Approximate non-adiabatic and adiabatic N factor ratio (N/N_{ad}) at $x/C \approx 0.034$ based on Figure 1.14 and its equivalent for $F = 1000Hz$ presented by Lekoudis (1980).

Comparison to TS Waves and Suction

The impact of wall heat transfer in the presence of CFI has been challenged as the effectiveness in TS waves (a viscous instability) is related to the modification of viscosity while crossflow instabilities are inflectional instabilities. Therefore, it is worthwhile to touch upon the effectiveness of this technique compared to different techniques or conditions. It has been chosen to limit the contents of this section to the papers that perform the comparison for time-related constraints.

Lekoudis (1980) performed a short comparison between cooling on the stabilisation of TS waves and CF vortices. The temporal amplification rate of the TS waves (at $M = 1.6$) is reduced by a factor of eight with a 20% reduction in wall temperature while a maximum reduction of 27% found for both stationary and travelling CF modes (at $M = 0.891$) at an 18% temperature reduction. Lekoudis (1980) attributes this limited increase in stability to the small reduction in the crossflow component. This implies that the impact of non-adiabatic walls on both the statioanry and travellin CF modes is much less compared to TS waves.

Comparison with suction in the presence of CFI is slightly more difficult as the control technique relies upon different mechanisms. Therefore, Mack (1980) compared the effectiveness by comparing the reduction in the growth rate for a given reduction in the crossflow component. These results are presented in Figure 1.15. It is clear that for a given reduction in the crossflow component, cooling is much less effective in stabilising the flow compared to suction. Mack (1980) attributes this to the mechanism itself, where suction indirectly reduces the crossflow, cooling is even more indirect as the change in the near-wall viscosity and density reduces the crossflow component.

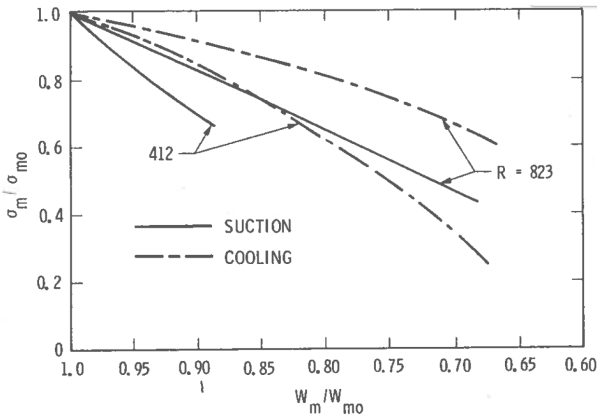

Figure 1.15: Reduction of the growth rate at $R = 412, 823$ for cooling and suction as a function of the maximum crossflow reduction. Reproduced from Mack (1980).

1.4.2 Experimental Investigations With Uniform Non-Adiabatic Walls

Although the numerical simulations of Lekoudis (1980), Mack (1980), Manuilovich and Ustinov (2014), and Ren and Kloker (2022) all suggest that uniform surface heat transfer affects the flow stability, no

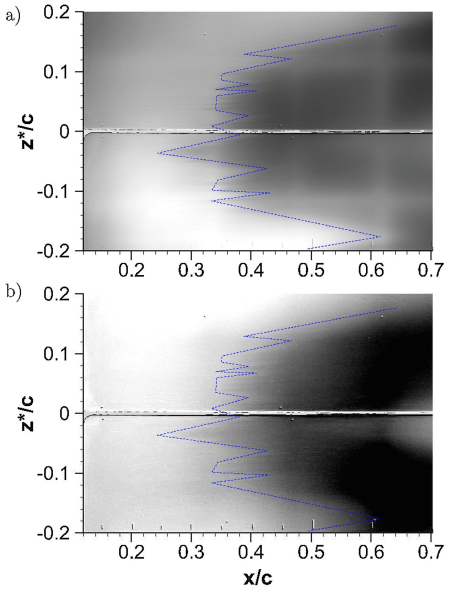

Figure 1.16: TSP image with identified transition line for $T_w/T_\infty \approx 1.04$ (a) and $T_w/T_\infty \approx 1.01$ (b). Reproduced from Lemarechal et al. (2019).

experimental data has been provided to confirm their observations. One of the experimental publications that showed the effect of uniform wall heat transfer upon transition due to stationary CFI is that of Lemarechal et al. (2019), which investigates the application of Temperature Sensitive Paint (TSP) as a transition identification technique. TSP requires thermal gradients on the model to distinguish the laminar from the turbulent region. Therefore, the model must be at a different temperature as the fluid. To assess if the measurement technique affects the transition front, measurements were performed for various heating ratios at which the model is actively heated. The heating equipment of this model has a single power setting, thus, to achieve the variation in the temperature ratio, the heating device was turned off while the measurement equipment and tunnel were running. The recorded images have a black-and-white scale (Figure 1.16(a) and (b)) where a light area represents laminar flow, the dark area represents turbulent flow, the transition front is determined by identifying the largest gradient numerically.

In Figure 1.16, the image with the highest achievable heating ratio ($T_w/T_f \approx 1.04$) and the image with the lowest heating ratio ($T_w/T_f \approx 1.01$) that still has sufficient contrast (according to Lemarechal et al. (2019)) are shown. The blue dotted line indicates the transition front determined computationally, the grey scale is changed for Figure 1.16(b) to increase the contrast. It is clear from the blue line that the heating ratio has little effect on the transition front, indicating that heat transfer does not affect the stability of stationary crossflow vortices. However, the difference in the temperature ratios of Figure 1.16(a) and (b) is only 0.03. This means that the effect may be small, and thus, a movement in transition may not be readily noticeable. Secondly, the small contrast in Figure 1.16(b) increases the measurement error of the identified transition location (as the thermal gradient is less pronounced), which can negatively impact the observations and, therefore, the conclusion on the movement of transition by wall heating. No quantification of this is provided in the error is provided in the work Figure 1.16. Hence, further experimentation is required to confirm this effect on transition.

The negligible movement of transition found by Lemarechal et al. (2019) is in contrast with the trend seen by Fey et al. (2003) when comparing the transition front for temperature ratios of $T_w/T_f = 1.07$ and $T_w/T_f = 0.93$ ($\Delta T_w/T_f = 0.14$ which is considerably larger compared to $\Delta T_w/T_f = 0.03$ of Lemarechal et al. (2019)). Fey et al. (2003) investigated the TSP technology in the European Transonic Wind Tunnel on the DLR-F4 mockup, which has a sweep angle of 27.1°. Fey et al. (2003) found that the transition front on the swept wing was located significantly upstream when comparing the transition location of these temperature ratios. The upstream movement of transition decreased when comparing images of $T_w/T_f = 0.95$ and $T_w/T_f = 1.05$. When the temperature ratio approaches unity ($T_w/T_f = 1.02$ and $T_w/T_f = 0.98$), a difference in the transition location is not readily noticeable, possibly explaining the lack of transition movement found by Lemarechal et al. (2019). However, the results by Fey et al. (2003)

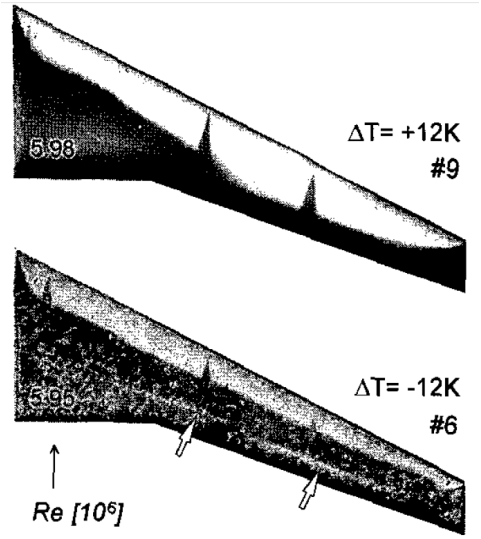

Figure 1.17: TSP images for $T_w/T_f = 0.93$ ($\Delta T = +12\ K$) and $T_w/T_f = 1.07$ ($\Delta T = -12\ K$) with $Re \approx 6 \times 10^6$. Arrows in the lower plot highlight the appearance of shock lines. Reproduced from Fey et al. (2003).

are based on visual interpretations only, and no quantification of the transition movement is performed by Fey et al. (2003). More importantly, despite the specification of the sweep angle, it has not been defined what the dominant instability and transition mechanism was. In a study by Fey et al. (2012), during which the same model, wind tunnel and similar conditions are used, it is argued that transition close to the LE is imposed by stationary CF vortices while TS waves are dominant when the transition is located closer to the Trailing Edge (TE). Utilising this description, one can argue that the transition is imposed by TS waves in the mid-span region for $\Delta T = +12\ K$ in Figure 1.17 ($T_w/T_f = 0.93$) while CFI is dominant in the mid-span region for $\Delta T = -12\ K$ ($T_w/T_f = 1.07$). Here ΔT is the variation of the air temperature. This suggests that a comparison is made between different transition mechanisms for these temperature ratios. For the lower wall-heating ratios, the TSP images are similar to the upper one in Figure 1.17, suggesting that TS waves are dominant. Therefore, one cannot draw conclusions on the effect of non-adiabatic walls on transition imposed by CF vortices based on the work of Fey et al. (2003).

The last experimental framework discussing the effect of non-adiabatic walls upon three-dimensional boundary layer stability is that of Eppink and Wlezien (2011). Eppink and Wlezien (2011) processed data of the NASA/Boeing Hybrid Laminar Flow Control Experiment where local wall cooling was utilised to damp the growth of TS waves in the mid-chord region such that CF vortices are dominant. Because of the temperature control strategy, oscillations of the water and wall temperature were observed as a function of time. Measurements of the boundary layer were performed through Hot-Wire Anemometry (HWA), which requires time. Thus, the temperature oscillations are translated into an oscillation in span. In the experimental data, the presence of a travelling CF mode with a frequency of $350Hz$ was found. Upon analysis of the Root-Mean Square (RMS) for velocity fluctuations in the $f = 200 - 500Hz$ frequency band, it was found that this mode was more stable for the lower wall temperature. This indicates that travelling CF modes are stabilised by wall cooling, confirming the results of Ren and Kloker (2022) that found a destabilisation of these travelling CF modes. The experimental result also agrees with PSE computations run by Eppink and Wlezien (2011) that showed a decrease of the N-factor at the lowest temperature for the travelling CF mode. Stationary CF modes were also found to be stabilised at the lower wall temperature by PSE, however, experimental data shows the opposite trend. Eppink and Wlezien (2011) attribute this to the temperature effect on the hotwire (a correction was applied using an analytical temperature profile).

1.4.3 Studies In Non-Adiabatic Walls Through Strip Heating

It has been shown in the numerical work of Abid and Masad (1996), Masad (1995), and Masad and Nayfeh (1992) and experimental work of Dovgal et al. (1990) that LE heating in two-dimensional boundary layers increases stability as the heated flow sees a relative cold wall in the unstable flow region.

Consequently, it may be interesting to see if the same applies to crossflow instabilities. Such research has only been performed by Dovgal et al. (1990) in an experimental framework utilising a 45°swept flat plate with LE heating. The turbulence intensity was artificially increased to 0.5% to "*obtain the 'natural' transition*". Although this is relatively high, it has been shown by Kosorygin et al. (1988) that the transition mechanism is the same as in low freestream turbulence conditions. A flexible wall above the swept flat plate enforced a favourable pressure gradient. As for the flat plate, the effect of LE heating has been investigated in the case of natural conditions, meaning that no forcing mechanism was present. Dovgal et al. (1990) verify that transition is triggered by crossflow instabilities as streamwise vortices were apparent in naphthalene visualisation. Additionally, the growth of low-frequency disturbances, much lower frequency than TS waves in a similar unswept flat plate setup, were measured.

Whereas it was found that LE heating strips stabilise TS waves, it was found by Dovgal et al. (1990) that the CFI disturbances are considerably destabilised by wall heating across all the reported frequencies ($f = 0 - 300Hz$) at a location far downstream of the heating strip. Secondly, it is reported that irrespective of the magnitude of the heating, transition was found to be located upstream of the adiabatic case.

Although no numbers or detailed trends are provided, it indicates that heating can destabilise CFI. However, no further conclusions can be made, and it does not allow for a further understanding of the fundamental mechanisms as the provided information is limited. It is, for example, unclear if the neutral point is located in the chord region of the LE heating strip and, if so, to which extent the heating strip protrudes into the unstable region of the flow. Considering the mechanism with TS waves, the effect of the heating strip inside the unstable region may be more destabilising than the stabilising effect of the strip in front of the neutral point, thereby destabilising the flow. However, considering the results of Mack (1980) and Lekoudis (1980) that heating destabilises the boundary layer and that this is more effective for upstream locations, it is reasonable that LE heating destabilises the CF vortices, causing transition to occur upstream of the adiabatic wall condition.

1.4.4 Studies In Non-Adiabatic Walls Through Bulk Heating

Apart from the numerical investigation into surface heating, Manuilovich and Ustinov (2014) also investigated the effect of bulk heating on the stability characteristics in three-dimensional boundary layers. One can argue that this technique is difficult to implement as it is difficult to locally heat the thin boundary layer, and any equipment required to do so may introduce a disturbance or turbulence, negatively affecting transition. However, it can give further insights into underlying mechanisms or confirm hypotheses and is therefore discussed.

The difference with surface heating is that the wall-normal temperature gradient is set at 0 instead of a uniform temperature distribution and that heat is added to the fluid according to a certain profile, Manuilovich and Ustinov (2014) used $Q = a\exp\left[-\left(\frac{y-h}{b}\right)^2\right]$ where y is the distance to the wall, h is the distance to the wall at which the maximum heat is added, b is the characteristic thickness and a is a scaling factor to maintain the total heat input. The thermal profiles for the investigated cases are shown in Figure 1.18 where the numbers represent no heating and $h = 0, 1, 2, 3$ respectively for $b = 0.5$. One can see that the maximum temperature is achieved when heat addition is localised at the wall ($h = 0$) and that it decreases as the heat is distributed over a larger wall-normal distance as the heat addition is moved away from the wall. One can also clearly see that the maximum crossflow component is increased as the maximum temperature gets higher.

Lastly, one can see that the wall-normal distance at which the maximum crossflow component occurs increases as the maximum crossflow component increases. This movement of the maximum was also found by Ren and Kloker (2022) for increasing wall temperature.

The increase in crossflow component is normally expected to decrease the stability which is the case for $h = 0, 1, 2$ as can be seen in Figure 1.19. However, as the heat addition is shifted away from the wall, the flow is seemingly less destabilised, for $h = 3$ it can even be seen that the flow is stabilised in comparison to the case where no heating is applied. According to Manuilovich and Ustinov (2014) this stabilisation increases even further as $h > 3$. Manuilovich and Ustinov (2014) attribute this phenomenon again to the balance between the effective Reynolds number and the increase in crossflow component. As the boundary layer becomes uniformly heated the effective Reynolds num-

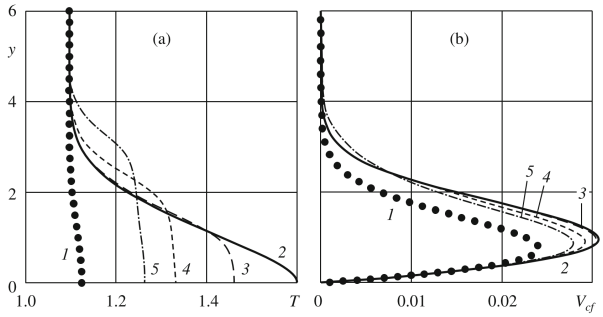

Figure 1.18: Temperature profile (a) and crossflow component (b) for different localizations of bulk heating as computed by Manuilovich and Ustinov (2014).

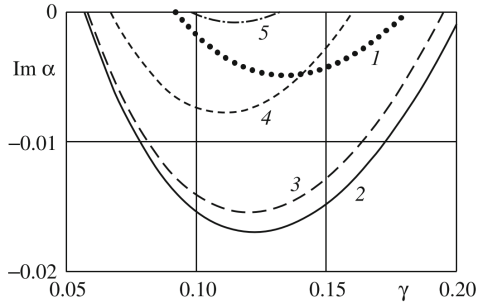

Figure 1.19: Amplification rate as a function of the spanwise wavenumber for the different bulk heating conditions (Manuilovich & Ustinov, 2014).

ber decreases while the increase in crossflow component is found to be limited. The stabilising effect of the decreasing effective Reynolds number thereby becomes dominant over the decreased stability due to the increase in crossflow component resulting in an overall stabilising effect.

1.4.5 Studies In Non-Adiabatic Walls Upstream Flow Deformation: Periodic Heating Strips

As discussed in section 1.3, UFD is a commonly investigated control technique. In the experimental work of Barth and Hein (2022) this technique was applied by artificially exiting a stationary CFI mode with a smaller wavelength as the naturally dominant mode utilising spanwise periodic heating elements. This was done by placing 8 rows of heating elements with a width of 6mm and alternating lengths were placed onto the surface at a 90-degree angle to the LE. The flow measurements were performed using Constant Temperature Anemometry (CTA) in a V-type probe and surface temperature was determined using infrared (IR) thermography.

As one would expect, the spanwise average wall temperature is modified in the presence of such heating rows which therefore may modify the stability characteristics. To quantify this effect upon flow stability, the adiabatic and non-adiabatic spanwise averaged temperature distribution (as a function of x) were measured and included in the Linear Stability Theory (LST) simulations. The used model has been used by Wartemann et al. (2022) for hypersonic flow over a blunted cone with transpiration cooling indicating that it is most likely suitable for compressible and non-adiabatic flows. Barth and Hein (2022) concluded that for the stationary CF modes, the effect is minimally destabilising.

For travelling CF modes, the overall effect was also mildly destabilising except at high frequencies for $0.08 < x/c < 0.3$, here the effect was much more pronounced. However, it has to be noted that the N factors in this region are relatively low ($N < 4.5$) thus it is less likely to trigger transition.

With the actuation of a single heating row during the experiments it is found by Barth and Hein (2022) that the $6mm$ wavelength control mode is successfully activated and that the stationary flow field is successfully rearranged. However, Barth and Hein (2022) find that transition delay is not achieved. The authors attribute this to the waviness of the epoxy surface over the actuators. Barth and Hein

(2022) found that an interaction between the wavenumber excited by the waviness of the surface and the $6mm$ control mode redistributed the stationary CFI such that the control mode was not effective anymore. As a result, the control mode was not suitable anymore thus not affecting stability.

Consequently, it can be concluded that spanwise periodic heating can be used to successfully generate a control mode and thus also provides the potential for transition delay even though this was not achieved in the experiment of Barth and Hein (2022). As the control mode is generated by local variation of the density and viscosity, it is expected that periodic cooling to have a similar result.

1.5 Research Objectives

To conclude, the electrification of the aviation industry comes with the disadvantage of increased drag due to the thermal loads which need to be dissipated. The drag induced by the required thermal management systems may be reduced through surface heat transfer. However, it is not yet fully understood how this affects the stability and laminar-to-turbulent breakdown of the three-dimensional laminar boundary layer and, thereby, the aircraft's skin friction drag. To the best of the author's knowledge, literature discussing uniform non-adiabatic walls on crossflow instabilities is limited to that of Eppink and Wlezien (2011), Fey et al. (2003), Lekoudis (1980), Mack (1980), Manuilovich and Ustinov (2014), Ren and Kloker (2022), and Tempelmann, Hanifi, and Henningson (2012). The numerical results of Lekoudis (1980), Mack (1980), Manuilovich and Ustinov (2014), and Ren and Kloker (2022) indicate that wall cooling stabilises both the stationary and travelling crossflow instability modes using CLST while Tempelmann, Hanifi, and Henningson (2012) showed a clear stabilisation of travelling CF modes with PSE.

Experimental data providing conclusive evidence is not yet readily available. The experiments of Fey et al. (2003) show a downstream movement of transition on a half model (with a swept wing) when the temperature ratio is decreased. However, Fey et al. (2003) do not specify what instability mechanism is dominant and the work of Fey et al. (2012), using the same setup, suggests that TS waves impose transition rather than CFI. Henceforth, one cannot draw definitive conclusions. Lemarechal et al. (2019) experimentally quantified the change in transition in the presence of wall heating. However, this was done for a limited temperature ratio, and the low contrast of the reference picture raises the measurement uncertainty, which is not elaborated upon by Lemarechal et al. (2019). Lastly, Eppink and Wlezien (2011) shows a stabilisation of travelling CF modes by wall cooling. However, the experimental measurements do not show a stabilisation of the stationary CF modes, which is predicted by the numerical work. To the best of the author's knowledge, no other experimental data is available.

As a result, no conclusive experimental evidence is available that confirms the trends found numerically and how accurate these trends are. Secondly, CLST excludes nonlinear terms and Tempelmann, Hanifi, and Henningson (2012) focuses on the neutral point with PSE calculations. Thus, no data is available on the growth in the nonlinear stages of development and the secondary CF instabilities. Hence, it is unknown how the secondary CF instability develops and how transition is affected by the non-adiabatic walls. With the new requirements of the increased thermal dissipation imposed by the new generation of electric-powered aircraft, the main research objective and sub-questions have been formulated as follows:

"Determine the influence of wall heating on the stability and transition of a three-dimensional boundary layer dominated by crossflow instability, through an experimental approach supported by theoretical stability calculations."

1. **What is the effect of wall heating on the mean flow?**
   (a) How is the boundary layer affected by a heated wall?
   (b) How does CBL compare with the experimental results?
2. **How does wall heating affect the primary CF instability?**
   (a) How is the stationary crossflow mode shape affected by wall-heating?
   (b) How does the growth of the stationary crossflow mode compare to experiments in adiabatic and wall-heating conditions?

3. **How does wall heating affect the secondary CF instability and laminar-to-turbulent breakdown?**

   (a) How does wall heating influence the development of the different secondary instabilities?
   (b) To what extent is laminar-to-turbulent breakdown affected by wall heating?

2

Experimental Methodology

In this chapter, the methodology behind the experimental work is discussed. First, the experimental setup will be discussed in section 2.1. Then, the measurement techniques are explained in section 2.2. Lastly, the processing and data analysis steps are shown in section 2.3.

2.1 Experimental Setup

2.1.1 A-Tunnel

The STEP (Swept Transition Experimental Platform) (Rius Vidales, 2022, ch 6.2) has been designed for the rectangular 25 by 100 cm nozzle of the vertical subsonic, open-jet, closed-circuit, anechoic, atmospheric (renovated) A-tunnel facility of the Delft University of Technology. It is well-established that turbulence intensity and surface roughness have a large impact on the development of stationary or travelling CF modes (see Deyhle and Bippes (1996) and White et al. (2001)). Therefore it is important to understand and characterise this quantity. Upon completion of the renovation, measurements of the homogeneity and flow quality were performed for different nozzles, as reported by Merino-Martínez et al. (2020). These show a sufficiently low turbulence intensity for the dominance of stationary CF modes. Further turbulence intensity measurements have been performed with and without the STEP will be discussed in chapter 4.

The closed-circuit configuration of the A-tunnel lacks thermal control of the freestream conditions, and as a result, the air temperature rises due to heat losses of the fans. Additionally, it has been found that the temperature inside the tunnel is highly dependent on the atmospheric conditions outside of the building. As a result, the ambient temperature varies across a measurement plane (of approximately 2.5 hours) and across the different measurement planes which were distributed over approximately two weeks.

2.1.2 Swept Transition Experimental Platform (STEP)

The STEP has been used to gather the experimental data. A picture of the STEP and equipment is shown in Figure 2.1. The swept flat plate (SFP) is contained in the STEP by a set of polycarbonate (optically transparent) side and back walls and a hinged frame at the front that provides access to the SFP and the inside of the STEP. A pressure body is attached to the hinged door that imposes the desired pressure gradient on the model. Measurement equipment mounted to the STEP includes an Optris PI640 Infrared Radiation (IR) camera to observe the wall temperature, a calibration pitot tube for the in-situ calibration of the Hot-Wire Anemometry (HWA) probe, a PT100 (Class B, accuracy of $\pm 0.3\,^{\circ}$C at $20\,^{\circ}$C) for measurements of the ambient temperature, pressure scanners (custom-made with Honeywell HSC series differential pressure transducers with ranges $\pm$160, $\pm$600, and $\pm$2488 Pa with a respective accuracy of $\pm$6, $\pm$9 and $\pm$25 Pa ,mounted on the outside) attached to two rows of 63 static pressure taps, a freestream pitot tube to set the desired Reynolds number and a 3-stage traversing system (consisting of 3 separate Zaber X-LRQ-DE stages) including sting allowing translation of the probes in the global X, Y and Z direction. As will be shown, the length of the string makes it prone to vibrations. These vibrations are measured in the X, Y and Z axes using the ADXL335 accelerometer

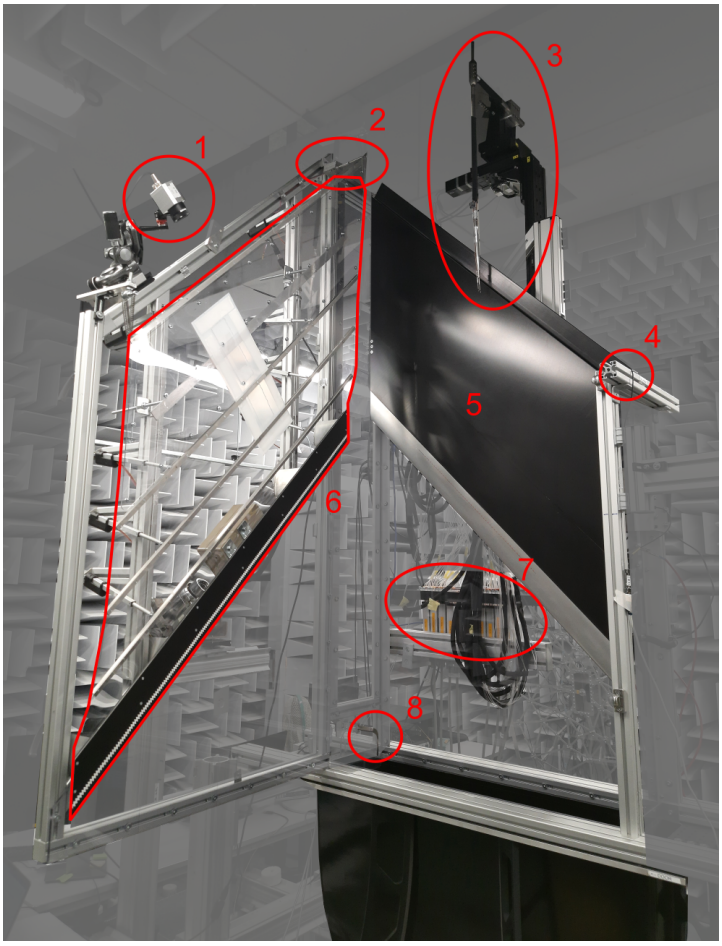

Figure 2.1: Image of STEP as used in the experiments. Equipment attached to the STEP: 1. IR camera, 2. calibration pitot tube, 3. three-stage traversing system including sting, 4. PT100, 5. swept flat plate model, 6. pressure body, 7. pressure scanners, 8. freestream pitot tube.

from Analog Devices. This has a cut-off frequency of $1600\ Hz$ in X and z axis of the STEP and $550\ Hz$ in the Y axis. Although not visible in Figure 2.1, a Taylor-Hobson micro alignment telescope is mounted outside of the STEP aiding the wall-finding process of the HWA and Cold-Wire Anemometry (CWA) probes.

The side walls and pressure body are designed so that the turbulent boundary layer from the contraction and nozzle is bled out to prevent contamination inside the measurement region. The pressure body is made of Polyethylene Terephthalate (PET) foil and is adjustable in shape using linear actuators. In the experimental research of Rajendrakumar (2021), the pressure body has been adjusted such that the pressure gradient is favourable and quasi-uniform over the entire chord and span, providing an excellent basis for fundamental CF-dominated transition research. Therefore, the shape of the pressure body has not been altered. The boundary layer of the pressure body is tripped using a zig-zag strip.

The swept flat plate in the STEP has a sweep angle (Λ) of $45°$ and consists of two separate sections: a downstream section (black in Figure 2.2) that is mounted rigidly to the walls and an adjustable upstream section (blue and grey in Figure 2.2). The upstream section can be adjusted to create steps effect of forward or backward-facing steps can be investigated. The effect of such steps is outside the scope of the current research, and therefore, the step has been minimised as best as practically achievable. A characterisation of the step height and the effect of a heating cycle is shown in chapter 4. A flap is attached to the TE of the model to adjust the stagnation point on the LE.

Both the upstream and downstream sections consist of an anodised aluminium plate except for the modified super elliptical leading edge (thickness of $20mm$ and aspect ratio of 6, grey in Figure 2.2) of the upstream plate which is polished to a surface roughness of $R_q \approx 0.6\,\mu$m (Rius Vidales, 2022).

The combination of the small radius, low freestream turbulence of the tunnel, lack of surface curvature, imposed favourable pressure gradient by the pressure body and optimum sweep angle make the setup susceptible to crossflow instabilities while providing a framework for non-adiabatic boundary conditions. To help the development of the stationary CF vortices, Discrete Roughness Elements (DREs) with a height of 130 µm and a diameter of 2 mm are installed along the neutral point conditioning the stationary CF mode with a spanwise wavelength of $\lambda_z = 10mm$. This wavelength was chosen as this was found to be the naturally most unstable mode using CLST, as presented in chapter 3, under adiabatic surface conditions.

The model is heated using two electrical heating elements (1 for the upstream and 1 for the downstream plate) attached to the back of the model. The power and dimensions of the heating elements are sized accordingly such that a power density of approximately 3.4 W/cm^2 is achieved at both the upstream and downstream heating elements. The silicone heaters are separately controlled by a control module using an on/off control strategy based on thermocouple temperature measurements on the back of the heating elements (i.e. exposed to air on the back). The heating elements have a maximum setpoint of 60°C limiting the achievable temperature ratio. When the setpoint is reached, the heating elements are turned off and the model cools down. When the thermocouple installed on the heating elements reaches 2°C under the setpoint, the heaters are activated again. During the measurements, the heating elements were set at the limit setpoint (60°C) for all non-adiabatic wall measurements and turned off when the adiabatic surface condition was measured.

In this work, two sets of coordinate systems are generally used. The first is a global or tunnel coordinate system expressed in capital letters with the X direction parallel to the freestream velocity, Y is positive in the wall-normal direction and the Z coordinate is orthogonal to X and Y coordinates. U, V and W are the respective velocity components and a visualisation of the coordinate system is presented in Figure 2.2.

The local coordinate system is expressed in lower-case and has its origin on the LE of the midspan (see Figure 2.2). The x direction is orthogonal to the leading edge and is positive towards the downstream direction while y is again aligned in the wall-normal direction of the measurement surface where positive is defined to be pointing away from said surface, z is parallel to the LE and positive pointing towards the outboard. The respective velocity components are u, v and w. The model has a chord length of $c_X = 848.5\ mm$ or $c_x = 600\ mm$ and a span of $b_Z = 884\ mm$ or $b_z = 1250.165\ mm$ with the step located at $x/c_x = 0.397$.

2.2 Flow Diagnostics, Measurement Techniques and Equipment

2.2.1 Selection of Measurement Techniques

A set of measurement techniques is commonly applied in research related to the development of boundary layer instabilities and transition. Commonly applied techniques at the Low Speed Laboratory (LSL) of the Delft University of Technology include IR thermography for the identification of the transition front and Hot-Wire Anemometry (HWA) and Particle Image Velocimetry (PIV) to investigate the development of the boundary layer instability quantitatively.

The transition front detection using IR thermography relies upon the detection of a large gradient in surface temperature due to a change in skin friction as the flow changes from laminar to turbulent facilitated by a (small) difference in the surface and air temperature. However, the current model consists of highly conductive anodised aluminium meaning that no large temperature gradients are present at the model's surface. This renders IR thermography ineffective for the identification of the transition front in the current setup.

HWA, captures the data on a single-point basis, requiring the probe to be traversed across the measurement plane resulting in a substantial measurement time. An advantage of the HWA technique is the high frequency measurements making it suitable for the investigation of unsteady perturbations. A disadvantage of HWA, in the scope of the current work, lies in the measurement principle. The perceived velocity by the HWA is a function of the heat transfer away from the HWA (see e.g. McKeon et al. (2007)). The (convective) heat transfer is a function of both the velocity and the temperature

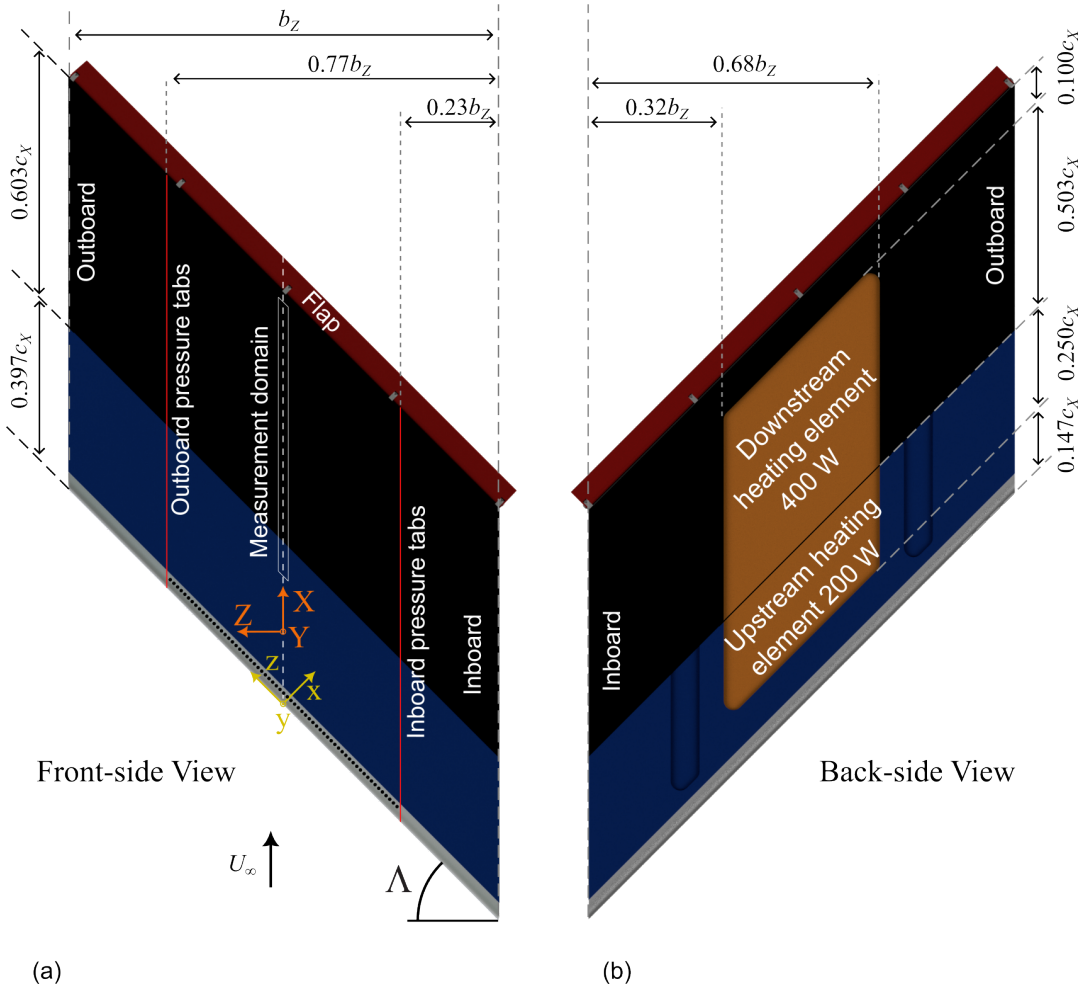

Figure 2.2: Layout and important dimensions of the swept flat plate model. (a) Front-side view (measurement side), (b) back-side view. The grey patch represents the polished LE of the upstream plate, the blue patch the anodised region of upstream plate. The black patch represents the (anodised) downstream plate, and the Bordeaux colour the flap.

difference between the wire and the fluid, and thus, HWA is sensitive to changes in the fluid's temperature. In the presence of a thermal boundary layer, the temperature changes across the boundary layer and thus thermal measurements of the boundary layer are required. In the presence of stationary CF vortices the thermal boundary layer will also be distorted, hence, local temperature measurements are required. Cold Wire Anemometry has been used to perform these thermal measurements. This is not a commonly applied methodology within the LSL of the Delft University of Technology, and hence, it requires additional attention.

Thermal measurements are not required if PIV is used it obtains the velocity by tracking small particles that are introduced into the fluid. An additional advantage of PIV is the high spatial resolution and the instantaneous measurement of multiple velocity components in a plane. This means that the flow information can be captured for a multitude of planes achievable by HWA and less time. Hence, more planes can be measured with PIV and the thermal drift between measurement planes is much lower. However, the frequency of measurements is much lower for PIV limiting the investigations into secondary CF instabilities. Additionally, the required equipment is expensive, and the setup is time-intensive.

The increased spatial resolution and the efficiency of the measurements in terms of time, make PIV measurements beneficial for the research purposes of this thesis. However, the performed work does not only function as fundamental research into the effect of surface heating on the stability of stationary CF vortices. It also functions as a case study bearing in mind a research outlook within the

research group focused on wall cooling. This outlook aims to achieve surface temperatures in the order $-10\ ^{\circ}C$. This surface temperature is well below the typical dew point in the Netherlands. Therefore, dehumidification of the tunnel is required to prevent the formation of condensation or frost on the surface in these experimental conditions. The seeding particle used for PIV at the LSL is a fluid water-glycol mixture which means that the use of PIV introduces moisture into the system. This contradicts the requirement of dehumidification. Hence, bearing in mind the research outlook, PIV was discarded and it was chosen to focus on the HWA and thermal measurements.

2.2.2 Hot Wire Anemometry

A single wire probe has been used to retrieve the flow velocity. The advantage of this is that it is a simple approach; however, it has the disadvantage of being unable to distinguish between velocity components. The output voltage is a function of the wire's heat transfer, which can be separated to be induced by a normal, binormal and tangential component (Jørgensen, 1971). The heat transfer of the tangential component is usually considered to be negligible, and as the wire is positioned parallel to the Z component of the global coordinate system, the perceived velocity by the wire can be expressed to be Equation 2.1. For the derivation, the reader is referred to Rius Vidales (2022, pp. 36-37).

$$Q = \sqrt{(u\cos\Lambda)^2 + (w\sin\Lambda)^2 + v^2} \tag{2.1}$$

The total HWA system consist of three main components: the HW probe, the bridge and the data acquisition equipment. The installed probes are commercially available 55P15 Dantec miniature boundary layer probes with a wire diameter d_w of $5\,\mu$m and length l_w of $1.25\,$mm yielding an aspect ratio $l_w/d_w = 250$.

The HW probe is connected to the TSI IFA-300 Constant Temperature Anemometer (CTA) Wheatstone bridge. A simplified schematic of a CTA system is visualised in Figure 2.3, it consist of four resistances, two fixed resistances (R_a and R_b), a variable resistor (R_v) and the HW probe acting as resistance (R_p). The bridge is balanced when the resistance ratio of the two fixed resistances R_a/R_b equals that of the probe and variable resistance R_p/R_v. As the heat transfer of the wire changes due to thermal or velocity changes, the resistance (and thus temperature) of the wire changes thereby unbalancing the bridge. This imbalance is registered by a high-frequency feedback system that constantly changes the current of the sensor to balance the bridge. The change in current through the probe changes the voltage across the bridge which is the quantity measured by the data acquisition system and used to reconstruct the velocity. Although the temperature of the wire is never truly constant (Perry & Morrison, 1971), the high-frequency feedback system practically keeps the temperature (and resistance) of the wire constant (Ossofsky, 2004), hence referred to as Constant Temperature Anemometry.

The analogue voltage output of the bridge is coupled with the data acquisition system to convert the analogue signal to digital output. This system consists of a NI cDaq-9174 frame and a NI9234 module managed by LabView software. The advantage of the NI9234 module is its high 24-bit resolution, hence, the velocity can be accurately reconstructed. This resolution is especially important for the to-be-discussed CCA system as the CW has a low sensitivity of voltage to temperature depending on the operating current.

Calibration

Under conventional conditions, it is assumed that the temperature is constant along the boundary layer, and consequently, the output voltage of the HWA probe can be directly related to velocity. This is an important assumption as the output voltage is a function of the heat transfer of the wire and thus the fluid velocity and temperature. As the surface is heated, a thermal boundary layer develops and this assumption is no longer valid. Consequently, the output velocity of the HWA needs to be corrected for the temperature.

A calibration method has been proposed by Hultmark and Smits (2010) that directly couples the fluid temperature into the calibration of the HW for CTA and CCA systems. For a CTA system, the convective heat transfer away from the wire is balanced with the joule heating of the wire such that Equation 2.2 is satisfied where. E is the bridge output voltage, $\Delta T = T_w - T_f$ (wire T_w and fluid temperature T_f), k is the thermal conductivity of the fluid, d is the diameter of the wire, A is the surface of the wire and Nu is the Nusselt number. The Nusselt number is a function of the Prandtl number, which has a small sensitivity to temperature variation, and the Reynolds number $Re = Qd/\nu$ with ν being the kinematic

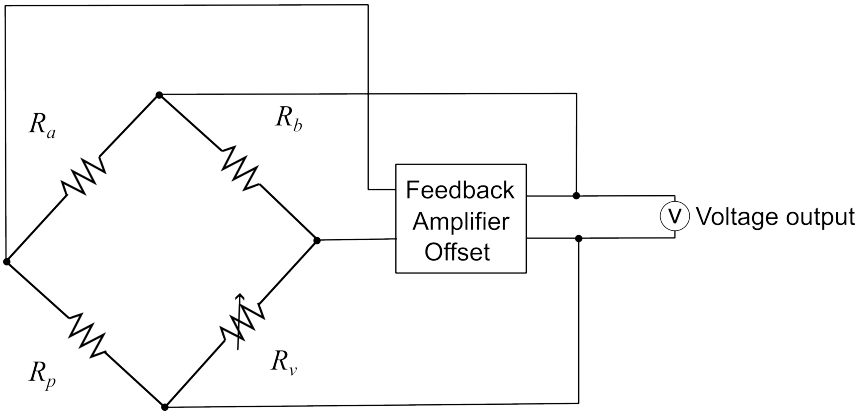

Figure 2.3: Simplified schematic of a CTA system.

viscosity and Q the fluid's velocity perceived by the wire sensor. Consequently, Equation 2.2 can be rearranged into Equation 2.3 which in turn can be expressed as Equation 2.4 as d is constant. ν and k are to be evaluated at the film temperature of the wire which is assumed to be $T_{film} = 0.5(T_w - T_f)$.

$$\frac{E^2}{R} = h\Delta TA = \frac{k\mathsf{Nu}}{d}\Delta TA \tag{2.2}$$

$$Re = f_1\left(\frac{E^2}{k\Delta T}\right) \tag{2.3}$$

$$\frac{Q}{\nu} = f_2\left(\frac{E^2}{k\Delta T}\right) \tag{2.4}$$

The advantage of this approach is that the effect of a temperature change is integrated into the calibration such that no rudimentary temperature corrections are required during the processing stage increasing the accuracy nor requiring double parameter calibrations where the calibration process needs to be repeated at multiple temperatures. It has been shown by Hultmark and Smits (2010) that this method works well for temperature variations of up to 15K (maximum investigated by Hultmark and Smits (2010)) which is similar to the temperature variation within the boundary layer of the current research (maximum variation of 18.4K) and the calibration method is considered to be suitable. By treating the temperature obtained with the CW as the fluid temperature when evaluating ν, k and Equation 2.4, the velocity is obtained easily and accurately considering variations in temperature across the boundary layer. It has to be noted that this approach is limited to low-speed flows as the film temperature assumption made by Hultmark and Smits (2010) is an oversimplification for higher speed subsonic flows as discussed by Cukurel et al. (2012).

Calibration of the HW probe has been performed daily before the start of any measurements. The HW probe was repositioned close to the TE within the bounds of the model and the pressure body and the calibration pitot (as encircled in Figure 2.1) was relocated close to the probe with the static ports on the same chordwise station as the wire sensor. The calibration was performed by varying the flow velocity between 0 and 26 m/s. This range is slightly larger as the expected flow velocities. The obtained data points are expressed in the form of Equation 2.4 through which a fourth-order polynomial is fitted and used in the post-processing phase to reconstruct the velocity.

2.2.3 Cold Wire Anemometry

As explained, local temperature measurements are required of the boundary layer to correctly obtain the the velocity from HWA. CWA (Cold Wire Anemometry) method has been used in the current work for these thermal measurements. The fundamental principle of the CW method compared to the HW method is to reduce the sensitivity of the output voltage to velocity such that the output voltage is only proportional to the temperature and its fluctuations, this can be achieved by setting the overheat ratio a_w close to zero. McKeon et al. (2007) note that the Constant Temperature Anemometry (CTA)

approach is not reliable at such low overheat ratios due to a nonlinear response at such ratios and that the feedback loop loses efficiency, however, the Constant Current Anemometry CCA approach is commonly applied with cold wires. McKeon et al. (2007) have derived the ratio of the sensitivity coefficient of the temperature and velocity using King's Law to be Equation 2.5 for the CCA approach. It is evident from Equation 2.5 that a low current is required to reduce the relative sensitivity of the voltage to the velocity relative to the temperature thereby setting the overheat ratio low. However, practical concerns such as the frequency response of the CWA and the signal-to-noise ratio typically limit the minimum achievable current McKeon et al. (2007).

$$\frac{S_{T_a}}{S_{U_1}} \simeq -2\left(A + B\sqrt{U}\right)\frac{1}{I_w^2} \tag{2.5}$$

For the CW, the same 55P15 Dantec miniature boundary layer probe is used relatively which has a rather low aspect ratio ($l_w/d_w = 250$) compared to conventional cold wire probes (typically $l_w/d_w = 400$ as reported by McKeon et al. (2007) and Tsuji et al. (1992)). The decrease in the aspect ratio increases end losses thereby decreasing the frequency response (Tsuji et al., 1992). However, only the mean temperature is considered in this work to correct the HWA calibration procedure. Future research should investigate the effect of using the mean temperature to study the unsteady content of the HWA signal.

The CW probe was connected to a system comprising of the DISA 55M01 main unit and the 55M20 Temperature (CCA) bridge. The current intensity has been set to 0.2mA, resulting in a sensitivity to temperature of $\Delta V/K = -0.011$. The velocity sensitivity was found to be low at this current (delta of $0.0028V$ for $U_\infty = 0$ and $14.1\ m/s$).

Calibration

Calibration of the CW was performed daily before the start of the measurements. A controlled thermal environment was created by placing a space heater directly underneath an approximately 1-meter aluminium tube in which the tip of the sting was lowered into the top end. The reference temperature was obtained using a PT-100 at a similar height as the CW, in this configuration it was found that the temperature measured by the PT-100 displayed asymptotic behaviour, therefore, the calibration was performed when the PT-100 measurements approached its asymptote which typically took 30 minutes.

The linear response of the CW to temperature permits to limit the number of data points for the calibration to a theoretical minimum of 2, therefore, one data point was generated at ambient conditions and another at higher temperatures by turning the space heater to its maximum setting. To reduce the error of the calibration, one could introduce an intermediate data point to the calibration, however, it was found that this had little to no effect on the calibration while the total time of the calibration approximately doubled. Accordingly, it was decided to limit the calibration routine to the ambient temperature and the maximum heating setting of the space heater.

2.2.4 Double-Wire Configuration

It has been chosen to perform the measurement using a double-wire configuration as opposed to repeating the plane with a single and alternating the function of the probe as HWA/CWA. The advantage of the double-probe design is that it limits the total required measurement time of a plane and the tunnel's thermal drift.

In the double-wire configuration, the spacing between the two probes determines the number of extra data points required to guarantee that measurements are available in the desired domain for both the HWA and CWA probes. The larger the spacing between the probes, the more measurement points are required, the larger the total measurement time and the larger the thermal drift of the tunnel between the HWA and CWA measurements inside the desired domain. Hence, one wants to limit this spacing. Ideally, one would develop a custom probe as this allows a small spacing of the Hot Wire (HW) and Cold Wire (CW) sensor, however, this was not feasible in the current work given available facilities and time constraints. Instead, the original sting end was adapted yielding the design displayed in Figure 2.4. This design features a spanwise offset of $6\ mm$ where the middle of the wires coincides with a line parallel to the LE (i.e. 45°angle). It was chosen to use the most downstream probe in CWA mode as the potential blockage or wake of the upstream probe is more problematic for velocity measurements than the thermal measurements (which are mainly used to correct the HWA measurements).

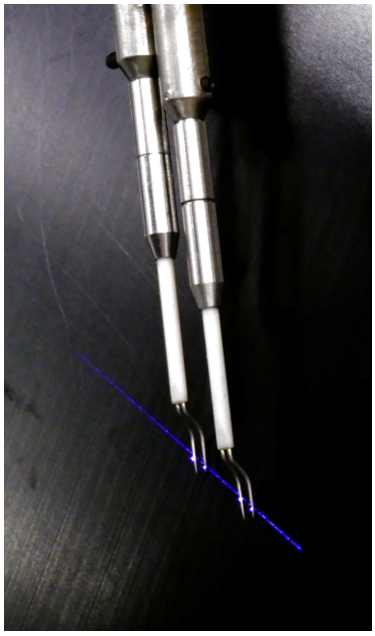

Figure 2.4: Double wire configuration parallel to the LE, CW probe is positioned on the outboard side (left in this figure) and the HW probe is positioned on the inboard side (right in this figure). Blue line projected onto the probes is parallel to the LE.

2.2.5 Discretisation of Measurement Planes

Two separate types of measurements have been performed, the first type quantifies the development of the CF instability through measurements in the zy plane (parallel to the LE in the wall-normal direction) at different chordwise stations. The other type of measurement provides insights into the change in laminar-to-turbulent breakdown by wall heating through measurements in the xz plane (parallel to the wall) at different wall-normal coordinates. The time-intensive HW measurement method requires careful consideration and planning of the measurement planes and the resolution. This is especially important in the current work as the double wire configuration increases the required measurement points to cover the same measurement domain due to the spanwise offset between the probes. The span of the measurement domain (both xz and zy measurements) has been chosen to cover three wavelengths of the crossflow vortices in the spanwise direction. As a trade-off between the spatial resolution and measurement time, this span has been discretised into 54 points, yielding 69 points in z to cover the full measurement domain with both the CW and HW probes. In the yz measurement planes, 42 points are measured in y covering approximately $1.25-1.4\delta_{99}$ depending on the measurement plane using the boundary layer results output from the CBL solver (see chapter 3) as reference.

The coordinates of the xz planes are based on in-situ processing, zy planes were analysed to identify where breakdown approximately occurred in chord to increase the spatial resolution in the region of interest. The same xz plane was measured at two wall-normal distances: one approximately at the maxima of the lower lobe in the steady disturbance profile and one approximately at the upper lobe (see Figure 5.6).

It has been chosen to perform the planes at the same absolute wall-normal distance under both the heating and adiabatic conditions for the sake of simplification. The height of the lobes is slightly different at these conditions, this is especially evident for the upper lobe. Consequently, the localisation of the measurement plane in the vortices is slightly different for the heated and adiabatic conditions. To mitigate the effect, the plane has been chosen to be measured at the approximate average of the adiabatic and non-adiabatic lobe heights. The localisation of the measurement plane will also vary slightly for the different chordwise coordinates as the plane is parallel to the wall while the boundary layer and vortices grow as x/c_X increases. Consequently, the approximate average of the obtained lobe heights at the start and end coordinates is averaged to obtain the final wall-normal coordinate.

2.2.6 Infrared Thermography Camera

An infrared (IR) Optris PI 640 camera with a 90-degree lens was installed to observe and register the wall temperature during the experiments. Initially, the camera was mounted behind the pressure body such that the lens was nearly parallel to the surface observing a considerable portion of the surface. In this configuration, an IR transparent foil is required as the material of the pressure body is not transparent to the spectral range of the camera. The registered wall temperatures showed non-physical temperatures, this was found to be the result of an interaction between the IR camera and the IR foil. Hence, the camera had to be repositioned and it was placed close to the TE, looking towards the LE, while limiting blockage imposed on the outflow of the measurement region. It was chosen to observe and calibrate for a single point on the surface as a reference.

A total of 100 measurement samples were obtained with a frequency of $0.33Hz$ at the beginning of each measurement plane. Calibration of the camera was performed by setting the emissivity in the software such that the IR measurement matches that of a thermocouple temporarily placed on the surface with the wind tunnel turned off and the heaters turned on. The emissivity of the anodised plates was found to be $\epsilon = 0.81$.

2.3 Processing and Data Analysis

2.3.1 Treatment of CW Measurements

During the experimental campaign, erratic behaviour of the CCA device was observed including jumps in the output voltage, drifts in voltage, localised peaks in the voltage and short high noise periods in the signal. As the velocity measurements are corrected with the temperature measurements, it is important to understand the limitations of the CCA measurements and how the data is treated to retain valuable information. The treatment of the CCA data consists of two steps: first the mean temperature of the time signal is obtained at each spatial measurement location, and then a temporal drift of the CCA is corrected.

Temporally Averaged Voltage

In the current work, only the mean temperature at each spatial measurement point is required as the effect of a thermal boundary condition on the development of the stationary CF vortices is being investigated rather than the effect of thermal fluctuations. Typically, this would be rather straightforward, however, the output signal of the CCA displayed erroneous behaviour, thereby complicating the matter. To illustrate the problems encountered with the CCA output signal, typical output voltage signals as a function of time are shown in Figure 2.5. Figure 2.5(a) represents a nominal output signal without significant anomalies in the signal. The sinusoidal wave pattern is created by the internals of the CCA device and does not pose a problem within the current research scope as only the average temperature (and thus voltage) is required at a measurement point. Figure 2.5(b) shows a voltage signal with clear jumps in voltage, these jumps are identified to be non-physical. Peaks in the voltage signal are present in Figure 2.5(c) while (d) showcases a signal with a high (local) noise level. These signals are all considered non-physical while they affect the obtained voltage when averaging the signal, therefore, processing of the data is required to obtain the mean temperature. The combination of local peaks, local high-noise signals and jumps in voltage make commonly used data smoothing or outlier detection techniques unsuitable as a one-size-fits-all solution. Consequently, an alternative method is used to retrieve the temperature based on the rationale that the peak of the histogram is not affected by high-noise periods or local peaks. A voltage jump affects the histogram as a second lobe appears in the histogram, however, it is difficult to quantify which voltage corresponds to the physical temperature in a signal with voltage jumps. A second lobe also appears for regions with strongly distorted mean flow (see next paragraph) this might be physics induced and one cannot simply discard one. Hence, the mean voltage is obtained by computing the weighted average of the peaks of the histogram. Low peaks are discarded if they are below a set threshold of the maximum observed peak, in the current work the threshold was set to 80%. The data is smoothed by obtaining the Probability Density Function (PDF) generated with the 'Epanechnikov' kernel density estimation function (Epanechnikov, 1969) to ease the identification of these peaks. An example of such a histogram and PDF is shown in Figure 2.6.

As metioned, a complication of this routine is that the development of a (second) peak in the PDF correlates with the structure of the crossflow vortices at chord stations where they are further developed. A spatial overview of the measurement locations where two or more peaks are identified is shown in

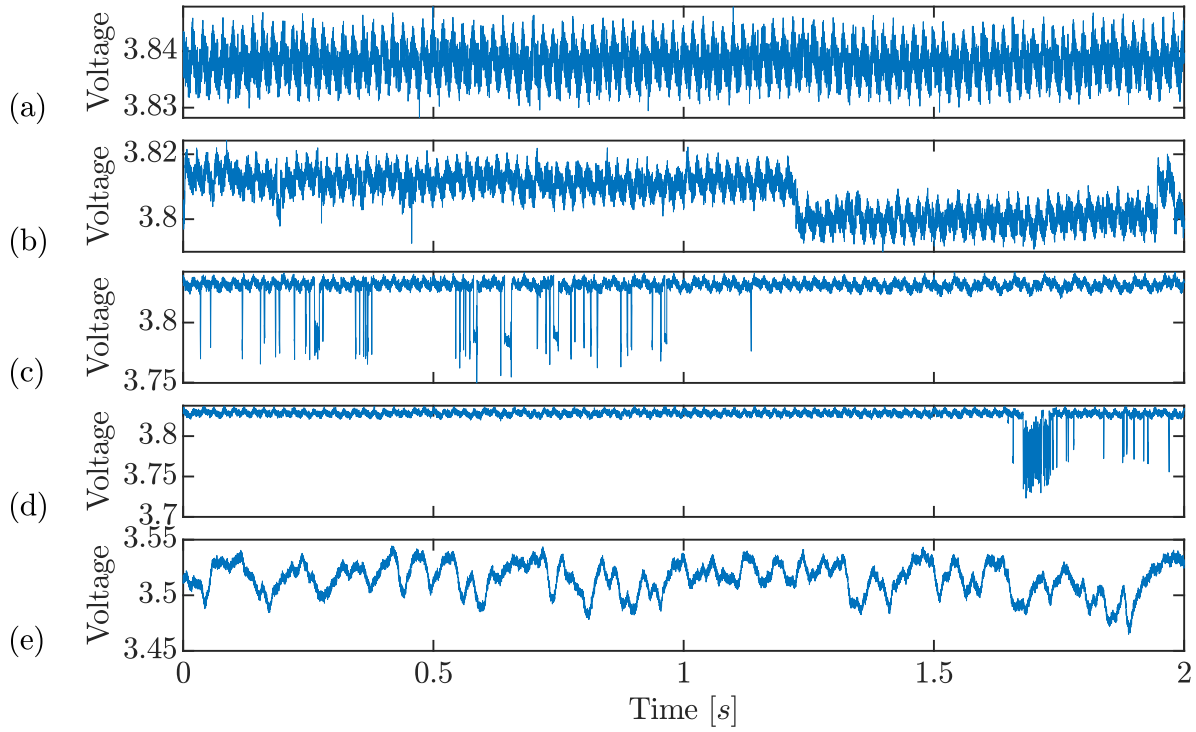

Figure 2.5: Examples of CCA output signals. Nominal signal (a), jumps in voltage (b), local peaks in voltage (c), voltage with local high-noise level (d), signal affected by flow physics (e).

Figure 2.7 for the 1st (weak crossflow instability) and 6th (saturated primary mode) plane under heated $H.X$ and adiabatic $A.X$ surface conditions. Red indicates a point where two or more peaks above the threshold are detected, the yellow colour represents the points where only a single peak is detected. $H.6$ clearly exhibits structures similar to the velocity field while this is not present in $A.6$, hence demonstrating that the presence of the non-adiabatic boundary condition affects the PDF through either interference of the heating elements with the CW or physical thermal fluctuations. In $A.1$ the heating elements are not turned on thereby demonstrating that the problem is not fully isolated to the heating elements. Unfortunately, it is difficult to distinguish between physics-induced peaks and 'random' peaks, combined with time constraints it was decided to use the current described methodology without further iteration.

Drift Correction

Apart from erroneous voltage signals at each data point, the CCA was found to drift in time. To correct this, CCA measurements (external flow data points) are compared to PT100 measurements (positioned in the outflow of the measurement region, see 4 in Figure 2.1). Unfortunately, one cannot directly compare these measurements as the obtained CWA measurements show a certain degree of 'oscillations' (see Figure 2.8), thus the data was linearly fitted. Comparison of this fit with the PT100 data provided an offset as a function of the span (and thus time), which is applied to the CWA measurements, providing the results displayed in Figure 2.8. This step is applied after the temperature is retrieved using the methodology discussed in the previous section.

As an offset is applied to the CWA measurements, one assumes that the drift of the CCA device is caused by the offset applied to the incoming signal rather than the gain. This assumption is valid as the slope of the different CWA calibrations was consistent while the voltage offset was prone to changes. Additionally, the drift was present in both adiabatic and heated surface conditions, confirming that this is equipment-induced rather than physical.

Cause of erratic behaviour

It is evident from Figure 2.7 and 2.8 that the processed data still shows erratic behaviour that one would like to eliminate for future research purposes. Several attempts were made during the experimental

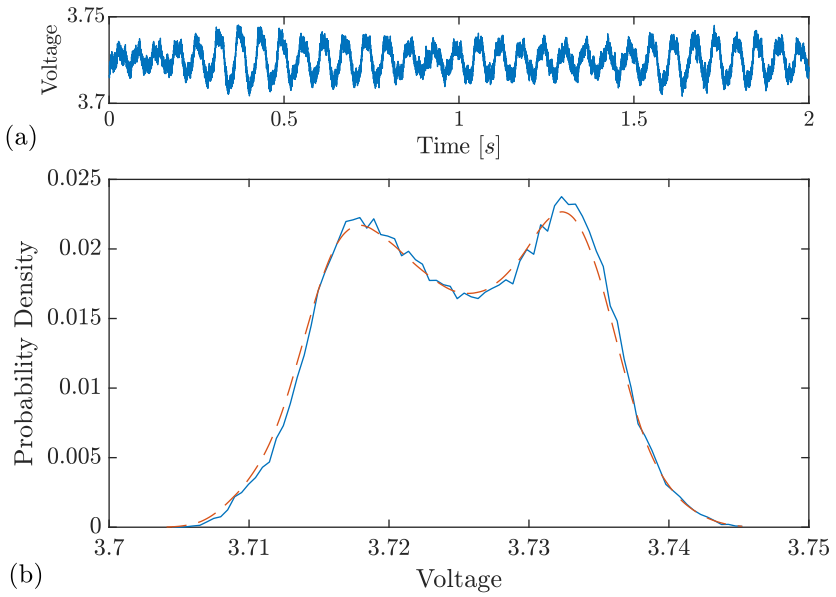

Figure 2.6: Example of a CW signal (a) with two peaks in the PDF (b). — in (b) represent the probability density function as calculated using the histogram method, - - is calculated using the Epanechnikov kernel density estimation function.

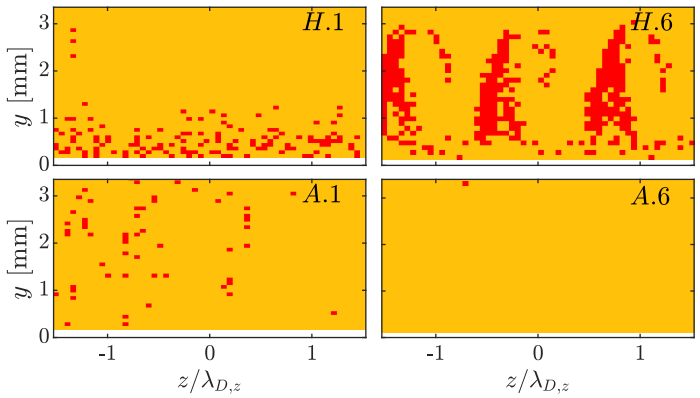

Figure 2.7: Spatial overview of signals with two or more peaks in the PDF, red blocks indicate the 2 or peaks in the PDF of the CW signal at the corresponding measurement locations, yellow relates to a single peak. A peak threshold of 0.1 has been used to generate these pictures.

campaign to resolve the issue. Unfortunately, these attempts were inconclusive. Post measurements, several more attempts have been made and one of the BNC cables of the CWA probe holder exhibits damaged shielding. Swapping this cable led to better results. Hence, it is expected that the temperature measurements will be of higher quality in future research.

2.3.2 Mapping of CWA Measurements on HWA Measurement Domain

Prior to the retrieval of the velocity measurements in the zy plane, the thermal measurements need to be mapped onto the HWA measurement domain. Knowing the offset between the HWA and CWA probes, one knows the physical measurement locations of the CWA yielding a similar overlap to that of Figure 2.9. As one can see, the domains do not fully overlap each other in Y hence the absolute Y measurement locations differ slightly as is also the case in the Z coordinate. The CWA measurements are interpolated to obtain the temperature at the HWA measurement points. If the CWA measurement domain is located closer to the wall, then thermal measurements are missing in the freestream. However, the temperature shouldn't vary in the freestream, and thus, one can extrapolate by using the nearest points. A linear extrapolation is used if thermal measurements are lacking near the wall.

The same approach is used for the xz planes by switching the Y coordinate to the X coordinate.

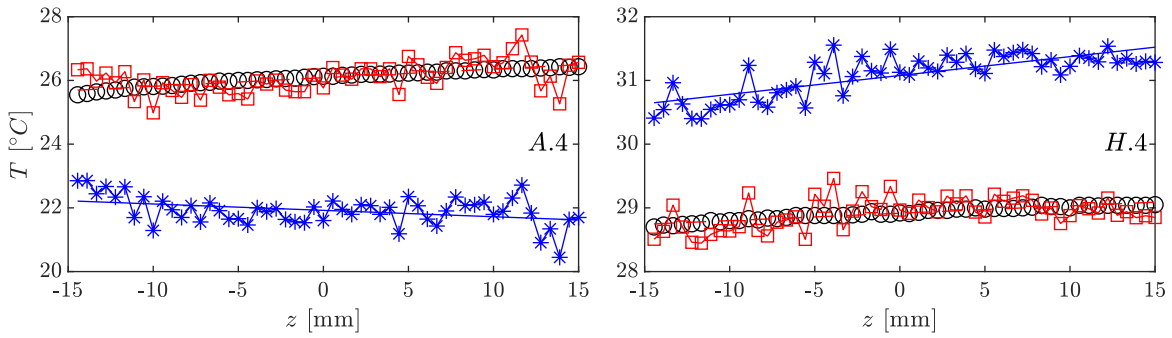

Figure 2.8: Visualisation of drift correction for measurement planes 5 and 7 under heated surface conditions. Uncorrected CWA measurements (-∗-,blue), linear fit through uncorrected CWA measurements (—,blue), PT100 measurements (○, black), linear fit through PT100 measurements (- -, red), CWA measurements corrected for drift (-□-, red).

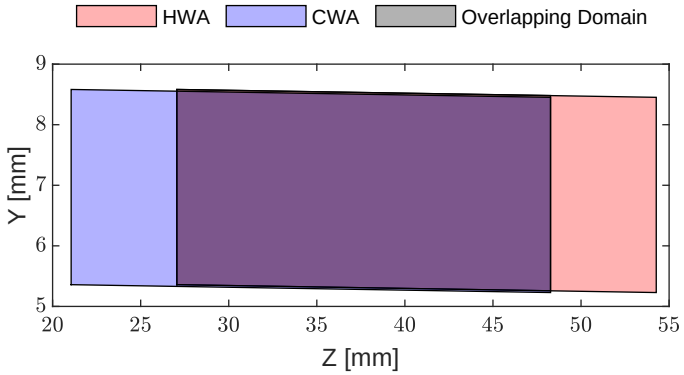

Figure 2.9: Measurement domain of HWA and CWA measurements and its overlap for a zy plane in the traverse coordinates.

However, these planes lack measurement points in the freestream, thus, one cannot correct for the drift and the corresponding correction is not applied introducing an error in the obtained velocity. An additional error is introduced as the CWA probe is positioned at a slightly different wall position than the HWA probe and, hence, at a different height in the thermal boundary layer. The error introduced by this difference is negligible in the freestream but much more critical for measurements close to the wall as the thermal gradients are large close to the wall. Fortunately, the purpose of the xz planes is to asses laminar-to-turbulent breakdown which will be performed using the RMS of the velocity fluctuations in a certain frequency range. Although the RMS has sensitivity to the temperature, it is less important than initially portrayed.

2.3.3 Wall Finding

When performing HWA measurements, it is often necessary to estimate the position of the wall in the HW's coordinate system, als0 in the current research. The approach used in this work follows the 'slice' procedure as discussed by White and Ergin (2004). The approach will be discussed in this subsection.

When performing the measurements, it was chosen to start the velocity and temperature measurements outside the boundary layer and traverse towards the surface. As the HW probe comes close to the wall, conduction between the prongs and the surface can occur resulting in a kink or tail in the velocity profile with the measurements close to the wall. White and Ergin (2004) chose to circumvent this problem and the risk of touching the wall by limiting the measurements to velocities higher or equal to 18% of the external flow velocity. In the current research, such a limit has not been used, instead the wall was found by moving the probe closer to the wall until the velocity signal showed signs of conduction to the wall. Consequently, a tail is present in the unprocessed velocity profiles which are identified and omitted in the post-processing stage.

Next, in accordance with the methodology of White and Ergin (2004), a least-square fit is performed

through the remaining measurements which have a value less than 35% of the external flow condition, the least-square fit is then extrapolated to find the point $\bar{Q} = 0$ (following the no-slip condition at the surface) and the velocity profile is shifted in y accordingly. This process is repeated for each spanwise position independently, however, dependent upon the modulation of the base-flow and thus the upwelling of low-momentum fluid and downwelling of high-momentum fluid, too little measurement points may be present for a least-squares fit that satisfy the 35% freestream criterion at a spanwise station. Consequently, this routine is only performed for spanwise stations with three or more measurement points satisfying the criterion. On the remaining points, a least-squares fit is performed after the spanwise locations that show a large random error are removed through outlier detection. The wall coordinate is then defined as the value of the least-squares fit in the middle of the measurement domain.

In ideal conditions, one would perform a similar routine to find the wall in the temperature profiles before correcting the HW measurements for optimal accuracy, however, the condition at the surface is not as straightforward as with velocity. To use a similar approach, one would require accurate surface temperature measurements and, dependent on the model, a spatial resolution high enough to distinguish temperature variations in span due to the up-and downwelling regions. In the current research, this was found to be unfeasible and as an alternative, a less accurate visual approach was taken. When the wall was found during the experimental campaign, the distance between the probes and the wall was measured and documented using a Taylor-Hobson micro-alignment telescope. The offset between the probes is obtained by taking the average of the difference in wall distance of the HW and CW probe at the two outer points of the domain. This offset is then applied to the CW measurement domain prior to the interpolation of the temperature from the CW measurement domain to the HW measurement domain as discussed in the previous section.

2.3.4 Analysis of Steady Disturbances

The obtained HWA data is processed depending on the interested quantities. For the analysis of the steady disturbance, the first interesting parameter is the temporally averaged velocity($\bar{Q}$) as this provides a qualitative insight into the development of the stationary crossflow instability. The steady velocity profile can then be obtained through spanwise spatial averaging of the $\bar{Q}_z$, this parameter is essentially a combination of the baseflow and the mean of the steady disturbance.

The steady disturbance profile ($\langle q' \rangle_z$) is computed following the methodology used by Downs and White (2013), Serpieri and Kotsonis (2016), and White and Saric (2005). Its computation is provided in Equation 2.6 where n is the number of measurement points in the spanwise direction. It provides a good insight into the development of the crossflow instabilities for two reasons. It gives an indication of the strength of the disturbance thereby providing the possibility to track its growth in space. Secondly, it provides an indication of the onset of nonlinear interactions.

$$\langle q' \rangle_z = \sqrt{\frac{1}{n} \sum_{j=1}^{n} \left(\bar{Q}(y, z_j) - \bar{Q}_z(y) \right)^2} \tag{2.6}$$

However, it has been found that the disturbance profile is prone to noise in the signal and it combines the primary mode with the harmonics while in the current work only the primary mode is computed in CLST. Hence, the disturbance profile has also been calculated through a spatial FFT-iFFT reconstruction. Depending on the interested quantity different harmonics are chosen to be reconstructed. This is expressed in Equation 2.7 where $(0, n)$ indicates the n^{th} harmonic of the primary CF mode.

$$\langle q' \rangle_{z,(0,n)} = FFT \left(\bar{Q}(y, z) \right) \tag{2.7}$$

Two methods are typically used to quantify the strength of the instability: integration of the disturbance profile across the boundary layer and taking the maximum of the disturbance profile. In this work, the latter method is used following the work of Rius Vidales (2022), the mathematical description is given in Equation 2.8. The disturbance of the first harmonic is used to define this quantity as it is used for comparison with CLST. The growth of the disturbance is quantified analogous to the e^N method. Hence, the amplification rate (or N factor) is calculated according to Equation 2.9 where the subscript 0 denotes the reference amplitude. This reference is the adiabatic value of the most upstream experimental measurement plane.

$$A_I = \max\left(\langle q' \rangle_{z,(0,1)}\right) \tag{2.8}$$

$$N = log\left(A_I / A_{I,0}\right) \tag{2.9}$$

2.3.5 Analysis of Unsteady Disturbances

The analysis of the steady disturbances provides no information on the development of unsteady disturbances (such as the secondary CF instabilities) and their flow structures. Hence, different techniques are applied for the unsteady disturbances.

Power Spectral Density

The first analysis tool for the unsteady disturbance is the evaluation of the power spectral density (PSD, Φ) of the temporal signal at specified spatial positions as these spectra provide information on the dominant frequencies of the different secondary CF instability modes and the energy associated to them.

Welch's method has been applied to estimate the PSD, in this method the time signal is divided into a specified number of segments over which periodograms are calculated, averaging of the periodograms results in the averaged PSD. In this work, Welch's method is performed with a 50% segment overlap where a Bartlett window is applied to segments of size $f_s/10 = 5120$ points such that a 10Hz frequency resolution (f_{res}) is achieved. The obtained PSD is non-dimensionalised with Equation 2.10 following the work of Deyhle and Bippes (1996) and Rius Vidales (2022) with U_∞ being the freestream velocity.

$$\Phi^* = \sqrt{\frac{f_{res}\Phi}{U_\infty^2}} \tag{2.10}$$

Unsteady Disturbance Amplitude

To track the growth and visualise the different unsteady modes the temporal signal needs to be filtered such that only the corresponding frequencies are considered. For this purpose, the Infinite Impulse Response Butterworth filter has been chosen as it is designed to have maximal flatness in the passband region (Şengül, 2018). The filter was chosen to be of 10$^{\text{th}}$ order to ensure a sharp frequency roll-off where the limits are defined such that the specified passband frequencies have a -3dB attenuation in the frequency roll-off. The signal is filtered by applying a zero-phase filtering algorithm.

The RMS (σ_{Q_f}) of the resulting filtered signal is calculated to obtain the strength of the velocity fluctuations of the interested frequencies and is visualised in the zy planes to investigate the topology of the different frequencies. The methodology employed by White and Saric (2005) and Downs and White (2013) is used to quantify and track the growth of the different frequencies in the chordwise direction. In this method, the filtered velocity fluctuations of the zy planes are spatially integrated across both z and y and normalised with the length of the integration domain in y and z yielding the amplitude A_{II} as formulated in Equation 2.11.

$$A_{II} = \frac{1}{\bar{Q}_e}\frac{1}{y^m}\frac{1}{z^m}\int_0^{y^m}\int_0^{z^m} \sigma_{Q_f}\left(y,z\right) dzdy \tag{2.11}$$

2.3.6 Uncertainty Analysis

To validate the experimentally results, it is important to understand their limitations and uncertainties, these are either systematic or random in nature.

For HWA, a systematic error is introduced by the relation between the output voltage and the velocity which is minimised in the calibration procedure. A typical systematic error in adiabatic conditions measurements is a drift of the fluid temperature due to a lack of or insufficient thermal control of wind tunnels. This systematic error is removed by applying the calibration procedure as proposed by Hultmark and Smits (2010) in the current work. However, the presence of the thermal boundary layer requires thermal measurements which, as became clear from subsection 2.3.1, exhibit instrument-related errors. Consequently, an error is introduced in the velocity measurement as a function of the temperature measurement error.

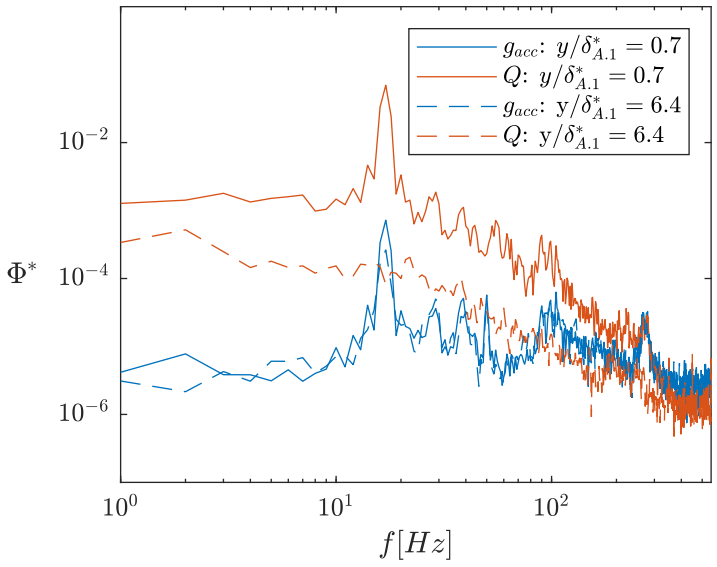

Figure 2.10: Spectra of the velocity signal (Q) and the accelerometer signal (g_{acc}) in the y axis of the STEP for a point close to the wall (—, $y/\delta^*_{A.1} = 0.7$) and in the external flow (- -,$y/\delta^*_{A.1} = 6.4$) at $x/c_x = 0.52$. The spectra are calculated following the methodology presented in subsection 2.3.5 but with Bartlett window size of 51200 points to obtain a frequency resolution of 1 Hz. x axes is cropped to 550 Hz in accordance with the cut-off frequency of the accelerometer.

A systematic error is introduced by the CW in the determination of the wall distance, which is based on analogue measurements of the wall distance of the CW and HW probe using the micro-alignment telescope. Apart from the accuracy of the telescope ($\pm$ 20 µm), this is difficult to quantify and hence no attempt has been made to do so. Another systematic error is possibly present due to a difference between the measured and actual offset of the HW and CW probe causing a shift between the HW and CW field, impacting the perceived velocity. This potential error will be discussed in more detail in chapter 5, however, the impact of this will not be discussed here in further detail as it has not yet been confirmed that this is an error or if it is.

A random error is introduced by fluctuations present in the flow field that are statistically not independent. This type of error is especially important for high-frequency acquisition measurements (such as HWA) where the time in between measurements is smaller as the integral time scale ($\Delta t < T_{int}$).

Statistical Uncertainty

The statistical uncertainty of the mean flow is computed using the following (Sciacchitano & Wieneke, 2016):

$$\varepsilon_{\bar{Q}} = \frac{k\sigma}{\sqrt{N_{eff}}} \quad \text{with} \quad N_{\text{eff}} = \frac{T}{2T_I} \tag{2.12}$$

The effective number of measurements (N_{eff}) represents the statistically independent measurements. To determine N_{eff}, the integral time scale is calculated using Equation 2.13 where ρ_i is the auto-correlation with lag i. The summation of Equation 2.13 is typically performed up to a defined threshold. Typically, the threshold is chosen to occur when $\rho_i(\tau)$ first crosses (Sciacchitano & Wieneke, 2016). However, other options include the minimum of the auto-correlation function and where $\rho_i(\tau)$ first falls below $1/e$ (O'Neill et al., 2004). In this work, the latter threshold is used. Under the assumption of a Gaussian distribution, a confidence interval of 68% is set, therefore, $k = 1$ in Equation 2.12.

$$T_I = \sum_{i=0}^{\infty} \rho_i(\tau) d\tau \tag{2.13}$$

It has been found that the velocity signal exhibits a sinusoidal oscillation with a frequency of 17 Hz. A comparison of the fluctuations in the velocity and accelerometer signal (acceleration in the y axis of the STEP) shows that these are induced by sting vibrations. The spectrum of both is provided in Figure 2.10 for a signal in the external flow ($y/\delta^*_{A.1} = 6.4$) and close to the wall ($y/\delta^*_{A.1} = 0.7$). The 17

x/c_x	0.31	0.41	0.52	0.63	0.74	0.85	0.96
Heating	$+0.17, -0.20$	$+0.40, -0.42$	$+0.40, -0.44$	$+0.96, -1.00$	$+0.83, -0.87$	$+2.99, -3.11$	$+3.05, -3.15$
Adiabatic	$+1.39, -1.37$	$+0.30, -0.21$	$+0.21, -0.26$	$+0.61, -0.60$	$+0.88, -0.93$	$+1.64, -1.60$	$1.73, -1.44$

Table 2.1: Uncertainty of the steady amplitude ($(\varepsilon_{A_I})/A_I$).

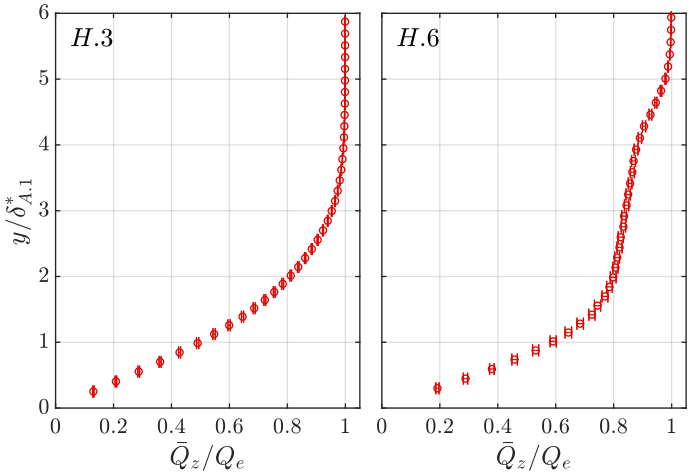

Figure 2.11: Statistical uncertainty of spanwise averaged velocity profile under heating conditions at $x/c_x = 0.52$ and 0.85.

Hz signal is apparent in the spectra at $y/\delta^*_{A.1} = 0.7$ for both the velocity and accelerometer signal. In the external flow, the accelerometer still exhibits the peak at $17\ Hz$, but it is not evident in the velocity signal. This can be explained by the velocity shears in the boundary layer. Outside the boundary layer, the flow is uniform, thus, a vibration does not alter the signal significantly. In the boundary layer, large velocity gradients exist and, as a result, small vibrations can significantly affect the velocity signal.

The presence of this vibration has several implications. First of all, it increases the standard deviation of the velocity signal and, thereby, also the measurement error. Secondly, the effective spatial resolution of the measurements is reduced as the obtained signal is now averaged over the deflection of the sting end. Lastly, the velocity signal is highly correlated with itself because of the sinusoidal behaviour. However, this is not a statistical correlation of the flow pattern but is induced by sting vibrations. To mitigate the effect on the auto-correlation and thus the integral time-scale, it has been chosen to filter the velocity signal with a stopband filter between 15 and $19\ Hz$ before the auto-correlation is calculated. For this, the same methodology of subsection 2.3.5 is followed but instead of a bandpass, a stopband filter is used. The standard deviation of the original signal is used to calculate the statistical uncertainty.

The obtained statistical uncertainty is propagated into the uncertainty of the velocity profile and the steady disturbance profile as these are important parameters in the current work. The result is shown in Figure 2.11 and 2.12 for the measurement planes at $x/c_x = 0.52$ and 0.85 with the heated wall condition.

It is evident from Figure 2.11 and 2.12 that the statistical uncertainty of the velocity and steady disturbance profile is small for plane $H.3$. Therefore, the measurement time of 2 seconds is justified in these conditions. However, for the measurements of plane $H.6$, a higher uncertainty is present, especially in the steady disturbance profile near its maximum and between the two lobes. This maximum is the metric used to assess the development of the vortices, therefore, it is important to understand the uncertainty of this maximum which is given in Table 2.1. Initially, the uncertainty stays below 0.5%, but they increase rapidly downstream of $x/c_x = 0.63$ and the uncertainty of 3% is considerable. Fortunately, this large uncertainty occurs far downstream (which will be shown to undergo nonlinear interactions), and thus, conclusions on the linear development of the vortices are not affected by this uncertainty. One would like to reduce this error, which could be achieved by increasing the measurement time. However, the vibration of the sting is found to be the primary issue and should be addressed if possible.

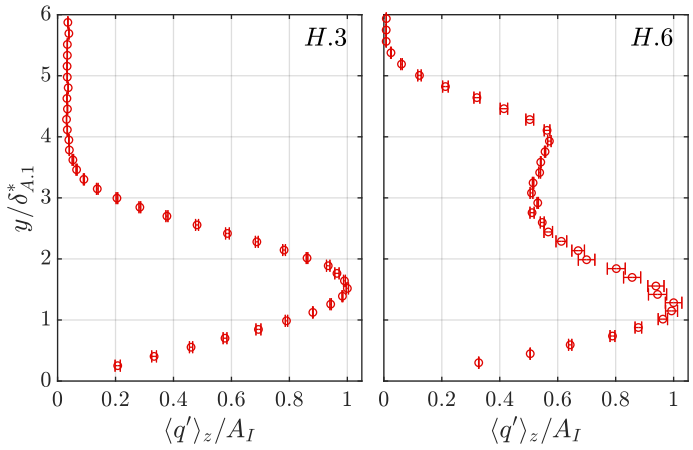

Figure 2.12: Statistical uncertainty of the steady disturbance (no FFT filtering) under heating conditions at $x/c_x = 0.52$ and 0.85.

x/c_x	0.31	0.41	0.52	0.63	0.74	0.85	0.96
$\varepsilon_{A_I,T}/A_I$	0.94%	2.30%	-0.39%	-0.45%	-0.31%	-0.14%	0.36%

Table 2.2: Error of the steady amplitude induced by CWA measurement errors $(\varepsilon_{A_I,T})/A_I$ of the adiabatic wall condition.

Error Induced By Thermal Measurements

Although routines have been developed to treat erroneous behaviour of the CWA circuit, random errors can still be seen in the output temperature. This is evident from Figure 2.8 as the temperature deviates around the ambient temperature of the tunnel. Comparison of the CWA and PT100 measurements show a maximum error of ε_T =2.78 °C. The output temperature is used to calculate the velocity, hence, it is important to understand how this temperature error affects the results. Again, the error is focused towards the steady perturbation profile as this is an important metric used to assess the development of the vortices.

The error is seemingly random and not of a statistical nature, hence, a reference measurement is required to quantify this error. Fortunately, the CWA measurements have also been performed for the adiabatic wall measurement plane while the temperature from the ambient is also available through the PT100. Hence, results where the velocity is obtained with the temperature measurement of the PT100 and CWA can be compared.

The disturbance profile of the primary CF mode for both of these is shown in Figure 2.13 for $x/c_x = 0.52$ and 0.85. A good agreement is found for the profiles, hence, an error in the temperature measurement does not significantly alter the disturbance profile of the primary CF mode. The error regarding steady amplitude A_I is provided in Table 2.2. Overall, the error is found to be below 0.5% except at $x/c_x = 0.31$ and 0.41. The nature of this larger relative error is unknown. However, it has to be noted that the presented error does not necessarily represent the measurement error for the heated wall conditions but rather provides an indication of the error. As the error is generally below 1%, it is not expected to significantly impact the disturbance profiles obtained in the presence of wall heating and its maximum amplitude.

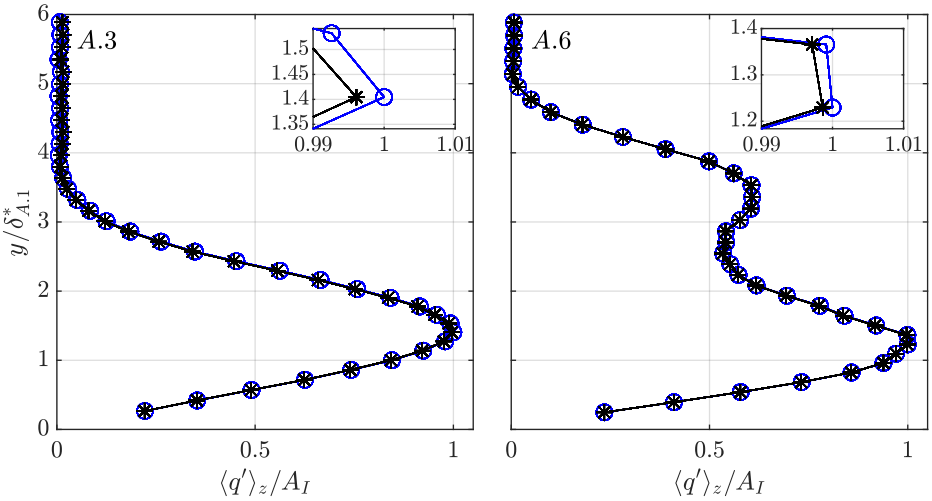

Figure 2.13: Disturbance profiles or primary CF mode obtained when using PT100 (-o-) and CWA (-∗-) as temperature reference for the adiabatic wall conditions. The left represents the disturbance profile at $x/c_x = 0.52$ and the right at $x/c_x = 0.85$.

3

Numerical Methodology

This chapter introduces the utilised numerical framework. First, the Compressible Boundary Layer solver (CBL) is introduced in section 3.1 after which the Compressible Linear Stability Theory (CLST) is discussed in section 3.2. Section 3.3 explains the process used to retrieve the surface temperature distribution required in the numerical framework.

3.1 Compressible Boundary Layer Solver

The boundary layer and its characteristics must be known before stability computations can be performed. In the current work, the thermal boundary layer modifies the density and viscosity across the boundary layer which is not evaluated in incompressible boundary layer theory, hence, CBL computations are required. The methodology of the CBL follows that presented by Liu (2021) with a few modifications. The compressible boundary layer equations are simplified by assuming a steady-state flow over an infinite span flat plate such that the boundary layer's three-dimensionality is retained while it is invariant in the spanwise direction ($\partial/\partial z = 0$). Combined with the usual boundary layer approximations, Equations 3.1 are obtained. Evaluating μ and k as a function of the temperature yields u, v, w, ρ, p and T as unknowns. At the wall, the no-slip, no penetration and constant or adiabatic temperature conditions are applied (see Equation 3.2a). The wall-normal velocity is set to zero in the freestream, and the streamwise velocity, spanwise velocity and temperature are set to approach the external flow conditions yielding Equation 3.2b.

$$\frac{\partial \rho u}{\partial x} + \frac{\partial \rho v}{\partial y} = 0 \tag{3.1a}$$

$$\rho\left(u\frac{\partial u}{\partial x} + v\frac{\partial u}{\partial y}\right) = -\frac{\partial p_e}{\partial x} + \frac{\partial}{\partial y}\left(\mu\frac{\partial u}{\partial y}\right) \tag{3.1b}$$

$$\frac{\partial p}{\partial y} = 0 \tag{3.1c}$$

$$\rho\left(u\frac{\partial w}{\partial x} + v\frac{\partial w}{\partial y}\right) = \frac{\partial}{\partial y}\left(\mu\frac{\partial w}{\partial y}\right) \tag{3.1d}$$

$$\rho c_p\left(u\frac{\partial T}{\partial x} + v\frac{\partial T}{\partial y}\right) = u\frac{\partial p_e}{\partial x} + \frac{\partial}{\partial y}\left(k\frac{\partial T}{\partial y}\right) + \mu\left(\frac{\partial u}{\partial y}\right)^2 + \mu\left(\frac{\partial w}{\partial y}\right)^2 \tag{3.1e}$$

$$p = \rho R T \tag{3.1f}$$

$$y = 0 : u = v = w = 0, \quad T = T_w \quad \text{or} \quad \partial T/\partial y = 0 \tag{3.2a}$$

$$y \to \infty : u \to u_e, \quad v \to v_e, \quad w \to w_e \quad \text{and} \quad T \to T_e \tag{3.2b}$$

Under the assumption of a Falkner-Skan velocity profile, one can perform a Falkner-Skan transformation retrieving a self-similar form of the boundary layer equations. When this transformation is applied

to the set of Equations 3.1 and under assuming low Mach numbers ($M \to 0$) this can be shown to reduce to Equations 3.3. The inflow of the Falkner Skan profile is defined through the Hartree parameter based and the wall temperature or heat flux depending on the experimental conditions.

$$(Nf'')' + ff'' = \frac{2m}{(m+1)}\left(f'^2 - \tau\right) \tag{3.3a}$$

$$(Ng')' + fg' = 0 \tag{3.3b}$$

$$\frac{1}{Pr}(N\tau')' + f\tau' = 0 \tag{3.3c}$$

$$N = \tau^{1/2}\left(\frac{1 + T_s/T_e}{\tau + T_s/T_e}\right) \tag{3.3d}$$

where

$$f(\eta) = \frac{u}{u_e}, \quad g(\eta) = \frac{w}{w_e}, \quad \tau(\eta) = \frac{T}{T_e} \quad \text{and} \quad \eta = y\sqrt{\frac{(m+1)u_e}{2v_e x}} \tag{3.3e}$$

The boundary conditions presented in Equation 3.2 are consequently transformed into Equation 3.4. The grid is discretised by a uniform spacing in x direction and a pseudo-spectral spacing in y using Chebyshev polynomials. The collocation points are clustered in the near-wall region to ensure an accurate computation of the high gradient flow near the wall. A 5$^{\text{th}}$ order Runge-Kutta method is used to solve the system of equations 3.3 where the derivatives in the streamwise direction are obtained through a first-order backward Euler scheme and in the wall-normal direction pseudo-spectral Chebyshev differentiation matrices are used.

$$\eta = 0 : f = f' = g = 0, \quad \tau = \tau_w \quad \text{or} \quad \tau' = 0 \tag{3.4a}$$

$$\eta \to \infty : f' = g = \tau = 1. \tag{3.4b}$$

3.2 Compressible Linear Stability Theory Solver

First the governing equations are obtained, these are the same as the CBL equations hence they are provided in Equation 3.1. Then, the flow is decomposed in its base flow and disturbance components ($q = \bar{q} + q'$ where $q' = [u', v', w', \rho', T']$) and substituted in the governing equations. By subtracting the base flow terms, removing nonlinear terms, assuming parallel flow and substituting the wave-like disturbance ansatz ($q' = \hat{q}(y)e^{i(\alpha x + \beta z - \omega t)}$), Equation 2.12-2.17 of Özgen and Kırcalı (2008) is obtained with the following boundary conditions:

$$y = 0 : \hat{u} = 0, \quad \hat{v} = 0, \quad \hat{w} = 0 \quad \text{and} \quad \hat{T} = 0 \quad \text{or} \quad \partial\hat{T}/\partial y = 0 \tag{3.5a}$$

$$y \to \infty : \hat{u} = 0, \quad \hat{v} = 0, \quad \hat{w} = 0 \quad \text{and} \quad \hat{T} = 0 \tag{3.5b}$$

The disturbances are defined to grow spatially, thus, the frequency is real ($\omega = \omega_r$) while the stream- and spanwise wavenumbers are complex ($\alpha = \alpha_r + \alpha_i$ and $\beta = \beta_r + \beta_i$). The system of equations is then solved for α at each specified streamwise location independently by breaking down the system of equations into $A\phi = \alpha B\phi + \alpha^2 C\phi$ which is generalised into the eigenvalue problem of $A\phi = \lambda B\phi$. Here α is the eigenvalue and ϕ the eigenfunction that includes the $\hat{u}, \hat{v}, \hat{w}, \hat{p}, \hat{T}$ terms.

3.3 Surface Temperature Distribution

Unfortunately, no thermal measurements of the surface temperature have been performed under forced convection conditions hence the surface temperature distribution has to be calculated numerically. However, extrapolation of the temperature profiles (from CWA) towards the wall shows that the temperature distribution is not uniform in the streamwise direction (see chapter 4). Consequently, a methodology was developed where the streamwise surface temperature distribution is computed with COMSOL. The temperature distribution obtained from COMSOL is calibrated to the wall temperature obtained from CWA measurements of zy planes at the streamwise measurement stations.

To do so, the CAD design of the swept flat plate and its material properties are imported into COMSOL and boundary conditions are applied. The heat source of the electrical heating elements is modelled by

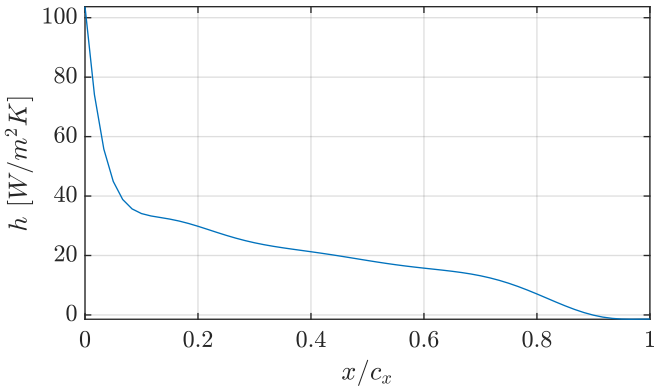

Figure 3.1: Heat transfer coefficient as a function of x/c_x at the midspan of the STEP.

setting a heat flux for the upstream and downstream plates individually. The heat losses of the model are separated into the measurement surface, the back of the plates and the sidewalls. The side walls are set to be adiabatic as heat losses due to radiation, convection and conduction are assumed to be small given the limited heat flux of the heating elements, the large span of the model and the small surface area of the side walls. On the back of the swept flat plate, the boundary layer is assumed to be mostly turbulent. Hence, only convective heat transfer using the approximation of Lienhard (2020) for the heat transfer coefficient except at the areas where the heat flux is specified. The corresponding approximation is presented in Equation 3.6.

$$h_{turb}(x) = \mathrm{Nu}_x \frac{k_{air}}{x} \tag{3.6a}$$

where

$$\mathrm{Nu}_x = 0.0296 \mathrm{Re}_x^{0.8} \mathrm{Pr}^{0.6} \tag{3.6b}$$

Over the measurement surface, the boundary layer is primarily laminar (laminar for $x/c_x \lessapprox 0.86$ in the most extreme condition) and thus the heat loss over the measurement surface is defined by imposing a heat transfer coefficient $h_{lam}(x)$ over the surface. The heat transfer coefficient of laminar boundary layers follows Equation 3.7 thus CBL calculations can be used to estimate $h_{lam}(x)$. Note that the CBL computations have the to-be-determined temperature distribution as an input, and thus, an iterative loop is introduced. In COMSOL, the heat transfer coefficient can be defined as a polynomial, the obtained polynomial is displayed in Figure 3.1.

$$h_{lam}(x) = -\frac{k_{air}}{T_w - T_f} \frac{\partial T}{\partial y}|_w \tag{3.7}$$

With the heat transfer coefficients imposed over the surfaces and the heat sources defined, the COMSOL simulation was run providing the surface temperature as a function of x and z. The streamwise distribution at the midspan was compared to the CWA wall temperature data points, and the heat fluxes were iterated until a good agreement between the CWA and COMSOL temperature distribution was obtained. This process was performed manually and the agreement was inspected visually, hence, a slight improvement can be made by adopting a numerical metric and automation. However, the experimental and numerical boundary layer match very well, as will be shown in chapter 4 and 5, hence this was not deemed necessary and rejected bearing in mind time constraints.

Eventually, a small region of air was added between the up- and downstream plate to function as a barrier for conduction as a discontinuity in the wall temperature is observed at the step location ($x/c_x = 0.397$). This discontinuity became evident from IR thermography measurements of the model under natural convection conditions and agrees well in shape with the CWA measurements. This discontinuity will be discussed in further detail in chapter 4.

4

Preliminary Results

In this chapter, a characterisation of the experimental conditions is provided. First, the streamwise temperature distribution along the midspan is characterised in section 4.1. Secondly, the freestream turbulence is discussed in section 4.2. Then, the step height is characterised in section 4.4 and the impact on the development of the CFI is shortly discussed. The pressure distribution over the model is discussed in section 4.5. Lastly, the conditions of the different measurement planes are specified in section 4.3.

4.1 Wall Temperature

The current work aims to investigate and quantify the effect of the wall temperature on the development of crossflow instabilities and laminar-to-turbulent breakdown. Hence, it is essential to understand the distribution of the wall temperature. As the heating elements do not cover the entire span of the model, inherently, a spanwise variance of the wall temperature exists in the measurement domain. Nevertheless, given the limited extent of the measurement domain ($\Delta Z \approx 0.023 b_Z$ or 21.21 mm), the spanwise variations are considered to be negligible. The wall temperature, as measured/predicted by different methodologies, along the midspan is displayed in Figure 4.1. The white background indicates the extent of the heating elements on the back side of the model (in accordance with the dimensions provided in Figure 2.2).

The dashed line in Figure 4.1 is obtained through IR measurements of the heated plate at equilibrium under natural convection conditions (i.e. $U_\infty = 0$ m/s). During the measurements, the IR camera was calibrated for the anodised aluminium. The polished LE has a different emissivity, yielding erroneous temperature measurements for the LE. Therefore, the LE region is cropped off in Figure 4.1.

The most notable feature of this distribution is the kink in the temperature at the step (vertical dashed line) caused by the model's design. As the model consists of two separate plates, an irregularity in the conductivity is present, causing this kink. In COMSOL, this irregularity is achieved by imposing a thin layer of air between the upstream and downstream plates, acting as a barrier for heat transfer between the plates.

Granting differences in the absolute temperature due to flow conditions (forced vs free convection), the wall temperature obtained through linear extrapolation of the experimental spanwise averaged thermal profile ($\circ$) shows the same overall shape as the IR measurement. Although the overall shape is the same, the experimental data points are based on the zy planes obtained for varying freestream conditions (e.g. changes in ambient temperature). This means that the magnitude of the wall temperature distribution may vary as well between these points. The IR measurements are used to quantify a potential drift in the wall temperature. Considering a small, pre-defined target on the downstream plate, no significant variations IR temperature was observed between the different HWA planes (maximum variation of $\approx 0.6\,^\circ$C). This indicates that the wall temperature is nearly constant between measurement planes (irrespective of the freestream temperature, see section 4.3). Consequently, the temperature distribution is considered to be invariant between measurement planes. This is explained by the heat-

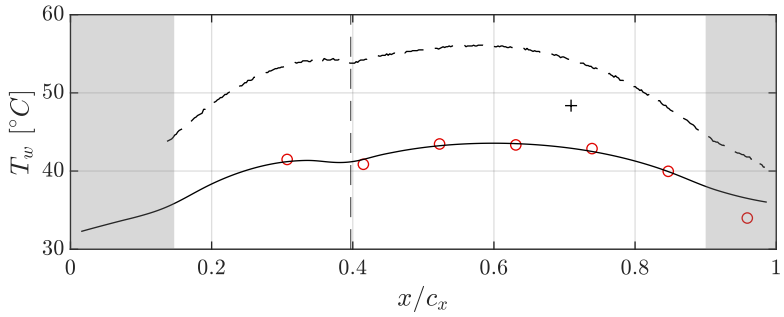

Figure 4.1: Measured and generated surface temperature profile along the midspan as a function of the streamwise station: surface temperature input CLST (——), surface temperature obtained with IR under natural convection conditions (- -), mean surface temperature as obtained with IR during measurements (+), surface temperature obtained through linear extrapolation towards the wall of the temperature profile from the CW measurements (○).

ing elements turning off when the setpoint is reached and turning on when the temperature drops by 2 degrees.

The average of the IR measurements is shown by the symbol + in Figure 4.1. Its value is significantly higher than the wall temperature obtained through the spanwise average thermal profile. The IR images displayed clear reflections of the metallic parts of the pressure body, thereby demonstrating that the perceived temperature of the IR might be affected by reflections of itself or the surroundings. Therefore, the absolute temperature reported by the IR measurement is expected to be offset to the physical temperature. However, this hypothesis requires further elaboration.

After iteration on the heat fluxes in COMSOL (as discussed in chapter 3), the wall temperature distribution (solid line) is obtained. This is used as the boundary condition of the numerical computations. The distribution fits the experimental wall temperature relatively well, validating the overall shape and magnitude of the thermal boundary condition of the numerical framework. The deviation of the last experimental point with the COMSOL wall temperature is explained by local relative wall cooling. This is a consequence of the heating elements not fully extending to the TE and will be further discussed in section 5.2.

4.2 Freestream turbulence intensity

The importance of the freestream turbulence condition upon the determination of the dominance of travelling or stationary crossflow instability modes has been established by Deyhle and Bippes (1996) and White et al. (2001). For low freestream turbulence conditions, the stationary CF modes have been found to dominate and travelling CF modes dominate for high freestream turbulence conditions. Consequently, the freestream turbulence intensity of the tunnel has been measured with and without the STEP model installed. Only the centre point has been measured with the STEP installed due to accessibility considerations.

In Figure 4.2(a), the turbulence intensity is displayed for measurements at the centre of the cross-sectional area of the nozzle for varying freestream velocities. The turbulence intensity is calculated for velocity fluctuations in the frequency range of 2 to $5000\ Hz$ using the bandpass filtering methodology of chapter 2. This frequency range was chosen as it allows for a comparison to the Low Turbulence Tunnel (see Serpieri (2018, section 2.2)) commonly used by the Delft University of Technology for boundary layer stability research (see e.g. Rius Vidales, 2022; Serpieri, 2018; Zoppini, 2023). Evidently, without the STEP model installed, the turbulence intensity remains below 0.06%. The configuration of the wire (i.e. parallel to the minor or major axes of the cross-sectional area of the nozzle) shows slightly different values, indicating a small level of anisotropy in the turbulence. However, the deviation and the absolute values are small and, thus, are not considered problematic. When the STEP model is installed, the turbulence intensity remains low even though it increased slightly for $U_\infty = 10$ and 15 m/s up to $Tu \approx 0.07$%.

Figure 4.2(b) shows the turbulence intensity at different locations along the major axis of the rectangular nozzle outlet at $U_\infty = 15\ m/s$. The turbulence is relatively uniform along the nozzle except at

$Z/b_Z = \pm 0.5$ where it rises to $Tu = 0.21$ and 0.64 %. This is where splitters are located on the STEP model to bleed the turbulent boundary layer away from the measurement region. These peaks are not considered problematic as the splitters bleed away the turbulent flow and the large span of the model decreases the proximity of the higher turbulence away from the measurement region.

Consequently, it is concluded that the tunnel and its combination with the STEP is suitable for investigating the stationary crossflow instability and the induced boundary layer transition.

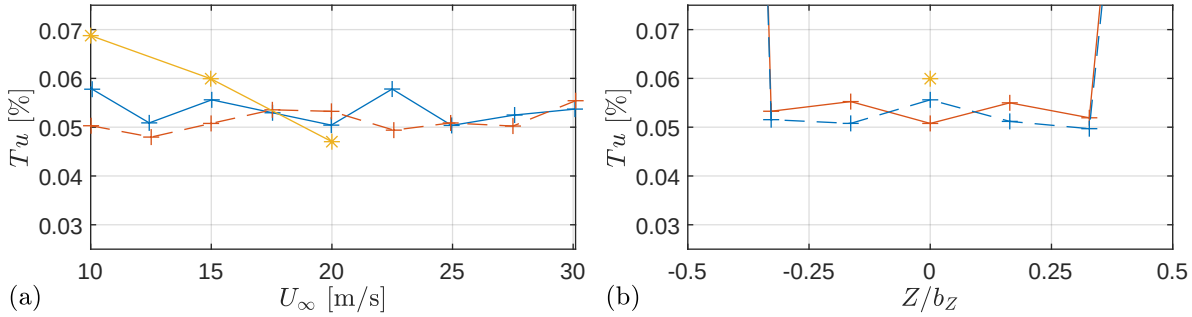

Figure 4.2: Measured turbulence intensity after the signal is filtered through a bandpass with frequencies $f_{bp} = [5, 5000]Hz$. Jet with wire parallel to minor axis (- + -), jet with wire parallel to Major axis (-+-), STEP model installed (-∗-). (a) Turbulence intensity at the intersection of the major and minor axis of the rectangular outlet for varying freestream velocity. (b) Measurements at different stations on the major axis of the rectangular nozzle outlet, where the intersection with the minor axis (centre point) is defined to be $Z/b_Z = 0$ at U_∞ of 15m/s.

4.3 Experimental Measurement Conditions

A total set of 9 different planes are measured for both the adiabatic and heated wall conditions. The plane types, locations and conditions are presented in Table 4.1. The reported temperature ratio is obtained by dividing the mean wall temperature ratio from the numerical distribution, with the average fluid temperature of the measurement plane. In the remaining work, the different planes are denoted by $H.X$ or $A.X$ where A denotes the adiabatic wall conditions and H the heated wall condition. X is substituted by the plane number, specifying the plane type and location.

The fluid temperature and temperature ratio change between measurement planes, in chapter 2 it was mentioned that the A-tunnel facility does not have a thermal management system. Hence, the fluid temperature varies between planes, yielding a variation of the temperature ratio as the thermal condition at the wall is constant across the measurements.

The freestream conditions of measurement plane $H.3$ have been used for the numerical computations. The only difference between the computation of the adiabatic and heated case is that the wall has been set to be adiabatic for the adiabatic wall condition.

Plane Number		1	2	3	4	5	6	7	9	10
Plane Type		YZ	YZ	YZ	YZ	YZ	YZ	YZ	XZ	XZ
x/c_x		0.31	0.41	0.52	0.63	0.74	0.85	0.96	0.85-0.96 $y = 0.7\ mm$	0.85-0.96 $y = 2.3\ mm$
$A.X$	U_∞	15.5	15.7	15.8	15.7	15.7	16	15.9	15.9	16
	Re_c	8.55	8.60	8.56	8.57	8.52	8.57	8.56	8.55	8.54
$H.X$	U_∞	15.5	15.7	15.8	16	16.1	16.1	16	16	16
	Re_c	8.52	8.57	8.55	8.55	8.55	8.55	8.54	8.54	8.54
	T_f	25.24	25.64	26.45	28.92	29.71	29.26	28.57	29.11	29.37
	$(T_w/T_f)_{mean}$	1.05	1.048	1.045	1.037	1.034	1.036	1.038	1.036	1.035

Table 4.1: Specification of conditions at the different experimental measurement planes.

4.4 Characterisation Of The Step Height

In the current research, a challenge of the STEP lies in its original purpose for the investigation of forward- or backwards-facing steps (FFS/BFS) upon transition in three-dimensional boundary layers.

The dual plate design has the disadvantage that a (small) step can form at their junction. Additionally, expansion and contraction of the aluminium plates may affect the step height over a heating cycle. Thus, it is important to characterise the nominal step height and the effect of a heating cycle on its height.

For the measurements, a Micro-Epsilon scanCONTROL 3010-25/BL LASER scanner was attached to the aluminium frame of the test section so that the measurement line was orthogonal to the LE and step. At the end of a measurement day, the measurement of the step height was performed when model was heated. The following morning the step height was measured at the same location for the adiabatic condition. These measurements were performed overnight to ensure that the model was fully cooled down.

Under heating conditions a FFS with a height of $33\,\mu m$ was present at the midspan while a BFS of $6\,\mu m$ was found at the midspan when for the adiabatic wall measurement. The adiabatic wall had a step height variation of $24\,\mu m$ (FFS) to $6\,\mu m$ (BFS) across the span of the measurement region. These values are very small considering the step heights ($591\,\mu m$ and $1292\,\mu m$) quantitatively investigated by Rajendrakumar (2021) on the STEP with a similar pressure gradient while with a higher Reynolds numb (and thus thinner boundary layer). These results are also shortly discussed by Rius Vidales (2022). Consequently, the effect of a heating cycle on the step height is considered to be acceptable and the step heights can be considered to have a negligible impact on the development of the crossflow instability.

4.5 Pressure distribution

The pressure distribution is of great importance to the growth of the stationary crossflow vortices as is mentioned in chapter 1. The pressure distribution across the model is conditioned by the pressure body. The pressure coefficient distribution, as obtained during measurements of the first heated plane ($H.1$), is shown in Figure 4.3(a). No modifications have been made to the pressure body within the experimental campaign. As a result, minimal to negligible variations in the distribution are found across the different measurement planes. Figure 4.3(a) clearly shows a nearly uniform pressure gradient across the model and the small difference between the outboard and inboard measurement suggests the desired spanwise invariance. The spanwise invariance within the measurement region becomes clear from Figure 4.3(b) where the non-dimensionalised external velocity, as measured by the HWA, is shown for planes $A.1$, $A.4$ and $A.7$.

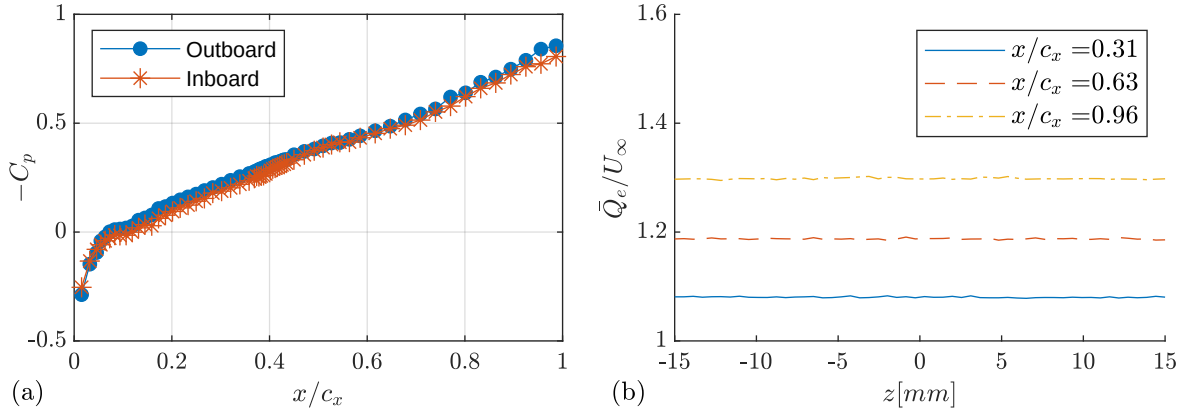

Figure 4.3: (a) Pressure coefficient distribution of plane $H.4$. (b) Non-dimensionalised external velocity measurement $\bar{Q}_e$ normalised with freestream velocity under adiabatic conditions and planes 1,4 and 7 (A.1, A.4, A.7)

5

Results

This chapter will discuss the effect of wall heating on the development of crossflow instabilities based on the numerical and experimental framework. First, the effect of wall heating on the time-averaged velocity boundary layer is discussed in section 5.1. Then the time-averaged thermal boundary layer is dicussed in section 5.2. The effect of wall heating on the steady disturbance is discussed in section 5.3 and the effect on the unsteady disturbances are discussed in section 5.4. Lastly, the effect of wall heating on laminar breakdown is discussed in section 5.5.

5.1 Time-Averaged Velocity Boundary Layer

Figure 5.3 represents the time-averaged velocity field after a spatial FFT-iFFT reconstruction for both the adiabatic and heated wall conditions. Spanwise averaging of this velocity field provides the profiles presented in Figure 5.1, this figure also shows the velocity profiles obtained by CBL. The integral boundary layer parameters based on these velocity profiles are presented in Figure 1.1b. In both Figure 5.1 and 5.3, the velocity is normalised with the external velocity. The y coordinate is non-dimensionalised with the displacement thickness obtained from the HWA measurements of the most upstream plane with the adiabatic surface condition ($\delta^*_{A.1} = 0.618\ mm$). The same reference value has been chosen at all stations to provide a clear indication of the growth of the vortices. The spatial FFT-iFFT reconstruction of Figure 5.3 includes the 1st to 5th harmonics and all wavelengths captured by the measurements larger as the forced wavelength ($\lambda > \lambda_{z,D}$). The contours vary from 0 to 1 with a 0.1 interval.

Close analysis of the experimental velocity profiles in Figure 5.1 shows that wall heating mildly increases the boundary layer thickness for $x/c_x = 0.31 - 0.52$, as is consistent with data presented in Figure 5.2. The increase in the boundary layer thickness is captured relatively well by CBL, however, the effect is more pronounced in the experimental measurements. From $x/c_x = 0.63$ onwards, the experimental data shows a rapid increase in δ_{99} for both wall conditions. Interestingly, the growth of the boundary layer thickness downstream of $x/c_x = 0.63$ is larger in the presence of wall heating.

The increase of the boundary layer coincides with an emerging lobe in the velocity profiles high in the boundary layer. This lobe is associated with a roll-over of low-momentum fluid high in the boundary layer, leading to nonlinear interactions (Reibert et al., 1996). The experimental results suggest that the modulation of the velocity field is larger in the presence of wall heating as the lobe is more pronounced.

The velocity fields in Figure 5.3 show that this is indeed the case. Let's consider the adiabatic surface condition ($A.X$). At the most upstream plane ($A.1$) the modulation of the boundary layer by the stationary CF vortices is still small. When advancing in the streamwise direction, the modulation increases, indicating the growth of the stationary CF vortices. Under adiabatic conditions, the overturning of low-momentum fluid first becomes apparent in plane $A.6$. For the heated wall conditions ($H.X$), a slightly larger modulation of the boundary layer is observed at the most upstream plane ($H.1$) compared to the adiabatic condition. Although no large differences between the adiabatic and heated surface conditions are apparent for the second and third plane ($X.2$ and $X.3$), one can see a slight increase in the maximum y coordinate of the $\bar{Q}/\bar{Q}_e = 0.9$ contour for plane $H.4$ compared to the adiabatic surface measurements. In planes 5 and 6, however, the overturning of low-momentum fluid is

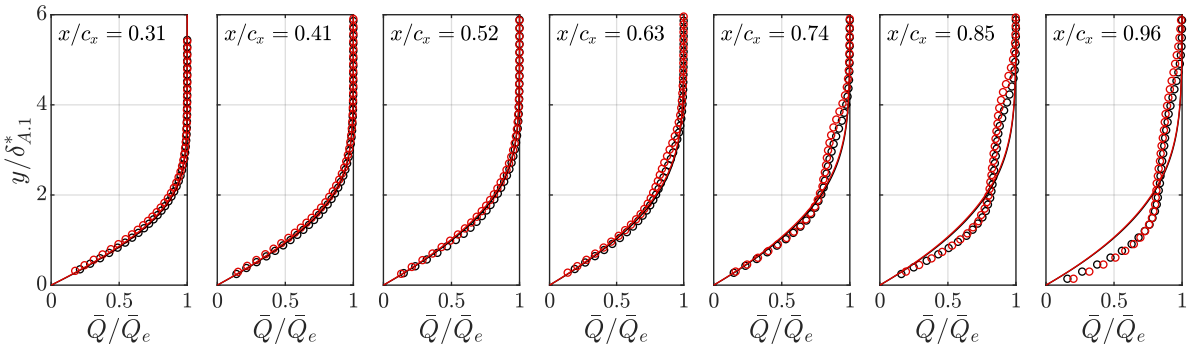

Figure 5.1: Velocity profile of the experimental (○) and numerical (—) results for the adiabatic (black) and heated (red) wall conditions at different streamwise locations.

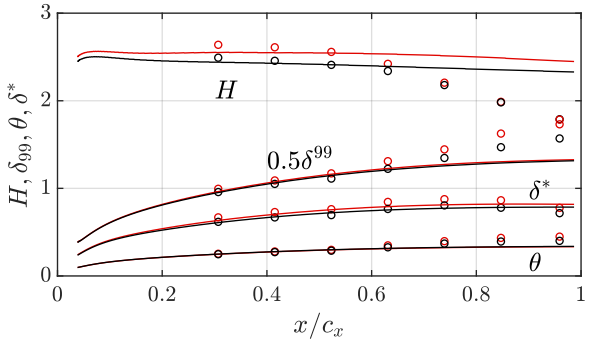

Figure 5.2: Boundary layer integral parameters obtained from the numerical and experimental velocity profiles for the adiabatic (black) and heated (red) wall conditions. δ_{99}, θ and δ^* have the dimension mm, H is dimensionless.

more significant for with wall heating indicating a larger modulation of the mean flow in the presence of wall heating. Consequently, this suggests that the stationary CF vortices are amplified in the presence of wall heating.

The velocity profile distortion is not visible in the numerical computations in Figure 5.1 and the boundary layer thickness is underpredicted by the CBL for these chord locations. This deviation is expected as the CBL computes the baseflow (i.e. the boundary layer without a disturbance) while the experimental profiles in Figure 5.1 represent the spanwise averaged temporally averaged flow of the distorted boundary layer.

The impact of wall heating on the fullness of the boundary layer is an interesting parameter as it has been shown in chapter 1 that it is associated with an increase in the inviscid instability of the crossflow component. The velocity profiles of both the numerical and experimental results show that momentum deficit is increased in the presence of wall heating. The overall agreement between the numerical and experimental results is good for $x/c_x \leq 0.52$, however, the impact of wall heating is less in the numerical framework.

These observations are also evident from δ^* in Figure 5.2 as it increases in the presence of wall heating while this difference is less for the numerical framework for $x/c_x \leq 0.52$. The deviation of the numerical results with the experimental results for $x/c_x \geq 0.63$ is again associated with the mismatch of the represented parameters (base flow versus the mean of the distorted boundary layer). The momentum thickness (θ) is hardly affected by the wall heating, and thus, the H factor increases as a function of the displacement thickness. A mismatch between the CBL and the experimental measurements is again found for $x/c_x \geq 0.63$ because the numerical and experimental results display different parameters.

The trend of the increased momentum deficit in the presence of wall heating is consistent with the analysis of the momentum equations at the wall (Equation 1.9a and 1.9b) in chapter 1 and the work of Ren and Kloker, 2022 who found that wall heating makes the boundary layer less full resulting in an increased displacement thickness (see Figure 1.12).

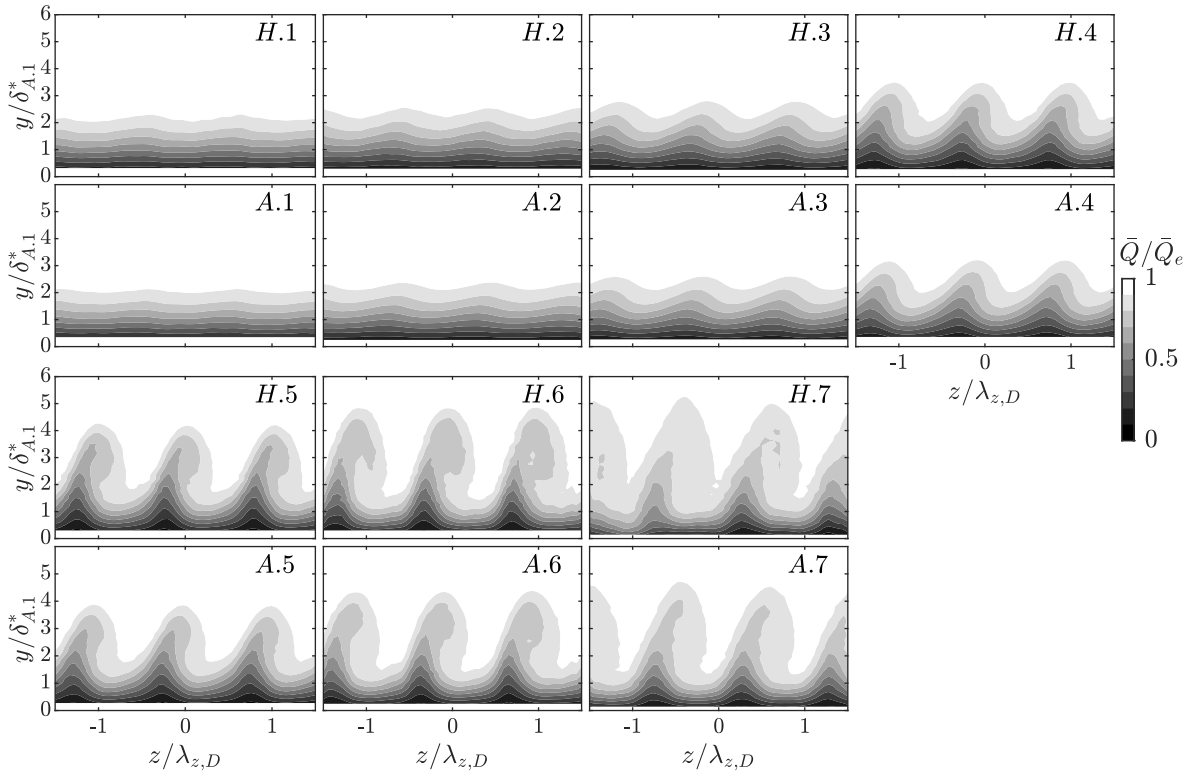

Figure 5.3: Contours of the FFT-iFFT reconstructed time-averaged velocity field from HWA measurements for both the adiabatic ($A.X$) and heated ($H.X$) surface condition at different chordwise locations (represented by X in $A.X$ or $H.X$). Reconstuction includes the 1st to 5th harmonic of the primary CF mode and all wavelengths larger as the forced wavelength ($\lambda > \lambda_{z,D}$). $z = 0$ indicates the midspan of the STEP, positive z the outboard side and negative z the inboard side of the STEP.

A last observation can be made from Figure 5.3. In plane $H.7$, one can observe that the stationary structure is being dissolved, especially for the vortex on the left. White and Saric (2005) explain that this occurs when breaking down. Hence it is found that the laminar breakdown is occurring at $x/c_x = 0.95$ in the presence of the heated wall. In contrast, this is not apparent for the adiabatic wall condition. Hence, these planes suggest that breakdown (followed by turbulent-to-laminar transition) in the presence of wall heating occurs upstream adiabatic conditions, which contrasts the work of Lemarechal et al. (2019) that did not observe a movement of transition in the presence of wall heating. This behaviour will be further discussed in section 5.5

5.2 Time-Averaged Thermal Boundary Layer

The experimental time-averaged thermal field obtained from CWA in the presence of wall heating is shown in Figure 5.5. For the heated wall condition, the experimental and numerical temperature profiles are shown in Figure 5.4. The normalisation of the temperature presented in Equation 1.5 is used.

Firstly, one can see that overall, a good agreement exists between the numerical and experimental results for $x/c_x = 0.31 - 0.52$. Slight differences do exist between the numerical and experimental results, however, this is to be expected given the limitations in the determination of the wall temperature distribution. The good agreement between CBL and the experimental result of the first plane suggests that no significant differences between the experimental and numerical conditions exist upstream of the first measurement plane. Hence, combined with the good agreement of the velocity profiles and the boundary layer integral parameters discussed previously, the CBL is found to represent the experimental conditions well. Thereby it provides a good basis for the stability computations performed with CLST.

The appearance of a lobe in the thermal profile is first evident at $x/c_x = 0.63$, and it continues to grow

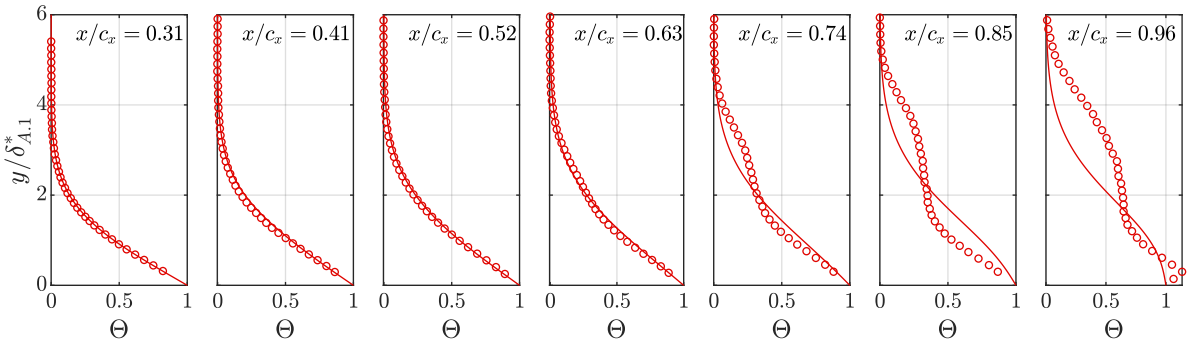

Figure 5.4: Temperature profile of the experimental (○) and numerical (—) results for the heated (red) wall conditions at different streamwise locations.

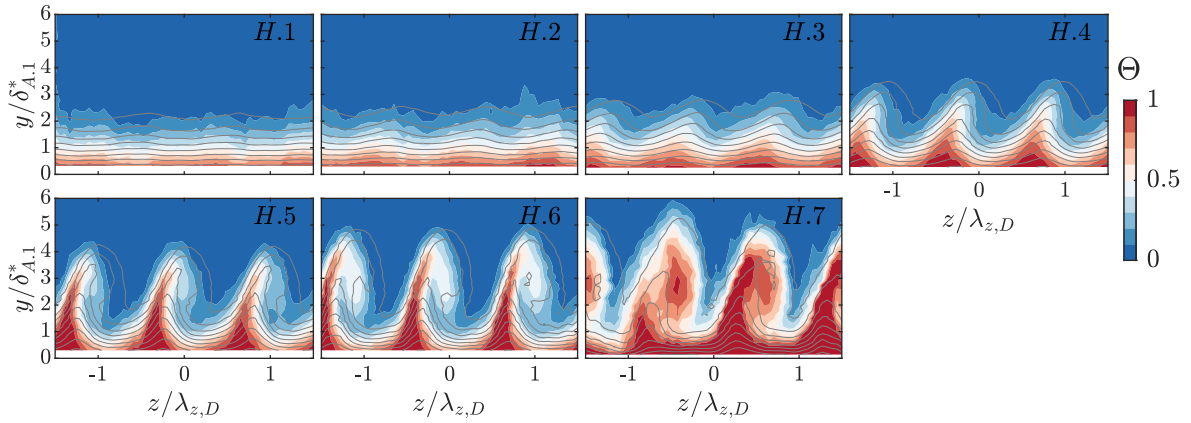

Figure 5.5: Contours of the time-averaged temperature field from CWA measurements for the heated ($H.X$) surface condition at different chordwise locations (represented by X in $H.X$) with the same velocity contours as Figure 5.3. $z = 0$ indicates the midspan of the STEP, positive z the outboard side and negative z the inboard side of the STEP.

when x/c_x increases. Interestingly, a comparison of the velocity profiles in Figure 5.1 and the temperature profiles in Figure 5.4 show that the modulation of the spanwise averaged temperature follows a similar topology to that of the velocity. This is to be expected as the thermal energy is transported by the flow.

The similarity between the velocity and thermal profiles can also be observed when comparing the contours of the non-dimensional velocity and temperature field in Figure 5.5 (velocity isolines are plotted as well for the contours as in Figure 5.3). However, even though the fields exhibit similar topology, they are not identical. A shift in the negative z direction is observed between the velocity and temperate contours, this is especially apparent for the contours in the upwelling region. Whether this shift is physical or introduced by a difference in the measured and actual offset between the HW and CW probe is yet unknown. Under the assumption that this is an artefact of the measurement and the shift is physically not present, an average shift of 1.07 mm is calculated across the different planes through a cross-correlation of the spanwise temperature and velocity distribution at the core height of the primary CF disturbance. As the velocity calculations are a function of the local temperature, this may bias the local velocity and velocity profiles, impacting the disturbance profile. Hence, it is advised to verify this potential shift numerically, especially considering the large thermal spanwise gradients in the later stages of the crossflow development.

An important feature to mention of the temperature profiles in Figure 5.4 is that wall temperature reduces for $x/c_x = 0.74, 0.85$ and 0.96 (based on the wall temperature distribution discussed in section 4.1). This is also evident from the numerical temperature profiles, given the curvature near the wall. One may even expect local wall cooling as the heating elements do not reach up to TE of the model (see section 4.1). However, the non-dimensional temperature profiles remain below one at all stages. Hence, CBL predicts no local wall cooling.

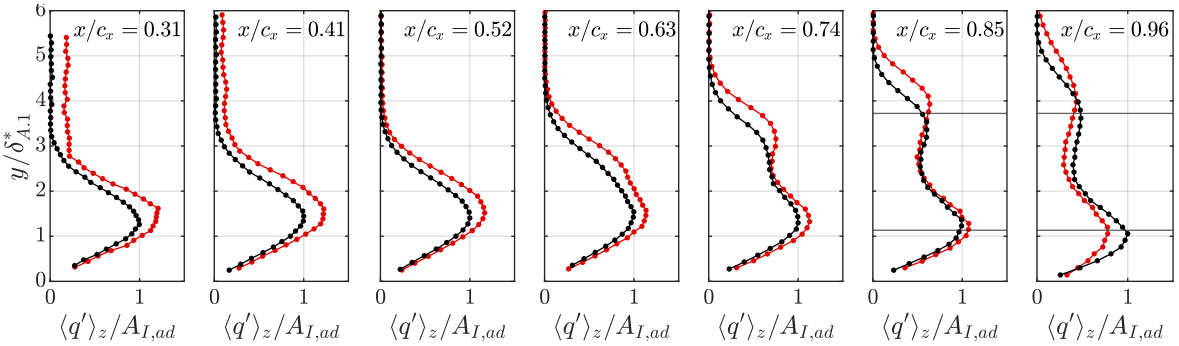

Figure 5.6: Steady disturbance profile of the experimental measurements for the first harmonic obtained through an FFT-iFFT reconstruction. Black represents adiabatic wall conditions, red represents the heated surface conditions. The horizontal lines represent the height of the xz planes discussed in section 5.5.

A close analysis of the experimental profiles at $x/c_x = 0.74$ and 0.85 shows a limited to negligible curvature associated with this local reduction of the wall temperature. This discrepancy is believed to be a combination of the strong modulation of the thermal boundary layer that alters the experimental temperature profile close to the wall, and the lack of measurements in the near-wall region (that potentially would make the curvature more evident).

At $x/c_x = 0.96$, the experimental temperature profile suggests local wall cooling as the measurement point second to the wall is larger than one. Although not directly evident from Figure 5.5, it has been found that the temperature in the upwelling region of the crossflow (the two that exhibit the least breakdown) at the second measurement closest to the wall is larger than the one closest to the wall. In the downwelling region, the temperature remains roughly constant in the downwelling region for the two measurement points closest to the wall. This occurs at two different vortices at the same respective location, suggesting that local wall cooling is occurring rather than being a measurement error. It is unclear why this feature is not present in the CBL simulation but may be related to the large distortion of the thermal boundary layer. Nevertheless, it is not considered to have a significant effect on the results as the boundary layer is either close to breakdown or already breaking down once this feature is encountered.

5.3 Steady Disturbance

5.3.1 Linear Amplification Regime

The N factor of the primary CF mode is shown in Figure 5.7 for both the numerical and experimental results. It is calculated following Equation 2.9 taking the maximum of the disturbance as its amplitude (see Equation 2.8).

A comparison of the adiabatic and heated experimental results shows that the primary CF mode has a larger disturbance amplitude in the presence of wall heating for all measurement planes except $x/c_x = 0.96$. This is also evident from section 5.3 that shows that the maximum magnitude of the steady perturbation is larger in the presence of wall heating for all x/c_x except at $x/c_x = 0.96$. Hence, the experimental results suggest a destabilisation of the primary CF mode. The CLST predictions agree relatively well with the experimental results up until $x/c_x = 0.63$ as the experimental results exhibit nonlinear effects downstream. This will be discussed further in the coming section. The destabilising trend of wall heating is also in agreement with the results of Lekoudis (1980) and Ren and Kloker (2022), who showed a destabilisation of the stationary CF mode using a similar CLST methodology.

A more detailed comparison between the experimental and numerical amplification of the steady mode in Figure 5.7, shows that the amplification of the experimental results for the adiabatic wall condition is larger than predicted by the numerical framework for the planes $x/c_x = 0.41 - 0.63$. The underprediction of CLST increases for increasing x/c_x, suggesting the CLST increasingly underpredicts the growth of the disturbance. This is not related to the wall temperature condition as it already occurs for the adiabatic condition. In fact, this underprediction is a known limitation of local linear stability analysis (such as CLST), which has been shown by Haynes and Reed (1996) and Reibert and Saric (1997) to be attributed to the nature of the local computations that do not take into account the growth of the boundary layer. The growth rate was found to be underpredicted for local linear solvers while

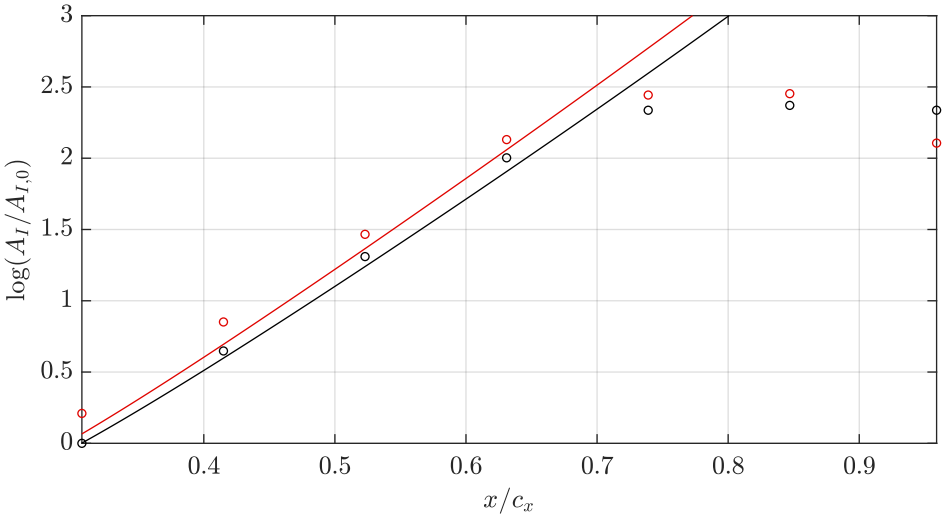

Figure 5.7: Amplification of the experimental (○) and numerical (—) steady disturbance as a function of the chord coordinate. Black represents the adiabatic surface condition, red the heated surface. The reference value $A_{I,0}$ is that of the adiabatic disturbance amplitude of the measurements at $x/c_x = 0.31$, it has a value of $A_{I,0}/\bar{Q}_e = 0.0139$.

a good match with experimental results was found in the initial linear growth stage when nonparallel effects Linear and Nonlinear PSE are taken into account.

In contrast to the adiabatic case, the underprediction decreases in the presence of wall heating as the streamwise coordinate is increased. Consequently, the difference in the N factor between the adiabatic and heated surface conditions decreases. One has to be careful not to interpret this appearance as a function of the streamwise coordinate. As described in chapter 2, the ambient temperature increased during the experimental campaign while the wall temperature remained constant (see section 4.1). This resulted in a decrease of the temperature ratio $(T_w/T_f)_{mean}$ in time, which is translated into a decrease in the temperature ratio as the streamwise coordinate increases from $x/c_x = 0.31$ to 0.63 (the reader is referred to Table 4.1 for more information). Therefore, this is found to be the consequence of a varying temperature ratio of the experimental framework. This conclusion is supported by the CLST predictions that show that the difference between the adiabatic and heated N factor, increases for increasing x/c_x with a constant $(T_w/T_f)_{mean}$.

5.3.2 Nonlinear Interactions And Amplitude Saturation

Initially, the disturbance is found to amplify linearly in both the heated and adiabatic wall conditions. However, the amplification of the experimental result can be seen to deviate from the linear trend at $x/c_x = 0.74$. This behaviour is well understood and is known as amplitude saturation (Haynes & Reed, 1996; White & Saric, 2005) induced by the nonlinear distortion of the boundary layer (Bippes, 1999; Saric et al., 2003). The nonlinear distortion is evident in the experimental steady disturbance profile presented in section 5.3. At $x/c_x = 0.63$, a lobe in the disturbance profile starts to emerge high in the boundary layer which develops further as x/c_x increases for the adiabatic and heated wall condition. This lobe is associated with the nonlinear distortion of the boundary layer by Reibert et al. (1996). An equivalent distortion of the velocity profile is also visible in Figure 5.1 as was discussed in section 5.1.

Interestingly, the distortion is larger in the presence of wall heating as the lobe is more distinct compared to the adiabatic measurements. The implication that this lobe first appears at $x/c_x = 0.63$ and it being more distinct in the presence of wall heating, is that the onset of nonlinear interactions occurs upstream compared to the adiabatic surface condition, the onset of the nonlinear interactions occurs in a similar chordwise position but the growth of nonlinear interactions is higher, or a combination of the two. Given the spacing of the measurement planes, no proof can be provided that the nonlinear interactions start upstream in the presence of wall heating. However, the primary disturbance is found to be amplified by wall heating, and therefore, it is expected that nonlinear effects occur upstream of the adiabatic condition. However, further research is required to confirm.

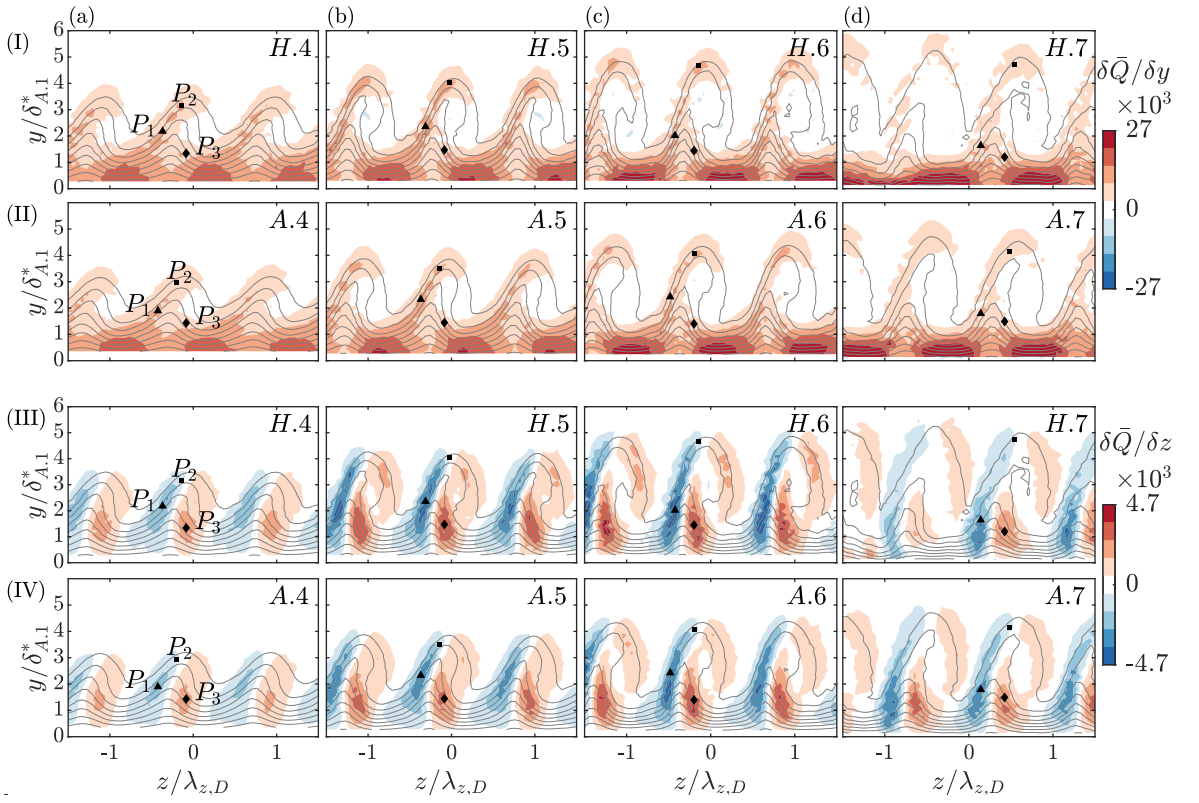

Figure 5.8: The wall-normal (I and II) and spanwise gradients (III and IV) of $\bar{Q}$ for $H.4$-$H.7$ (I.a-d and III.a-d) and $A.4$-$A.7$(II.a-d and IV.a-d)

Following the nonlinear interactions is amplitude saturation. An interesting observation of the effect of wall heating on saturation regards the saturation magnitude. It is observed that the saturation amplitude slightly increases for the heated wall condition compared with the adiabatic condition ($A_I/\bar{Q}_e = 0.1615$ for the heated wall condition versus $A_I/\bar{Q}_e = 0.1487$ for the adiabatic case). However, the measurement uncertainty for this measurement plane (see chapter 2) is in the order of the difference in amplitude between the adiabatic and heated wall conditions. Therefore, further research is required to confirm this.

Another interesting observation concerning amplitude saturation is that it seems to appear upstream in the presence of a heated wall. The growth of the heated wall is found to be $\Delta A_I/\bar{Q}_e = 0.0015$ ($\approx 1\%$ of the amplitude at $x/c_x = 0.85$) between $x/c_x = 0.74$ and $x/c_x = 0.85$ and $\Delta A_I/\bar{Q}_e = 0.0050$ ($\approx 3.36\%$ of the amplitude at $x/c_x = 0.85$) for the adiabatic condition. However, again no definitive conclusions can be drawn as the measurement error at plane $H.6$ is considerable.

A last remark that can be made based on Figure 5.7 regarding the prediction of CLST in the chord region where the experimental results exhibit nonlinear effects. The deviation is expected given as linear stability theory is limited to linear disturbances while the effects found for $x/c_x \geq 0.74$ are strongly nonlinear. This has been shown by Haynes and Reed (2000), who found that linear numerical methodologies (LST, linear PSE) start to deviate from experimental results when the disturbance is developing nonlinearly. Nonlinear PSE, however, does not rely upon the linear disturbance assumption and was found by Haynes and Reed (2000) to agree well with the experimental results.

5.4 Unsteady Disturbances

As discussed in chapter 1, amplitude saturation is followed up by the development of secondary instabilities. To track the development of secondary instabilities, spectral analysis is performed at the location where the type-I to type-III modes are expected to occur, the localisation of the velocity fluctuations for different frequency bands is analysed, and the unsteady disturbance amplitudes are calculated following the methodology presented in subsection 2.3.5.

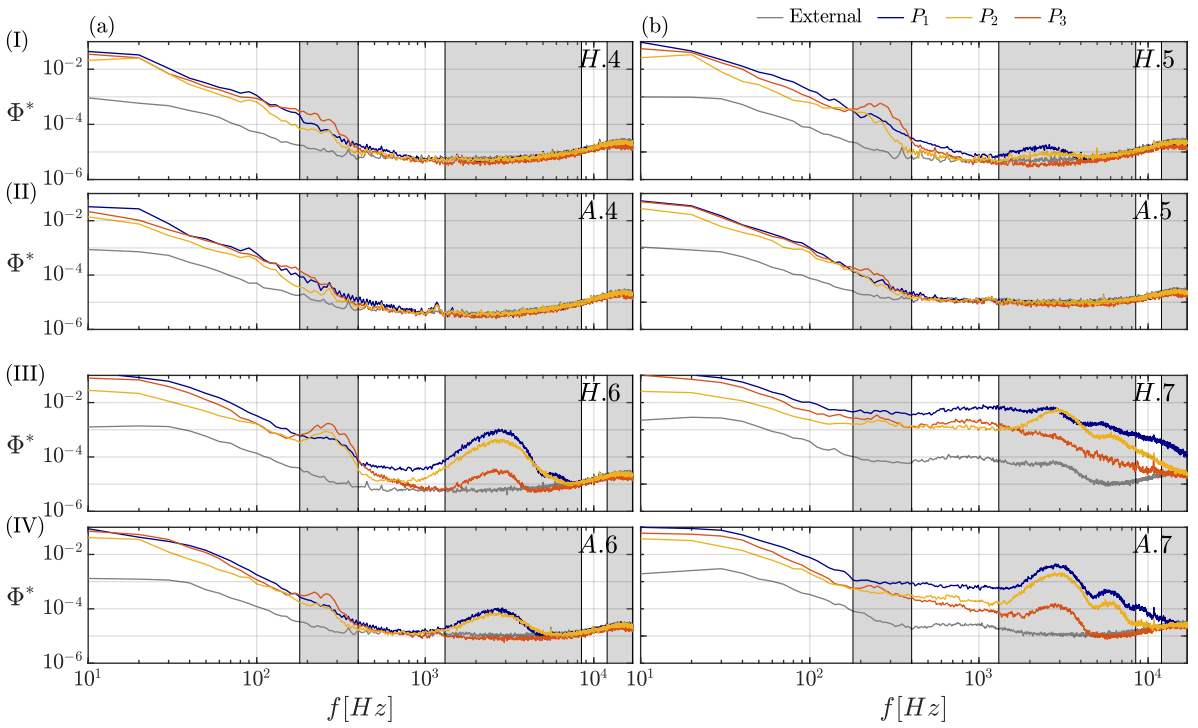

Figure 5.9: Spectra of velocity fluctuations at different spatial locations for plane 4 (I-II.a), 5 (I-II.b), 6 (III-IV.a) and 7 (III-IV.b) under adiabatic (II.a-b, IV.a-b) and heated (I.a-b, III.a-b) surface conditions.

The type-I and type-II modes are Kelvin-Helmoltz instabilities driven by velocity shears in the highly distorted boundary layer (Bonfigli & Kloker, 2007). The type-I mode is driven by the spanwise gradients (White & Saric, 2005) and is typically located in the outer region of the upwelling region where the spanwise gradients are minimum (i.e. negative) (Serpieri, 2018). Utilising the gradients shown in Figure 5.8, spectral analysis is performed at P_1. The type-II mode is conditioned by wall-normal gradients (Malik et al., 1996; White & Saric, 2005) and is typically located on top of the primary vortices (Serpieri & Kotsonis, 2016). This combination has driven the decision to analyse the spectra at point P_2.

In contrast to the type-I and type-II mode, the type-III mode is related to the interaction between stationary and travelling CF modes (Bonfigli and Kloker, 2007; Wasserman and Kloker, 2002) and has lower frequencies as the type-I and type-II mode (White & Saric, 2005). It is manifested on the inner side of the upwelling region and is linked to the local maxima of the spanwise gradient (Wasserman & Kloker, 2002). Hence, one expects the development of this mode at P_3.

The spectra of the analysed points for adiabatic and heated wall conditions are shown in Figure 5.9. The spectrum of the external flow is provided as a reference and obtained at the centre of the domain for the largest wall distance (i.e. in the external flow).

In Figure 5.9, two distinct bands of frequencies can be identified, one at 180-400 Hz and one in the 1310-4860 Hz frequency band. In plane $H.5$ (II.b) and $A.6$ (IV.a), it is apparent that the 180-400 Hz frequency is most pronounced for P_3, which is where the type-III mode is expected to manifest. It is evident from Figure 5.10 that the fluctuations are located in the inner upwelling region where the spanwise gradient is maximum. This observation is consistent with previous research (Serpieri & Kotsonis, 2016; White & Saric, 2005), and hence, it is concluded that the velocity fluctuations in this frequency band are associated with the type-III mode.

The high-frequency 1310-4860 Hz band is most evident for P_1 and P_2 in Figure 5.9. The RMS of these fluctuations is shown in Figure 5.12, showing that the fluctuations are located on the outer side of the upwelling region. This characteristic is consistent with the work of, for example, Bonfigli and Kloker (2007), Serpieri and Kotsonis (2016), and White and Saric (2005) and it was characterised as the type-I mode. Hence, velocity fluctuations in the 1310-4860 Hz frequency band are found to be of the type-I mode.

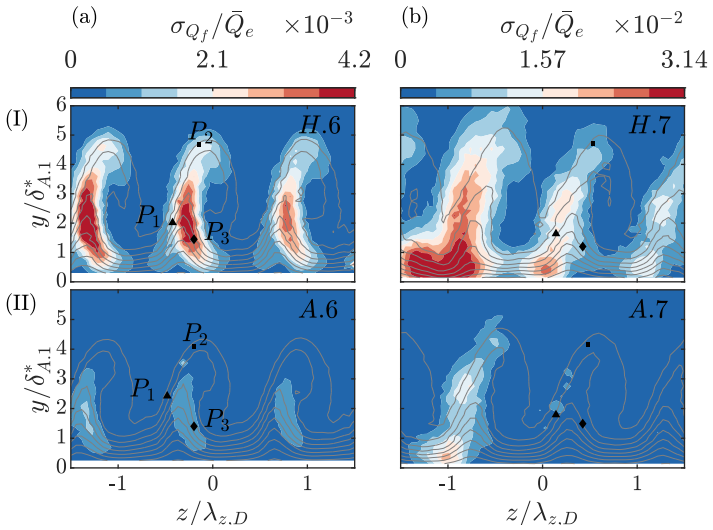

Figure 5.10: RMS of the velocity fluctuations in the $180 - 400\ Hz$ frequency band for measurement plane 6 ($x/c_x = 0.85$, column a) and 7 ($x/c_x = 0.96$, column b) for heated (I) and adiabatic (II) conditions.

The spectra in Figure 5.9 show an additional, higher frequency mode in the 4860-8450 Hz frequency band for plane $H.6$ (III.a) and $A.7$ (IV.b). This frequency is visible for both P_1 and P_2. Although no visualisation is shown in this work of the associated RMS of these fluctuations, they are found to occur in the outer side of the upwelling region similar to the results shown in Figure 5.12. Hence, this frequency band is also believed to be associated with the type-I mode. These frequencies are combined into a 1310-8450 Hz band and when discussing the type-I mode in the remainder of this work, the velocity fluctuations in this frequency band are meant.

No further distinct frequency bands are evident in Figure 5.9, and the readily discussed frequencies do not show that they are primarily manifested on top of the stationary CF vortices, which is expected for the type-II mode based on the work of Malik et al. (1996) and White and Saric (2005). This suggests that no significant type-II mode is present in the current work.

The frequencies of the velocity fluctuations and the localisation remain unaffected by wall heating. Additionally, it will be shown that the breakdown originates from the type-I mode for both wall conditions later. Hence, the topology of the secondary instabilities is not affected by wall heating.

In plane $H.7$ (III.b of Figure 5.9), the spectra have flattened and risen in value over the whole frequency domain indicating that the flow is breaking down. The same happens in $A.7$ (IV.b), however, the magnitudes are lower than $H.7$ (III.b) and the type-I mode is still clearly distinguishable. This indicates that the boundary layer is in an earlier stage of breakdown compared to heated wall condition indicating an advancement of breakdown by surface heating. This is supported by Figure 5.11 where one can see that the turbulent fluctuations (12-17 kHz band) are significantly larger in the presence of wall heating (Figure 5.11(b)).

These turbulent fluctuations originate from the outer side of the upwelling region for both wall conditions, suggesting that breakdown is initiated from the type-I mode for both surface conditions. Thus, the presented results indicate that breakdown is advanced by surface heating but that the topology of breakdown remains unchanged for the current temperature ratios.

5.4.1 Type-I Mode

It is evident from Figure 5.9 that the frequency band associated to the type-I mode is absent in plane 4 for both the adiabatic (II.a) and heated (I.a) surface conditions. This is consistent with the experimental data that shows that saturation of the primary CF disturbance occurs downstream of $x/c_x = 0.63$. Comparison of $H.4$ with $H.5$ in Figure 5.9 (I.a and I.b) shows an apparent rise in the type-I associated frequency band. This rise is not evident for the adiabatic measurement planes at the same x/c_x coordinates and comparison of plane $A.5$ and $H.5$ ($x/c_x = 0.74$) show that the amplitude of the frequencies associated with the type-I mode is larger in amplitude for the type-I mode. Hence, the type-I mode

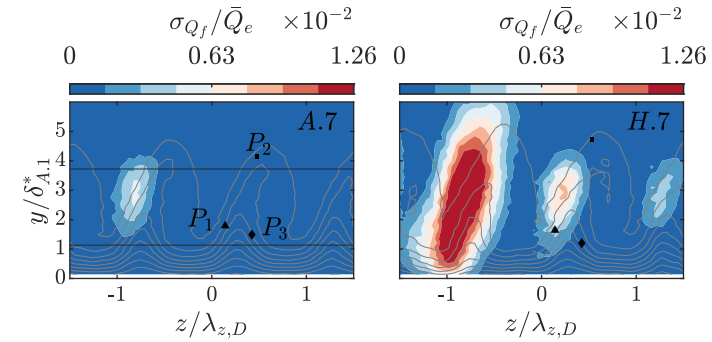

Figure 5.11: RMS of the velocity fluctuations in the $12 - 17\ kHz$ frequency band for measurement plane 7 for adiabatic and heated surface conditions (left and right respectively). The horizontal lines represent the height of the xz planes discussed in section 5.5.

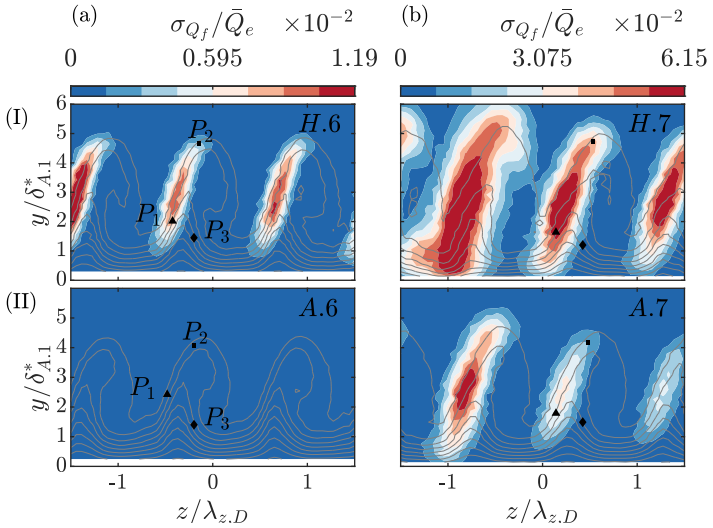

Figure 5.12: RMS of the velocity fluctuations in the $1310 - 4860\ Hz$ frequency band for measurement plane 6 ($x/c_x = 0.85$, column a) and 7 ($x/c_x = 0.96$, column b) for heated (I) and adiabatic (II) conditions.

frequency is found to develop upstream in the presence of wall heating. As the type-I mode is inviscid instability that develops following saturation, this suggests that amplitude saturation occurs upstream in the presence of wall heating as is also suggested by the steady perturbation amplitude.

The observation is not consistent with the growth of the unsteady amplitude shown in Figure 5.14. Here, $A_{II,0}$ is the unsteady amplitude at $x/c_x = 0.31$ of the adiabatic wall condition for each respective frequency band. The amplitude for the heated wall condition is smaller than the amplitude of the adiabatic case for the type-I mode frequencies which contradicts the results of the previous paragraph. This has been found to be a consequence of a lower RMS in the background (affecting the computation of (A_{II}) of this specific measurement plane ($H.5$). Hence, a comparison of the unsteady amplitude of the adiabatic and heated case does not present a meaningful comparison for this particular plane. Therefore, the conclusion that the onset of the type-I mode is moved upstream by wall heating in the previous paragraph still holds.

Further analysis of the results in Figure 5.14 shows that the unsteady amplitude grows quickly after amplitude saturation for both wall conditions. This is consistent with the widely reported growth of the type-I mode in other work (see (Bippes, 1999; White & Saric, 2005)). Furthermore, Figure 5.14 shows that the unsteady amplitude in the presence of wall heating is considerably larger in the presence of wall heating. Therefore, it is found that the type-I mode is considerably destabilised by wall heating.

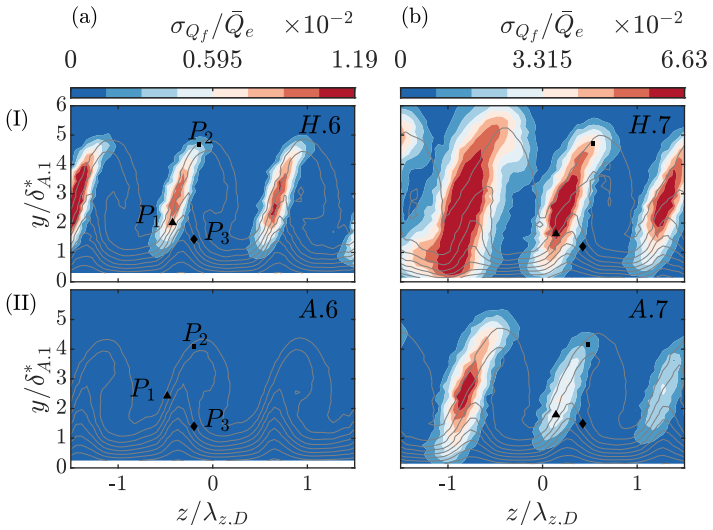

Figure 5.13: RMS of the velocity fluctuations in the $1310 - 8450\ Hz$ frequency band for measurement plane 6 ($x/c_x = 0.85$, column a) and 7 ($x/c_x = 0.96$, column b) for heated (I) and adiabatic (II) conditions.

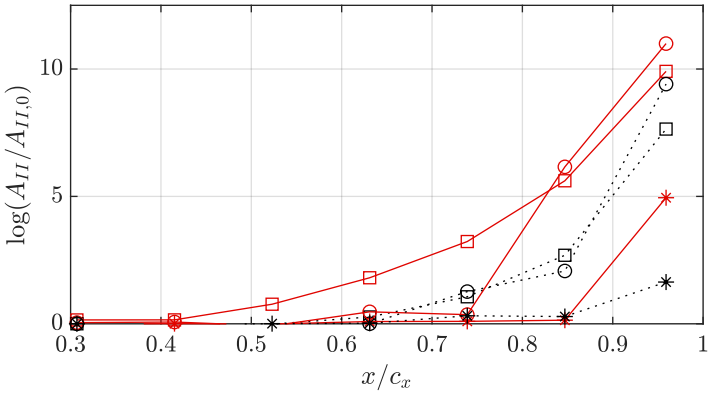

Figure 5.14: Growth of the unsteady amplitude for different frequency ranges for the adiabatic (black, ····) and heated (red, —) wall conditions normalised by the first calculated adiabatic plane. $180 - 400\ Hz$ (□), $1310 - 8450\ Hz$ (○) and $12 - 17\ kHz$ (∗).

5.4.2 Type-III Mode

The effect of wall heating on the type-III mode is apparent from both the spectra and the unsteady amplitude. In Figure 5.9, one can see that the low-frequency band shows a more apparent hump at P_3 in the presence of wall heating for all measurement planes except the most downstream plane (caused by the breakdown). This indicates that the energy content of the velocity fluctuations is higher in the presence of wall heating suggesting a considerable destabilisation of the type-III mode.

The destabilisation of the type-III is even more evident in the unsteady amplitude (see Figure 5.14). Overall, the magnitude of the unsteady amplitude for the frequencies associated with the type-III mode is considerably larger in the presence of wall heating. Additionally, the growth of this mode becomes first apparent at $x/c_x = 0.52$ in the presence of wall heating and at $x/c_x = 0.63$ for the adiabatic case. Hence, it is concluded that the type-III mode is considerably destabilised by the presence of wall heating.

Unlike the type-I mode, the type-III mode is found to develop upstream of saturation. This difference is associated to the nature of the instability. The type-I mode is conditioned by spanwise velocity gradients in the highly distorted boundary layer while the type-III mode has been linked to an interaction between the travelling and stationary CF modes by, for example, Tempelmann, Schrader, et al. (2012) and White and Saric (2005). The latter suggests the destabilisation of the type-III mode by wall heating is a function of a destabilised travelling CF mode. This would be in agreement with the trends found in the research of Eppink and Wlezien (2011) and Ren and Kloker (2022). Eppink and Wlezien

(2011) processed experimental data of previously performed experiments and found that a variation in the wall temperature affected the travelling crossflow modes and confirmed this through PSE computations. Ren and Kloker (2022), on the other hand, established a destabilisation of both the stationary and travelling CF modes with CLST predictions. Although not directly mentioned by Ren and Kloker (2022), the computations show a larger destabilisation of the travelling CF modes than the stationary CF mode. The current work does not provide enough information to understand if the travelling CF mode is destabilised by wall heating, and if so, to which extend compared with the primary CF mode. This is certainly an interesting topic as an increase in the temperature ratio may potentially lead to the travelling CF modes becoming dominant over the stationary CF mode. Such a phenomenon is also observed when the freestream turbulence is increased (Deyhle & Bippes, 1996; White et al., 2001). Such a behaviour would completely change the stability characteristics of the swept wing boundary layer. Therefore, further research is required to understand if this can occur and, if so, for which conditions.

5.5 Effect On Breakdown

In the previous section, it is established that breakdown of the CF vortices is advanced in the presence of wall heating. However, the advancement of breakdown and, consequently, transition is yet to be quantified. Typically, IR thermography is performed to investigate the location of the transition front. However, the current setup is not suitable for this technique due to the high diffusivity of the anodised aluminium as discussed in chapter 2. As an alternative to these measurements, HW and CW measurements are performed parallel to the wall at two different heights: the approximate height of the lower lobe in the shape function and the approximate height of the upper lobe. It has to be noted that the disturbance profiles differ between chordwise stations and the heating and adiabatic surface conditions. Hence, the localisation of the plane relative to the disturbance profile will differ slightly between planes. However, breakdown typically spreads rapidly, therefore, these planes provide an indication of the movement of laminar-to-turbulent transition by surface heating.

The obtained velocity signal is filtered through a bandpass filter with 12 and 17 kHz limits at each measurement point. The RMS of the resulting signal is calculated such that turbulent velocity fluctuations are considered. The 17 kHz upper limit has been set as this was found to be the cut-off frequency of the HWA sensor using a square-wave test. The results are shown in Figure 5.15. All planes are referenced to the same minimum σ_{Q_f} retrieved across all the considered planes. The measurements are performed between $x/c_x = 0.85$ and $x/c_x = 0.96$ for 18 equidistant spaced chordwise stations for the same domain in span as the preceding measurement planes.

In Figure 5.15 a set of turbulent wedges visible, this pattern is similar to the jagged transition front found at the wall with, for example, IR thermography (see e.g. Figure 1.10 in Rius Vidales (2022)). A considerable upstream onset of these turbulent wedges can be seen in the presence of surface heating at both $y = 0.7$ and $y = 2.3\ mm$. Hence, the results clearly indicate an advancement of laminar breakdown by wall heating. To quantify the effect, a criterion has been defined. Only the tip of the turbulent wedge is visible for a single stationary CF vortex in the adiabatic surface measurement at $y = 0.7\ mm$, therefore, it has been chosen to define the tip of this specific vortex as the breakdown location for comparative considerations. This coincides with the contours $log_e\left(\frac{\sigma_{Q_f}}{min(\sigma_{Q_f})}\right) = 0.8$ for $y = 0.7\ mm$ and $log_e\left(\frac{\sigma_{Q_f}}{min(\sigma_{Q_f})}\right) = 1.2$ for $y = 2.3\ mm$, the horizontal lines in Figure 5.15 are drawn in compliance with this criterion.

An advancement from 0.952 to 0.897 (difference of 0.055 x/c_x) is found at $y = 0.7\ mm$. At $y = 2.3\ mm$ and advancement from 0.922 to 0.870 (difference of 0.052 x/c_x) is found. This is equivalent to an advancement of 5.8% and 5.6% respectively, relative to the adiabatic location. In the heated case at $y = 2.3\ mm$, the rise of turbulent fluctuations of two additional vortices is visible, however, these are not present for the adiabatic surface condition measurements. Consequently, the quantification is limited to the bounds of the domain leading to a minimum advancement of approximately $0.045\ x/c_x$. This suggests that the numbers mentioned above reasonably represent the advancement of breakdown across the measurement domain.

The found upstream onset of turbulent wedges contrasts the work of Lemarechal et al. (2019) who did not find an appreciable movement of the transition front for a comparable temperature ratio ($T_w/T_f =$

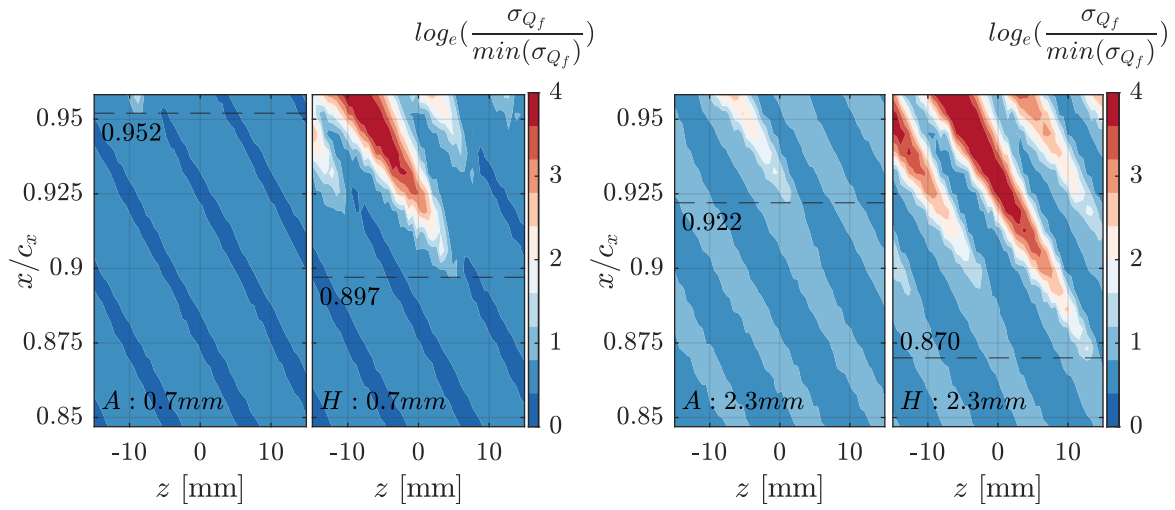

Figure 5.15: Contours of the logarithmic growth of turbulent velocity fluctuations (12 to 17 kHz) referenced to the minimum of all planes. Left set has been performed at $y = 0.7$ mm and right set has been performed at $y = 2.3mm$. A is the adiabatic wall condition and H the heated wall with $(T_w/T_f)_{mean} = 1.036$ at $y = 0.7$ mm and $(T_w/T_f)_{mean} = 1.035$ at $y = 2.3$ mm. To visualise the localisation of these xz planes, horizontal lines are shown in Figure 5.6 and 5.11.

1.04) using the TSP measurement technique. One could argue that a mismatch exists as different metrics are used, Lemarechal et al. (2019) assesses the effect on the transition front at the wall while the results of Figure 5.15 show an increase of the turbulent fluctuations at different wall distances. However, apart from an advancement of the turbulent fluctuations shown in Figure 5.15, the current work also shows an amplification of the primary CF mode, the type-I and type-III mode. Additionally, the time-averaged velocity field presented in Figure 5.3 and the RMS of the turbulent fluctuations shown in Figure 5.11 also indicate that breakdown advances upstream in the presence of wall heating. Therefore, evidence is provided in the current work that strongly suggests a considerable advancement of transition.

Nevertheless, it is an oversimplification to state that transition is advanced by 5.6-5.8%. It is advised to assess the effect on transition using a technique that is directly or indirectly a function of the change in skin friction such as IR thermography. Additionally, one should increase the span of the measurement region in future endeavours when assessing the effect of transition. Currently, only the advancement of a single vortex can be tracked.

6

Conclusions and Recommendations

The effect of wall heating on the stability and breakdown of the laminar swept wing boundary, dominated by stationary CF modes, lacks experimental studies. Therefore, the current work has experimentally investigated the effect of wall heating on the stationary CF mode, using the STEP and the A-Tunnel facility of the Delft University of Technology. Velocity and thermal boundary layer measurements are performed with HWA and CWA, respectively, in the zy plane. The development of the primary CF mode is tracked in the presence of an adiabatic and heated surface using the steady disturbance profile and a comparison to CLST is made. The development of secondary CF instabilities is tracked by integrating the RMS of velocity fluctuations of certain frequency bands in the spanwise and wall-normal direction. The effect on laminar breakdown is assessed by investigating the turbulent velocity fluctuations obtained by HWA and CWA measurements in xz planes (parallel to the wall) at two different wall distances.

In agreement with theory and previous CLST computations (Ren & Kloker, 2022), wall heating has been shown to negatively affect the spanwise averaged boundary layer as the momentum deficit increases in the presence of wall heating. As a result, the displacement thickness increases in the presence of wall heating. The effect on the stability of the boundary layer becomes evident from the zy velocity fields as the distortion of the boundary layer is visibly increased in the presence of wall heating. The destabilisation of the stationary CF mode is confirmed through the steady disturbance profile as its maximum (steady amplitude) is consistently larger in the presence of wall heating prior to breakdown. Comparison of the N factor shows that the destabilising trend observed experimentally is consistent with that of the CLST predictions and with the work of Ren and Kloker (2022) and Lekoudis (1980) that use a similar CLST methodology.

The destabilisation of the stationary CF mode is also observed when evaluating nonlinear effects. The steady disturbance profile and the velocity profile both show the development of a lobe high up in the boundary layer at $x/c_x = 0.63$. This is linked to the nonlinear distortion of the boundary layer by Reibert and Saric (1997). In the presence of wall heating, this lobe is more distinct, indicating that nonlinear development of the vortices occurs upstream in the presence of wall heating.

The experimental results suggest that amplitude saturation of the primary CF mode occurs upstream in the presence of wall heating. However, the measurement error of the steady amplitude is too high to draw a definitive conclusion on this subject. The amplitude at saturation also seems to be affected by wall heating as the experimental results show an increase in the amplitude. Unfortunately, the measurement error is too large, making it premature to draw definitive conclusions. However, spectral analysis shows that the type-I mode, which develops after saturation based on available literature, is present $x/c_x = 0.74$ for the heated wall condition while it is first visible in $x/c_x = 0.85$ for the adiabatic case. This suggests that amplitude saturation occurs indeed upstream.

Besides the amplification of the primary CF mode, wall heating is also found to destabilise the secondary instabilities. Spectral analysis of the velocity fluctuations has identified three distinct frequencies: one low-frequency from 180 to $400\ Hz$, a high-frequency band of $1310-4860\ Hz$ and another high-frequency band from 4860 to $8450\ Hz$. Given its location and frequency, the low-frequency band is identified as

the type-III mode. The $1310 - 4860\ Hz$ is identified as a type-I mode because of its frequency and its localisation on the outer side of the upwelling region. The $4860 - 8450\ Hz$ is identified to occur in the same location as the $1310 - 4860\ Hz$ frequency, hence, it is also associated to the type-I mode. No significant type-II mode has been identified as the mentioned frequencies are not identified at the typical location, nor are considerable velocity fluctuations present for other frequency bands.

A destabilisation of the type-I and type-III modes is observed for the wall heating condition. The type-I mode is found to grow quickly after amplitude saturation, which is consistent with the widely reported behaviour of this mode. A comparison of the spectra shows that the first sign of the type-I mode is evident upstream in the presence of wall heating. Furthermore, the magnitude of the unsteady amplitude is considerably larger in the presence of wall heating for a given x/c_x. This is a clear indication that type-I mode is found to be destabilised by wall heating.

The unsteady amplitude shows that the type-III mode is significantly destabilised by wall heating as the magnitude is considerably larger for the measurements with the heated wall condition. Furthermore, the type-III mode is found to start developing upstream of the adiabatic case. Previous work has linked the type-III mode to an interaction of the travelling and stationary CF modes, see for example Tempelmann, Schrader, et al. (2012) and White and Saric (2005). Therefore, the destabilisation of the type-III mode suggests a destabilisation of the travelling CF mode. This would be consistent with the work of Ren and Kloker (2022) that numerically shows a destabilisation of the travelling CF mode and the work of Eppink and Wlezien (2011) who found a stabilisation of the travelling CF mode experimentally and using PSE computations for a decreasing wall temperature. However, the current work cannot confirm the destabilisation of the travelling CF mode.

The experimental results suggest an advancement of laminar breakdown by wall heating. The first indication of this effect is provided in the time-averaged velocity field where the stationary structure of one of the vortices in the most downstream measurement plane is being dissolved in the presence of wall heating. The adiabatic case does not show such a characteristic. Additionally, a comparison of the RMS distribution in the zy plane shows that the energy content of turbulent velocity fluctuations ($12-17\ kHz$) is much higher in the presence of wall heating for at $x/c_x = 0.95$ plane. The overall result contrasts with the work of Lemarechal et al. (2019) who did observe an appreciable movement of the transition front using TSP.

Quantification of the advancement of breakdown is assessed through the visualisation of turbulent velocity fluctuations in a plane parallel to the wall at two different wall distances. These planes show turbulent wedges that look similar to the jagged transition front obtained by, for example, IR thermography. The onset of these turbulent wedges is observed considerably further upstream in the presence of wall heating, again indicating an advancement of laminar breakdown. Tracking the tip of the most upstream wedge shows an advancement of 5.6% and 5.8% at x/c_x at $y = 0.7\ mm$ and $2.3\ mm$ respectively. This is significant considering that a limited temperature ratio of 1.036 was achieved when performing these measurements. Although this is a strong sign of transition advancement, one cannot characterise the 5.8% as transition advancement as the metric used does not track the transition front at the wall but the onset of turbulent fluctuations.

In short, wall heating has been found to destabilise crossflow instability on multiple fronts. Firstly, the primary CF mode is amplified by wall heating and nonlinear distortion of the boundary layer occurs upstream compared to the adiabatic case. Amplitude saturation also appears to be affected by the wall condition, however, based on the current work no definitive conclusions can be drawn. Both the type-I and type-III secondary instabilities are amplified and laminar breakdown is found to be advanced in the order of 5.7% given a temperature ratio of 1.035.

6.1 Recommendations

In this MSc project, the experiments show that stationary crossflow dominated breakdown is advanced by wall heating, suggesting an advancement of transition. However, quantification of the advancement of the transition front is still missing and should be performed. An ideal scenario would be to observe the transition front using IR thermography or TSP. It is desirable to do so for a uniform wall temperature. Such a quantification is paramount to assess the effect of wall heating on total aircraft drag.

Detailed numerical work is missing to support the results presented in this project. The work of

Lekoudis (1980) and Ren and Kloker (2022) confirm the effect of wall heating on the primary CF mode using CLST, however, no numerical studies are available that investigate the effect of non-adiabatic walls on the nonlinear growth of the primary CF mode and subsequently amplitude saturation. Furthermore, no numerical studies are available investigating the effect of wall heating on the secondary instability. Therefore, it is highly advised to numerically study the effect of wall heating on stationary CF instabilities using a methodology suitable for nonlinear effects. A compressible form of the nonlinear PSE would likely be suitable based on the agreement between PSE and experimental results found in previous studies for adiabatic walls. The work of Malik and Li (1993) and Malik et al. (1994) are good examples of this.

Furthermore, the results suggest a strong destabilisation of the travelling CF mode by wall heating through the destabilisation of the type-III mode. This is complemented by the work of Eppink and Wlezien (2011) and Ren and Kloker (2022). If the effect of wall heating is larger on the growth rate of the travelling mode, then the travelling CF mode may become dominant, changing the stability characteristics of the boundary layer. Therefore, it is important to investigate if this can occur and, if so, for which conditions. This characterisation is best done numerically as it is difficult to assess the effect on the isolated travelling and stationary CF modes in an experimental framework. Additionally, the dominance of the mode is known to be dependent on the freestream turbulence, and thus, it is likely that the effect of wall heating may differ between freestream turbulence conditions. Hence, a full characterisation of the effect will require a change in freestream turbulence, which may not be readily possible depending on the facility. Consequently, a characterisation is most efficient to be performed numerically. A suitable framework is provided by Malik and Li (1993). Using nonlinear PSE, they investigated the interaction of travelling and stationary CF modes for varying initial amplitudes and showed that linear methodologies are unsuitable for this. Hence, a compressible form of the nonlinear PSE methodology can be used to assess the effect of wall heating on the dominance and interaction of travelling and stationary CF modes for different freestream conditions. A first characterisation of the effect of wall heating on the local growth rates can be performed using CLST, however, considering the results of Ren and Kloker (2022) and Eppink and Wlezien (2011) it is already expected that the local growth rate is affected more by the wall condition for travelling CF modes.

The results of the current project suggest an advancement of transition and, thus, skin friction in the presence of wall heating. Consequently, it shows a disadvantageous effect for aircraft technology that needs to dissipate large quantities of heat. However, the effect of wall cooling is believed to be stabilising given the viscosity dependence. Hence, it may be an opportunity for aircraft technology that can implement wall cooling. An example of this is hydrogen combustion, which requires liquid hydrogen to be transformed into its gaseous state (Rondinelli et al., 2017). Therefore, the work should be extended to implement the effect of wall cooling.

Further recommendations can be formulated regarding the current experimental setup. In the current work, sting vibrations have been found to contribute to considerable measurement errors. This has compromised the ability to draw conclusions about amplitude saturation. It is highly advised to address these vibrations if possible.

Secondly, the CWA system was found to exhibit erroneous behaviour. Although this issue has been addressed during post-processing to limit the effect on the results, it is desirable to troubleshoot the system further to allow for more reliable measurements.

Lastly, the temperature ratio was found to vary considerably in the current work due to varying freestream conditions. Given the time requirements of HWA and CWA, freestream conditions vary during and between planes. In an ideal condition, these remain constant. To keep the ambient temperature constant for the full measurement campaign, one would need to install a heat exchanger in the facility. However, considering the implied cost, this may not be feasible. Therefore, it is advised to use measurement techniques that can retrieve data of different planes or heating ratios in a short period of time (such as PIV or IR thermography) when possible.

References

Abid, R., & Masad, J. (1996). Effect of localized cooling on laminar flow. *International Journal of Engineering Science*, *34*(14), 1573–1583. https://doi.org/10.1016/S0020-7225(96)00033-X

Airbus. (2023). At airbus, hydrogen power gathers pace [Accessed on 19-11-2023]. https://www.airbus.com/en/newsroom/stories/2023-06-at-airbus-hydrogen-power-gathers-pace

Barth, H., & Hein, S. (2022). Experimental investigation of spanwise-periodic surface heating for control of crossflow-dominated laminar-turbulent transition. *IUTAM Laminar-Turbulent Transition*, 267–278.

Bergman, T., Lavine, A., Incropera, F., & DeWitt, D. (2011). *Fundamentals of heat and mass transfer* (Seventh Edition). John Wiley & Sons.

Bippes, H. (1999). Basic experiments on transition in three-dimensional boundary layers dominated by crossflow instability. *Progress in aerospace sciences*, *35*(4), 363–412. https://doi.org/10.1016/S0376-0421(99)00002-0

Bodonyi, R., & Duck, P. (1992). Boundary layer receptivity due to a wall suction and control of Tollmien–Schlichting waves. *Physics of Fluids A: Fluid Dynamics*, *4*(6), 1206–1214. https://doi.org/10.1063/1.858239

Boiko, A., Grek, G., Dovgal, A., & Kozlov, V. (2002). *The origin of turbulence in near-wall flows* (1st ed.). Springer Berlin, Heidelberg. https://doi.org/10.1007/978-3-662-04765-1

Bonfigli, G., & Kloker, M. (2007). Secondary instability of crossflow vortices: Validation of the stability theory by direct numerical simulation. *Journal of Fluid Mechanics*, *583*, 229–272. https://doi.org/10.1017/S0022112007006179

Casacuberta, J., Hickel, S., & Kotsonis, M. (2023). Passive stabilization of crossflow instabilities by a reverse lift-up effect. *arXiv*. https://doi.org/10.48550/arXiv.2310.03189

Costantini, M., Fey, U., Henne, U., & Klein, C. (2015). Nonadiabatic surface effects on transition measurements using temperature-sensitive paints. *AIAA Journal*, *53*(5), 1172–1187. https://doi.org/10.2514/1.J053155

Costantini, M., Hein, S., Henne, U., Klein, C., Koch, S., Schojda, L., Ondrus, V., & Schröder, W. (2016). Pressure gradient and nonadiabatic surface effects on boundary layer transition. *AIAA Journal*, *54*(11), 3465–3480. https://doi.org/10.2514/1.J054583

Costantini, M., Risius, S., & Klein, C. (2020). Surface temperature effects on boundary-layer transition at various subsonic mach numbers and streamwise pressure gradients. *New Results in Numerical and Experimental Fluid Mechanics XII: Contributions to the 21st STAB/DGLR Symposium, Darmstadt, Germany, 2018*, 155–164.

Coutinho, M., Afonso, F., Souza, A., Bento, D., Gandolfi, R., Barbosa, F., Lau, F., & Suleman, A. (2023). A study on thermal management systems for hybrid–electric aircraft. *Aerospace*, *10*(9), 745. https://doi.org/10.3390/aerospace10090745

Cukurel, B., Acarer, S., & Arts, T. (2012). A novel perspective to high-speed cross-hot-wire calibration methodology. *Experiments in Fluids*, *53*, 1073–1085. https://doi.org/10.1007/s00348-012-1344-y

Dagenhart, J., & Saric, W. (1999). Crossflow stability and transition experiments in swept-wing flow.

Deyhle, H., & Bippes, H. (1996). Disturbance growth in an unstable three-dimensional boundary layer and its dependence on environmental conditions. *Journal of Fluid Mechanics*, *316*, 73–113. https://doi.org/10.1017/S0022112096000456

Dörr, P., & Kloker, M. (2015). Stabilisation of a three-dimensional boundary layer by base-flow manipulation using plasma actuators. *Journal of Physics D: Applied Physics*, *48*(28), 285205. https://doi.org/10.1088/0022-3727/48/28/285205

Dovgal, A., Levchenko, V., & Timofeev, V. (1990). Boundary layer control by a local heating of the wall. In D. Arnal & R. Michel (Eds.), *Laminar-turbulent transition* (pp. 113–121). Springer Berlin Heidelberg.

Downs, R., & White, E. (2013). Free-stream turbulence and the development of cross-flow disturbances. *Journal of Fluid Mechanics*, *735*, 347–380. https://doi.org/10.1017/jfm.2013.484

Epanechnikov, V. A. (1969). Non-parametric estimation of a multivariate probability density. *Theory of Probability & Its Applications*, *14*(1), 153–158. https://doi.org/10.1137/1114019

Eppink, J., & Wlezien, R. (2011). Data analysis for the nasa/boeing hybrid laminar flow control crossflow experiment. In *41st aiaa fluid dynamics conference and exhibit*. https://doi.org/10.2514/6.2011-3879

Fey, U., Egami, Y., & Engler, R. (2012). High reynolds number transition detection by means of temperature sensitive paint. In *44th aiaa aerospace sciences meeting and exhibit*. https://doi.org/10.2514/6.2006-514

Fey, U., Engler, R., Egami, Y., Iijima, Y., Asai, K., Jansen, U., & Quest, J. (2003). Transition detection by temperature sensitive paint at cryogenic temperatures in the european transonic wind tunnel. *20th International Congress on Instrumentation in Aerospace Simulation Facilities, 2003. ICIASF '03.*, 77–88. https://doi.org/10.1109/ICIASF.2003.1274855

Frick, C., & McCullough, G. (1942). *Tests of a heated low-drag airfoil* (tech. rep.). National Advisory Committee for Aeronautics.

Friederich, T., & Kloker, M. (2012a). Control of the secondary cross-flow instability using localized suction. *Journal of Fluid Mechanics*, *706*, 470–495. https://doi.org/10.1017/jfm.2012.269

Friederich, T., & Kloker, M. (2012b). Localized blowing and suction for direct control of the crossflow secondary instability. In *38th fluid dynamics conference and exhibit*. https://doi.org/10.2514/6.2008-4394

Haynes, T., & Reed, H. (1996, January). Computations in nonlinear saturation of stationary crossflow vortices in a swept-wing boundary layer. In *34th aerospace sciences meeting and exhibit*. https://doi.org/10.2514/6.1996-182

Haynes, T., & Reed, H. (2000). Simulation of swept-wing vortices using nonlinear parabolized stability equations. *Journal of Fluid Mechanics*, *405*, 325–349. https://doi.org/10.1017/S0022112099007260

Hosseini, S., Tempelmann, D., Hanifi, A., & Henningson, D. (2013). Stabilization of a swept-wing boundary layer by distributed roughness elements. *Journal of Fluid Mechanics*, *718*, R1. https://doi.org/10.1017/jfm.2013.33

Hultmark, M., & Smits, A. (2010). Temperature corrections for constant temperature and constant current hot-wire anemometers. *Measurement Science and Technology*, *21*, 105404. https://doi.org/10.1088/0957-0233/21/10/105404

Ivanov, A., & Mischenko, D. (2019). Delay of laminar-turbulent transition on swept-wing with help of sweeping surface relief. *AIP Conference Proceedings*, *2125*(1).

Jørgensen, F. (1971). *Directional sensitivity of wire and fibre-film probes* (tech. rep.). DISA Info.

Joslin, R. (1998). Aircraft laminar flow control. *Annual Review of Fluid Mechanics*, *30*(1), 1–29. https://doi.org/10.1146/annurev.fluid.30.1.1

Kachanov, I., Kozlov, V., & Levchenko, V. (1978). Occurrence of tollmien-schlichting waves in the boundary layer under the effect of external perturbations. *Akademiia Nauk SSSR Izvestiia Mekhanika Zhidkosti i Gaza*, *13*, 85–94.

Koch, W., Bertolotti, F., Stolte, A., & Hein, S. (2000). Nonlinear equilibrium solutions in a three-dimensional boundary layer and their secondary instability. *Journal of Fluid Mechanics*, *406*, 131–174. https://doi.org/10.1017/S0022112099007387

Kosorygin, V., Levchenko, V., & Polyakov, N. (1988). Preprint itam sb as ussr. In M. Y. Hussaini, A. Kumar, & C. L. Streett (Eds.).

Leehey, P., & Shapiro, P. (1980). Leading edge effect in laminar boundary layer excitation by sound. *Laminar-turbulent transition*, 321–331.

Lekoudis, S. (1980). Stability of the boundary layer on a swept wing with wall cooling spyridon. *AIAA Journal*, *18*(9), 1029–1035. https://doi.org/10.2514/3.50852

Lemarechal, J., Costantini, M., Klein, C., Kloker, M., Würz, W., Kurz, H., Streit, T., & Schaber, S. (2019). Investigation of stationary-crossflow-instability induced transition with the temperature-sensitive paint method. *Experimental Thermal and Fluid Science*, *109*, 109848. https://doi.org/10.1016/j.expthermflusci.2019.109848

Li, Y., & Gaster, M. (2006). Active control of boundary-layer instabilities. *Journal of Fluid Mechanics*, *550*, 185–205. https://doi.org/10.1017/S0022112005008219

Lienhard, V., John H. (2020). Heat Transfer in Flat-Plate Boundary Layers: A Correlation for Laminar, Transitional, and Turbulent Flow. *Journal of Heat Transfer*, *142*(6). https://doi.org/10.1115/1.4046795

Liepmann, H., & Fila, G. (1947). *Investigations of effects of surface temperature and single roughness elements on boundary-layer transition* (tech. rep. No. 890). National Advisory Committee for Aeronautics.

Liepmann, H., & Nosenchuck, D. (1982). Active control of laminar-turbulent transition. *Journal of Fluid Mechanics*, *118*, 201–204. https://doi.org/10.1017/S0022112082001037

Liu, Z. (2021). Compressible Falkner–Skan–Cooke boundary layer on a flat plate. *Physics of Fluids*, *33*(12), 126109. https://doi.org/10.1063/5.0075233

Mack, L. (1980). On the stabilization of three-dimensional boundary layers by suction and cooling. *Laminar-Turbulent Transition: Symposium Stuttgart*, 222.

Malik, M., & Li, F. (1993). Transition studies for swept wing flows using pse. *31st Aerospace Sciences Meeting*, 77. https://doi.org/10.2514/6.1993-77

Malik, M., Li, F., & Chang, C. (1994). Crossflow disturbances in three-dimensional boundary layers: Nonlinear development, wave interaction and secondary instability. *Journal of Fluid Mechanics*, *268*, 1–36. https://doi.org/10.1017/S0022112094001242

Malik, M., Li, F., & Chang, C. (1996). Nonlinear crossflow disturbances and secondary instabilities in swept-wing boundary layers. In P. W. Duck & P. Hall (Eds.), *Iutam symposium on nonlinear instability and transition in three-dimensional boundary layers* (pp. 257–266). Springer Netherlands.

Manuilovich, S., & Ustinov, M. (2014). Heat addition effect on the instability of the crossflow in a three-dimensional boundary layer. *Fluid Dynamics*, *49*, 602–607. https://doi.org/10.1134/S0015462814050068

Marec, J. (200). Drag reduction: A major task for research. *CEAS/DragNet European Drag Reduction Conference*.

Masad, J. (1995). Transition in flow over heat-transfer strips. *Physics of Fluids*, *7*(9), 2163–2174. https://doi.org/10.1063/1.868466

Masad, J., & Nayfeh, A. (1992). Laminar flow control of subsonic boundary layers by suction and heat-transfer strips. *Physics of Fluids A: Fluid Dynamics*, *4*(6), 1259–1272. https://doi.org/10.1063/1.858244

McKeon, B., Comte-Bellot, G., Foss, J., Westerweel, J., Scarano, F., Tropea, C., Meyers, J., Lee, J., Cavone, A., Schodl, R., Koochesfahani, M., Andreopoulos, Y., Dahm, W., Mullin, J., Wallace, J., Vukoslavčević, P., Morris, S., Pardyjak, E., & Cuerva, A. (2007). Velocity, vorticity, and mach number. In C. Tropea, A. L. Yarin, & J. F. Foss (Eds.), *Springer handbook of experimental fluid mechanics* (pp. 215–471). Springer Berlin Heidelberg. https://doi.org/10.1007/978-3-540-30299-5_5

Merino-Martínez, R., Rubio-Carpio, A., Lima Pereira, L., van Herk, S., Avallone, F., Ragni, D., & Kotsonis, M. (2020). Aeroacoustic design and characterization of the 3d-printed, open-jet, anechoic wind tunnel of delft university of technology. *Applied Acoustics*, *170*, 107504. https://doi.org/10.1016/j.apacoust.2020.107504

Morkovin, M. (1994). Transition in open flow systems-a reassessment. *Bull. Am. Phys. Soc.*, *39*, 1882.

O'Neill, P., Nicolaides, D., Honnery, D., & Soria, J. (2004). Autocorrelation functions and the determination of integral length with reference to experimental and numerical data. *15th Australasian fluid mechanics conference*, *1*, 1–4.

Ossofsky, E. (2004). Constant Temperature Operation of the Hot Wire Anemometer at High Frequency. *Review of Scientific Instruments*, *19*(12), 881–889. https://doi.org/10.1063/1.1741190

Özgen, S. (2004). Effect of heat transfer on stability and transition characteristics of boundary-layers. *International journal of heat and mass transfer*, *47*(22), 4697–4712. https://doi.org/10.1016/j.ijheatmasstransfer.2004.05.026

Özgen, S., & Kırcalı, S. (2008). Linear stability analysis in compressible, flat-plate boundary-layers. *Theoretical and Computational Fluid Dynamics*, *22*, 1–20. https://doi.org/10.1007/s00162-007-0071-0

Peng, K., Arkesteijn, J., Avallone, F., & Kotsonis, M. (2022). Experimental base flow modification on a swept wing using plasma forcing. *Physics of Fluids*, *34*(10), 103614. https://doi.org/10.1063/5.0118861

Perry, A., & Morrison, G. (1971). A study of the constant-temperature hot-wire anemometer. *Journal of Fluid Mechanics*, *47*(3), 577–599.

Rajendrakumar, N. (2021). *An experimental investigation of crossflow instability interaction with forward facing steps* [Master's thesis, Delft University of Technology].

Reed, H., & Saric, S. (1989). Stability of three-dimensional boundary layers. *Annual Review of Fluid Mechanics*, *21*(1), 235–284. https://doi.org/10.1146/annurev.fl.21.010189.001315

Reed, H., & Saric, S. (2014). Attachment-line heating in a compressible flow. *Journal of Engineering Mathematics*, *84*, 99–110. https://doi.org/10.1007/s10665-013-9662-5

Reibert, M., & Saric, W. (1997, June). Review of swept-wing transition. In *28th fluid dynamics conference*. https://doi.org/10.2514/6.1997-1816

Reibert, M., Saric, S., Carrillo, R., & Chapman, K. (1996). Experiments in nonlinear saturation of stationary crossflow vortices in a swept-wing boundary layer. *34th Aerospace Sciences Meeting and Exhibit*. https://doi.org/https://arc.aiaa.org/doi/abs/10.2514/6.1996-184

Ren, J., & Kloker, M. (2022). Instabilities in three-dimensional boundary-layer flows with a highly non-ideal fluid. *Journal of Fluid Mechanics*, *951*, A9. https://doi.org/10.1017/jfm.2022.845

Reshotko, E. (1979). Drag reduction by cooling in hydrogen-fueled aircraft. *Journal of Aircraft*, *16*(9), 584–590. https://doi.org/10.2514/3.58571

Rius Vidales, A. (2022). *Influence of a forward-facing step on crossflow instability and transition: An experimental study in a swept wing boundary-layer* [Doctoral dissertation, Delft University of Technology]. https://doi.org/10.4233/uuid:6fd8a152-ab7a-4ecd-a817-61945d431bef

Rolls-Royce. (2022). Rolls-royce and easyjet set new world first [Accessed on 22-08-2023]. https://www.rolls-royce.com/media/press-releases/2022/28-11-2022-rr-and-easyjet-set-new-aviation-world-first-with-successful-hydrogen-engine-run.aspx

Rondinelli, S., Gardi, A., Kapoor, R., & Sabatini, R. (2017). Benefits and challenges of liquid hydrogen fuels in commercial aviation. *International Journal of Sustainable Aviation*, *3*(3), 200–216. https://doi.org/10.1504/IJSA.2017.086845

Saric, S., Reed, H., & White, E. (2003). Stability and transition of three-dimensional boundary layers. *Annual review of fluid mechanics*, *35*(1), 413–440. https://doi.org/10.1146/annurev.fluid.35.101101.161045

Saric, W., Carpenter, A., & Reed, H. (2011). Passive control of transition in three-dimensional boundary layers, with emphasis on discrete roughness elements. *Philosophical Transactions of the Royal Society A: Mathematical, Physical and Engineering Sciences*, *369*(1940), 1352–1364. https://doi.org/10.1098/rsta.2010.0368

Saric, W., Hoos, J., & Radeztsky, R. (1991). Boundary-layer receptivity of sound with roughness. *Boundary layer stability and transition to turbulence*, 17–22.

Saric, W., Reed, H., & Kerschen, E. (2002). Boundary-layer receptivity to freestream disturbances. *Annual Review of Fluid Mechanics*, *34*(1), 291–319. https://doi.org/10.1146/annurev.fluid.34.082701.161921

Saric, W., West, D., Tufts, M., & Reed, H. (2019). Experiments on discrete roughness element technology for swept-wing laminar flow control. *AIAA Journal*, *57*(2), 641–654. https://doi.org/10.2514/1.J056897

Schlabe, D., & Lienig, J. (2014). *Model-based thermal management functions for aircraft systems* (tech. rep.). SAE. https://doi.org/https://doi.org/10.4271/2014-01-2203

Schmid, P., & Henningson, D. (2000). Stability and transition in shear flows. applied mathematical sciences. *Applied Mathematicsl Sciences*. https://doi.org/https://doi.org/10.1007/978-1-4613-0185-1

Sciacchitano, A., & Wieneke, B. (2016). Piv uncertainty propagation. *Measurement Science and Technology*, *27*(8). https://doi.org/10.1088/0957-0233/27/8/084006

Şengül, M. (2018). Transitional butterworth-chebyshev filters. *2018 18th Mediterranean Microwave Symposium (MMS)*. https://doi.org/10.1109/MMS.2018.8611988

Serpieri, J. (2018). *Cross-flow instability: Flow diagnostics and control of swept wing boundary layers* [Doctoral dissertation, Delft University of Technology]. https://doi.org/10.4233/uuid:3dac1e78-fcc3-437f-9579-048b74439f55

Serpieri, J., & Kotsonis, M. (2016). Three-dimensional organisation of primary and secondary crossflow instability. *Journal of Fluid Mechanics*, *799*, 200–245. https://doi.org/10.1017/jfm.2016.379

Tempelmann, D., Hanifi, A., & Henningson, D. (2012). Spatial optimal growth in three-dimensional compressible boundary layers. *Journal of Fluid Mechanics*, *704*, 251–279. https://doi.org/https://doi.org/10.1017/jfm.2012.235

Tempelmann, D., Schrader, L., Hanifi, A., Brandt, L., & Henningson, D. (2012). Swept wing boundary-layer receptivity to localized surface roughness. *Journal of Fluid Mechanics*, *711*, 516–544. https://doi.org/10.1017/jfm.2012.405

Theisen, J., Brewer, G., & Miranda, L. (1979). Laminar flow stabilization by surface cooling on hydrogen fueled aircraft. *Aircraft Systems and Technology Meeting*. https://doi.org/10.2514/6.1979-1863

Tsuji, T., Nagano, Y., & Tagawa, M. (1992). Frequency response and instantaneous temperature profile of cold-wire sensors for fluid temperature fluctuation measurements. *Experiments in Fluids*, *13*, 171–178. https://doi.org/10.1007/BF00218164

Wartemann, V., Camillo, G., Neumann, J., Weber, A., & Wagner, A. (2022). Stability analyses of hypersonic, conical flows with transpiration cooling. *IUTAM Laminar-Turbulent Transition*, 671–689. https://doi.org/https://doi.org/10.1007/978-3-030-67902-6_59

Wasserman, P., & Kloker, M. (2002). Mechanisms and passive control of crossflow-vortex-induced transition in a three-dimensional boundary layer. *Journal of Fluid Mechanics*, *456*, 49–84. https://doi.org/10.1017/S0022112001007418

Wasserman, P., & Kloker, M. (2003). Transition mechanisms induced by travelling crossflow vortices in a three-dimensional boundary layer. *Journal of Fluid Mechanics*, *483*, 67–89. https://doi.org/10.1017/S0022112003003884

White, E., & Ergin, F. (2004). Using laminar-flow velocity profiles to locate the wall behind roughness elements. *Experiments in fluids*, *36*, 805–812.

White, E., & Saric, S. (2005). Secondary instability of crossflow vortices. *Journal of Fluid Mechanics*, *525*, 275–308. https://doi.org/10.1017/S002211200400268X

White, E., Saric, S., Gladden, R., & Gabet, P. (2001). Stages of swept-wing transition. *39th Aerospace Sciences Meeting and Exhibit*, 271. https://doi.org/10.2514/6.2001-271

White, F. (2006). *Viscous fluid flow* (Vol. 3). McGraw-Hill New York.

Yadala, S., Hehner, M., Serpieri, J., Benard, N., Dörr, P. C., Kloker, M., & Kotsonis, M. (2018). Experimental control of swept-wing transition through base-flow modification by plasma actuators. *Journal of Fluid Mechanics*, *844*, R2. https://doi.org/10.1017/jfm.2018.268

Yadala, S., Hehner, M. T., Serpieri, J., Benard, N., & Kotsonis, M. (2021). Plasma-based forcing strategies for control of crossflow instabilities. *AIAA Journal*, *59*(9), 3406–3416. https://doi.org/10.2514/1.J060101

Zafar, F., & Alam, M. M. (2020). Mixed convection heat transfer from a circular cylinder submerged in wake. *International Journal of Mechanical Sciences*, *183*, 105733. https://doi.org/https://doi.org/10.1016/j.ijmecsci.2020.105733

Zoppini, G. (2023). *Receptivity of swept wing boundary layers to surface roughness* [Doctoral dissertation, Delft University of Technology]. https://doi.org/https://doi.org/10.4233/uuid:edfbbf98-2530-463b-94d0-43dee5435786